INVESTIGATION ON THE APPLICABILITY OF ACTIVE MAGNETIC BEARINGS TO HIGH SPEED SPINDLE DESIGN

A Thesis

by

MENGKE LIU

Submitted to the Office of Graduate and Professional Studies of
Texas A&M University
in partial fulfillment of the requirements for the degree of

MASTER OF SCIENCE

Chair of Committee,	Chii-Der S. Suh
Committee Members,	Nguyen Hung
	Won-Jong Kim
Head of Department,	Andreas A. Polycarpou

May 2015

Major Subject: Mechanical Engineering

ABSTRACT

A novel concept applicable to the control of spindles at high speed is developed by using active magnetic bearings (AMBs) that are non-contact and of low vibration. Extensive literature reviews explicate that the broad applications of AMBs are severely hampered by the incomplete description of the underlying electro-magnetic-mechanical dynamics. The thesis considers the gyroscopic effect inherent of a flexible rotor and explores the geometry coupling of the electro-magnetic actuators to the formulation of a comprehensive nonlinear AMB-rotor model. The model provides the basis for the creation of a novel time-frequency control algorithm whose derivation requires no linearization or mathematical simplification of any kind, thus allowing the model system to retain its true fundamental characteristics. Unlike proportional-integral-derivative (PID) controllers that are dominant in most if not all AMB configurations, the controller developed for the research is inspired by the wavelet-based nonlinear time-frequency control methodology that incorporates the basic notions of online system identification and adaptive control. Wavelet filter banks and filtered-x least-mean-square (LMS) algorithm are two of the major salient physical features of the controller design, with the former providing concurrent temporal and spectral resolutions needed for identifying nonlinear states of motion and the latter ensuring the dynamic stability of the AMB-rotor system at all operating speeds subjected to the presence of external disturbances. It is shown in the thesis that the vibration of the rotor is unconditionally controlled by maintaining the mandatory 0.55 mm air gap at 150,000 and 187,500 rpm subject to a tight spatial constraint (tolerance) of the order of 0.1375mm. System responses with and

without considering the gyroscopic motion and geometry coupling are studied to demonstrate the negative impact on misinterpreting the AMB-rotor dynamics when the two effects are neglected. The case of an impact of 5,000m/s^2 in magnitude and 0.001 seconds in duration at 187,500rpm is also investigated to establish the robustness of the controller design. The time responses of all the cases considered are both temporally bounded and spectrally bandwidth-limited, thus demonstrating the effectiveness of the wavelet-based time-frequency controller design in mitigating the inherent instability of the AMB-rotor system at extreme speeds.

ACKNOWLEDGEMENTS

I would like to dedicate this thesis to my loving parents who raised me with the greatest love and the deepest affection in the world. Without their support I would not have been able to finish my study at Texas A&M University. No words of gratitude are equal to their unconditional love and steadfast encouragement.

I am grateful to Dr. C. Steve Suh, who is my research advisor and the chairman of my thesis committee, for his patience, guidance, encouragement, and criticism of my work. His serious attitude toward research and enthusiasm for life has greatly affected me in the last two years. My sincere appreciation also goes to Dr. Nguyen Hung and Dr. Won-Jong Kim for serving on my advisory committee and for providing their insightful guidance throughout the course of the endeavor.

Lastly, I would like to thank all my friends at Texas A&M for their generosity and support. I would like for all of them to know that I treasure their friendships very much.

TABLE OF CONTENTS

Page

LIST OF FIGURES

LIST OF TABLES

TABLE Page

CHAPTER I

INTRODUCTION

1.1 Overview

As high performance rotary machinery such as wind mills becomes populous, alternative bearings that are effective in mitigating friction, vibration, and thermal generation are in high demand. One of the alternatives is active magnetic bearings (AMBs). AMBs are non-contact in that they exploit electro-magnetic force to suspend the rotor to maintain a desired "air gap," which is the space between the rotor and stators (electro-magnets). Typically, an AMB system consists of two radial AMBs and one axial AMB that together as an integral unit controls five degree-of-freedoms (DOFs) in total. As illustrated in Fig. 1.1, the single radial AMB has two pairs of electromagnets as the stators. They are made of laminated rings to reduce energy loss. The coils wounded around these stators carry the driving currents controlled by the controllers (not shown). The electromagnetic force field is generated in the cavity to suspend the rotor and to maintain a spatial clearance between the rotor and stators which is the air gap.

AMBs are found in many applications. For example, they enable the variations of damping and stiffness in suspension systems [1, 2] and compressors [3]. Their non-contact nature is explored in the design of fly-wheel energy storage devices [4, 5] and pumps [3] to minimize rotor kinetic energy loss to friction and thermal generation. Given their explicit advantages over the conventional mechanical bearings [6], AMBs are shown to be promising in machine tool spindle design [7]. AMBs have also found applications in biological systems including being employed as an essential component in artificial

hearts [2, 8]. Since alien contaminants such as dust, debris, and fluid resulted from lubricant-leakage or mechanical-contact could disperse through blood circulation and ultimately compromise the proper functioning of human organs, the implication of exploring AMBs as a viable alternative to fluid film bearings or mechanical bearings in human body is significant. This is a typical example of AMBs being utilized to replace conventional rolling elements when the environment is of concern.

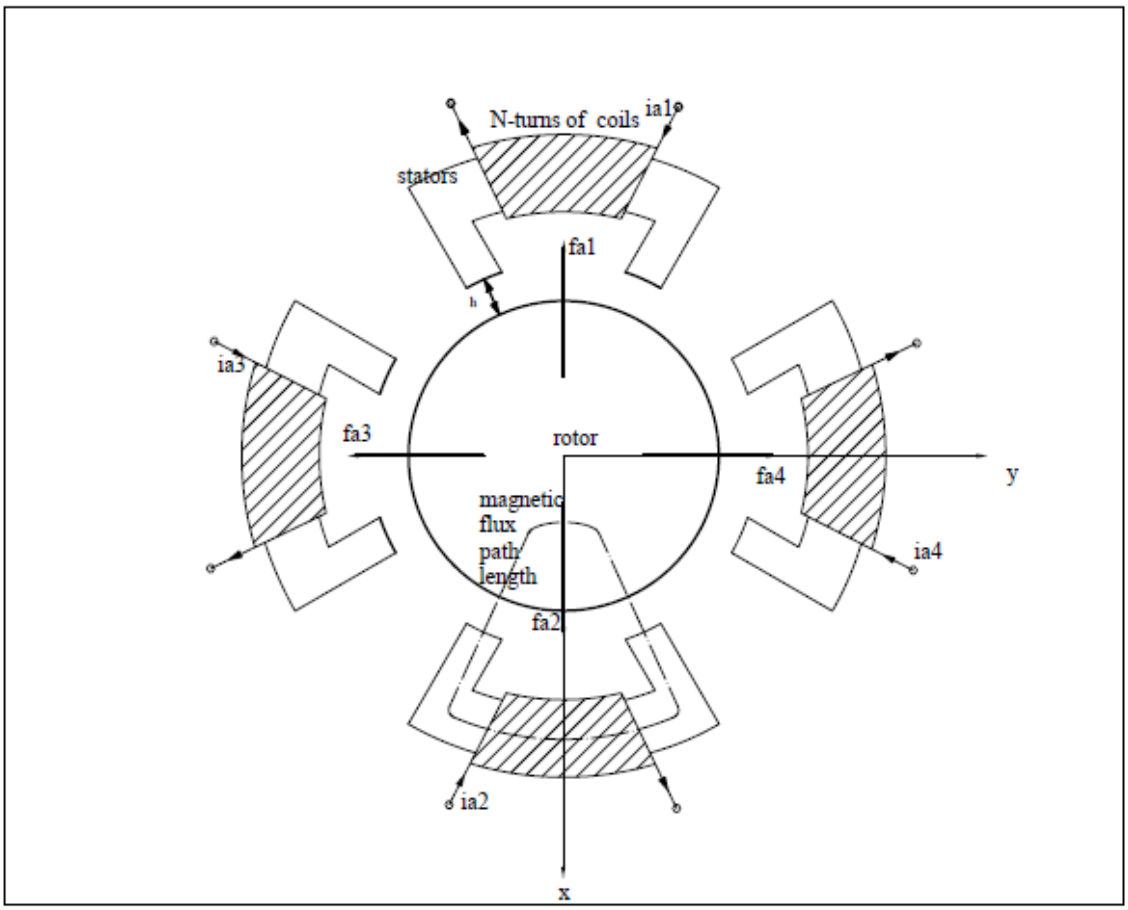

Fig. 1.1 AMB configuration

1.2 Issues of Present Work

Though studies are abundant and demonstrating promising potentials, however, two major issues hamper the broader application of AMBs. The first is the disregard for the gyroscopic effect and geometry coupling that influence the magnitude as well as distribution of the electro-magnetic force in AMBs. Not considering the two has a significant implication for the proper control of AMBs. In describing AMB dynamics and subsequently establishing the corresponding dynamic system model, gyroscopic effect, which characterizes the gyroscopic motion of the rotor, is generally neglected [9, 10]. For short rotors the assumption of negligible gyroscopic effect is acceptable because the angular displacements of the rotor at both ends where AMBs are mounted can be assumed to be identical, thus resulting in no relative displacement. However, for the long rotor considered in this thesis, the relative displacement is prominent and non-negligible. The dynamics of the AMB system is incomplete without considering the gyroscopic effect.

An intensive literature review shows that the generation of electro-magnetic force is usually simplified by disregarding the geometry coupling effect so as to retaining the radial component and dropping the component perpendicular to it. However, the perpendicular component can be significant enough to have an impact on the motion of the rotor when it is off the bearing center [9, 10]. AMB control cannot be effective without considering the geometry coupling effect.

The dominant method for controlling AMB systems is PID control where linearization is inevitably required for system modeling and controller design. Linearization has been studied under the topics of sliding mode control for AMBs [11, 12] and input-output signal

linearization [13-17]. Linearization necessarily would misinterpret a nonlinear system such as AMBs of its true inherent characteristics. Control of AMBs has conventionally been facilitated mainly in the time-domain. Research focusing on the control of AMBs in both the time and frequency domains is rare. Because dynamic instability is characterized by time-varying frequency and non-stationary spectrum [18, 19], the control of AMBs needs be executed in the time and frequency-domain concurrently to ensure stability and performance at high speed. This is the reason why chatter is detrimental to surface finish and damaging to both the work-piece and the tool. The hazardous effect is particularly prominent at high-speed drilling or milling operation when the excitation is of broad bandwidth. Control of dynamic instability must be realized in the time and frequency domains simultaneously.

1.3 Research Objective

The proposed research is aimed to establish the feasibility of a high-speed AMB-rotor system so as to address the aforementioned issues through the implementation of a novel nonlinear controller design. The objective of the research is of two-fold. The first is to develop a comprehensive dynamic model allowing the highly nonlinear characteristics of a specific AMB-rotor configuration to be studied. The second is to formulate a time-frequency control methodology that is robust, requires no linearization, and incorporates no feedback.

1.3.1 Model Development

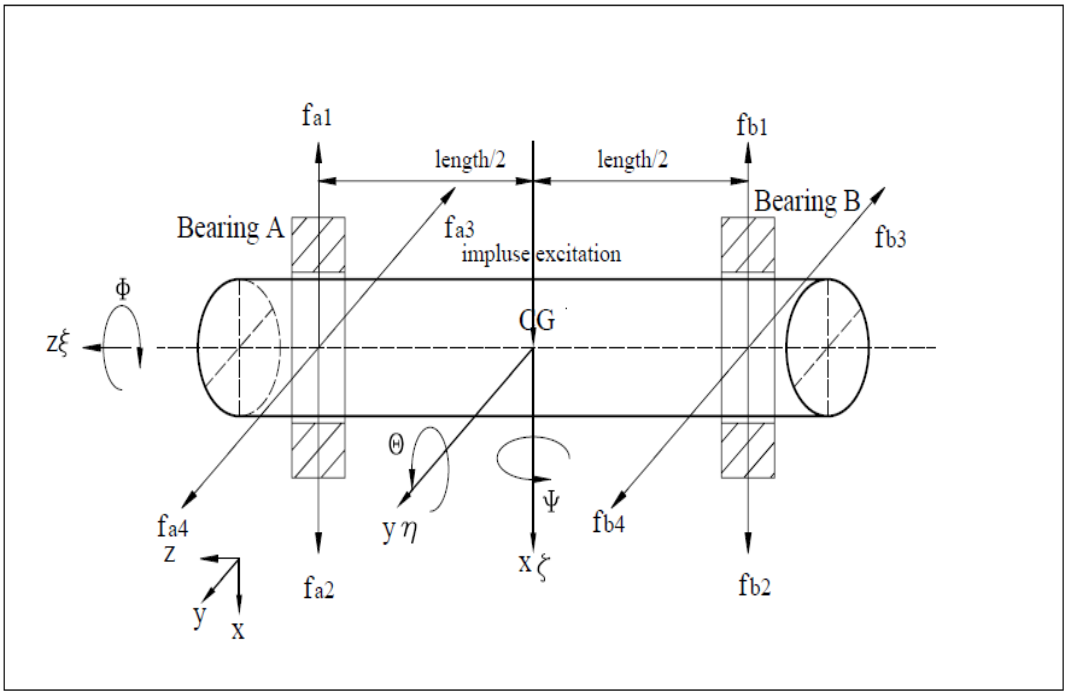

Fig. 1.2 AMB model configuration (with impulse excitation applied at CG)

Fig. 1.2 presents a five degree-of-freedom (DOF) AMB-supported rotor model used for the research. Because they can negatively impact the motion and stability of the AMB-rotor system, gyroscopic and geometry coupling effects are considered in the system's equations of motion (EOM). The radial and polar moments of inertia of the rotor are included in the EOM with the length of the rotor explicitly being specified. The corresponding EOM that incorporates gyroscopic effect has been derived as follows:

$$\ddot{x} = \frac{1}{m_r}\left(f_{ax} + f_{bx} + f_{dx}\right) \tag{1.1}$$

$$\ddot{y} = \frac{1}{m_r}(f_{ay} + f_{by} + f_{dy}) \tag{1.2}$$

$$\ddot{\theta} - \left(\frac{I_p}{I_r}\right)\dot{\phi}\dot{\psi} + \dot{\psi}\sin\theta - \left(\frac{I_p}{I_r}\right)\dot{\psi}^2\sin\theta = \frac{M_x}{I_r} \tag{1.3}$$

$$\ddot{\psi} + \left(\frac{I_p}{I_r}\right)\dot{\phi}\dot{\theta} + \left(\frac{I_p}{I_r}\right)\dot{\psi}\dot{\theta}\sin\theta - \dot{\psi}\dot{\theta}\sin\theta + \dot{\psi}^2\sin\theta\cos\phi\left(\sin\phi - \cos\theta\right) = \frac{M_y}{I_r} \tag{1.4}$$

$$\ddot{\phi} + \ddot{\psi}\sin\theta + \dot{\psi}\cos\theta\dot{\theta} = \frac{M_x\sin\theta + M_z}{I_p} \tag{1.5}$$

$$M_x = -f_{ax}\frac{l}{2} + f_{bx}\frac{l}{2} \tag{1.6}$$

$$M_y = f_{ay}\frac{l}{2} - f_{by}\frac{l}{2} \tag{1.7}$$

$$f_{dy} = m_r\mu\dot{\phi}^2\cos\left(\dot{\phi}t\right) \tag{1.8}$$

$$f_{dx} = m_r\mu\dot{\phi}^2\sin\left(\dot{\phi}t\right) \tag{1.9}$$

$$f_{d\theta} = {2\left(I_p - I_r\right)}\Big/{l}\ \tau\dot{\phi}^2\cos\left(\dot{\phi}t\right) \tag{1.10}$$

$$f_{d\psi} = {2\left(I_p - I_r\right)}\Big/{l}\ \tau\dot{\phi}^2\sin\left(\dot{\phi}t\right) \tag{1.11}$$

where f_{ax}, f_{bx}, f_{ay}, and f_{by} are the electro-magnetic actuation force components generated by the two supporting AMBs, bearings A and B, in the x- and y-directions. ψ , θ and ϕ

denote the angular displacements, and μ and τ are the static eccentricity and dynamic eccentricity, respectively.

The effect of geometry coupling is considered for the comprehensive description of the electrical-magnetic force in the AMB-rotor model. With the consideration of the parameter, denoted as α in the followings, the electro-magnetic force can be decomposed into two perpendicular components allowing forces along different axes in bearing A to be readily correlated as follows:

$$f_{ax} = f_{a1} - f_{a2} + \alpha\left(\frac{x_a}{h}\right)\left(f_{a3} + f_{a4}\right) \tag{1.12}$$

$$f_{ay} = f_{a3} - f_{a4} + \alpha\left(\frac{y_a}{h}\right)\left(f_{a1} + f_{a2}\right) \tag{1.13}$$

1.3.2 Controller Design

Nonlinear control of AMBs and magnetic levitation systems were investigated in [20] and [21] where linearization was applied to simplify the EOMs. In this thesis, a novel control scheme is formulated to control the AMB-rotor model system described above. The scheme employs wavelets and filtered-x LMS (FXLMS) algorithm as two of the physical features. The controller is developed without resorting to linearization which is a common practice of the controller design community. With the implementation of filtered-x LMS algorithm, probable mathematical singularity and physical instability at uncontrollable frequencies is avoided, thus ensuring the proper control of the model system response in

the frequency domain. The controller, which is adaptive, is so designed that the control parameters are updated in *real-time* to warrant desired system response at all time.

Numerical investigations are performed using the following (four) models of different considerations for system parameters: (1) model without considering gyroscopic effect; (2) model without considering geometry coupling; (3) model with both gyroscopic effect and geometry coupling included; and (4) model with a broad bandwidth, brief duration impulse excitation.

1.3.3 Research Plan with Tasks

To meet the research objective defined above, it is imperative that a solid plan along with definitive tasks is developed. The followings are specific tasks generated to address all the issues regarding the application of AMBs, and, once properly executed, to substantiate the applicability of AMBs to high speed spindle design.

1. Create an AMB-rotor design concept
2. Derive the corresponding dynamic model that describes the AMB-rotor design
3. Develop and implement a nonlinear time-frequency controller design based on the derived model
4. Generate numerical results to validate the model as well as the controller design

CHAPTER II

DYNAMICS OF AMB-SUPPORTED ROTOR

The diagram in Fig. 2.1 shows a solid cylindrical shaft that is supported by two active magnetic bearings (AMBs), Bearing A and Bearing B. At where the geometric center (CG) is located a coordinate system *xyz* is defined. In addition to the three translational degrees-of-freedom, three rotational degrees-of-freedoms are also specified using notations Ψ, Θ, and Φ as shown.

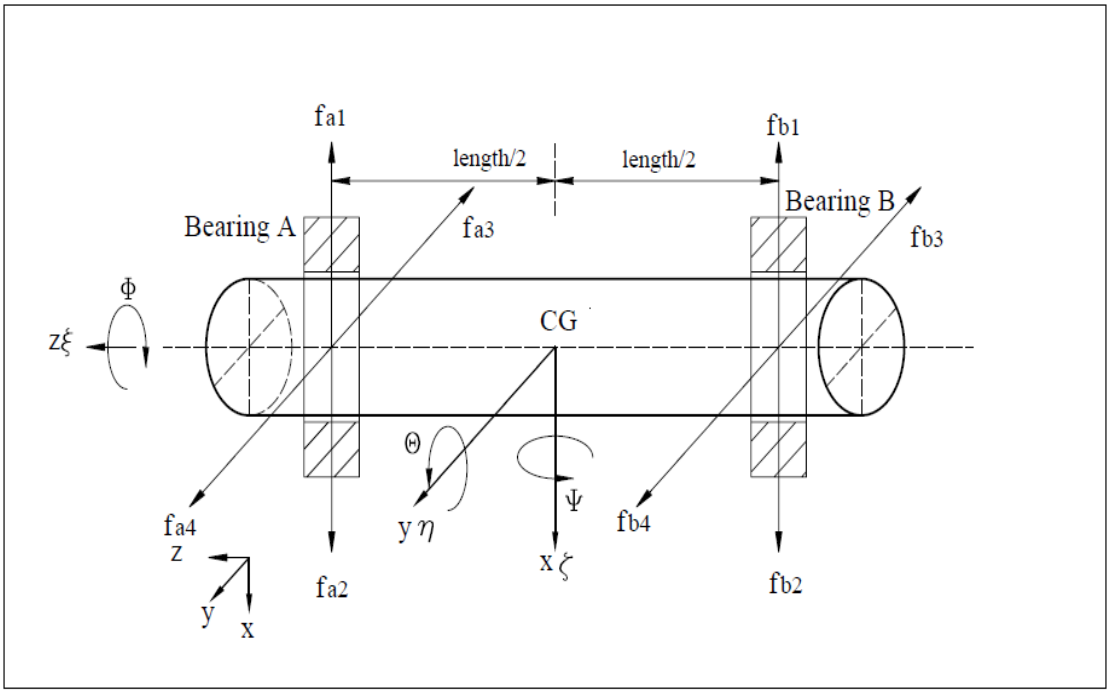

Fig. 2.1 AMB system

The translational and rotational motions of the rotor can be described using the Newton's Laws as follows,

$$\vec{F} = \dot{\vec{I}}_m = \frac{d}{dt}\left(m_r \vec{v}\right) \tag{2.1}$$

$$\vec{M} = \dot{\vec{H}} = \frac{d}{dt}\left(I\vec{\omega}\right) \tag{2.2}$$

with $\vec{F}$ and $\vec{M}$ being the external force and the mass moment of the rotor, respectively, $\vec{I}_m$ and $\vec{H}$ the linear and angular momentum vectors, m_r and $\vec{v}$ the mass and velocity vector of the rotor, and I and $\vec{\omega}$ the inertia tensor and angular velocity vector of the rotor. As the rotor rotates the corresponding inertia tensor I varies with respect to the stationary reference frame defined by *xyz*. As such a coordinate system of rotation $\zeta\eta\xi$ is attached to the center of mass for the evaluation of the moment vector in Eq. (2.3) in the following

$$\left(\frac{d}{dt}\right)_{\zeta\eta\xi}\left(I\vec{\omega}\right) + \vec{\omega}\times\left(I\vec{\omega}\right) = \vec{M}_{\zeta\eta\xi}$$

Assuming that mass imbalance is negligible, the inertia tensor and angular velocity vector of the rotor are

$$I_{\zeta\eta\xi} = \begin{pmatrix} I_r & 0 & 0 \\ 0 & I_r & 0 \\ 0 & 0 & I_p \end{pmatrix} \tag{2.3}$$

$$\begin{pmatrix} \omega_1 \\ \omega_2 \\ \omega_3 \end{pmatrix} = \begin{pmatrix} \dot{\theta}\sin\phi + \dot{\psi}\cos\phi \\ \dot{\theta}\cos\phi - \dot{\psi}\sin\phi \\ \dot{\phi} + \dot{\psi}\sin\theta \end{pmatrix} \tag{2.4}$$

where I_r and I_p are the radial and polar moments of inertia of the rotor and ψ, θ, and ϕ denote the angular displacements associated with the stationary coordinates. Since

angles ψ and θ are generally very small in applications, the small angle approximations that $\cos\theta \approx 1$ and $\sin\theta \approx 0$ are commonly adopted. No such approximations will be followed in the derivations below so as to incorporate no linearization.

Rearranging Eq. (2.5) we have

$$\begin{pmatrix} \omega_1 \\ \omega_2 \\ \omega_3 \end{pmatrix} = \begin{pmatrix} \cos\phi & \sin\phi & 0 \\ -\sin\phi & \cos\phi & 0 \\ \sin\theta & 0 & 1 \end{pmatrix} \begin{pmatrix} \dot{\psi} \\ \dot{\theta} \\ \dot{\phi} \end{pmatrix} \tag{2.5}$$

Similarly, the moment with respect to the rotating frame is

$$M_{\zeta\eta\xi} = \begin{pmatrix} \cos\phi & \sin\phi & 0 \\ -\sin\phi & \cos\phi & 0 \\ \sin\theta & 0 & 1 \end{pmatrix} M_{xyz} \tag{2.6}$$

Substituting Eqs. (2.6) and (2.7) into Eq. (2.3), one has

$$\left(\frac{d}{dt}\right)_{\zeta\eta\xi} (I\omega) + \omega \times (I\omega) = \frac{d}{dt} \begin{pmatrix} I_r\left(\dot{\theta}\sin\phi + \dot{\psi}\cos\phi\right) \\ I_r\left(\dot{\theta}\cos\phi - \dot{\psi}\sin\phi\right) \\ I_p\left(\dot{\phi} + \dot{\psi}\sin\theta\right) \end{pmatrix} + \begin{pmatrix} \dot{\theta}\sin\phi + \dot{\psi}\cos\phi \\ \dot{\theta}\cos\phi - \dot{\psi}\sin\phi \\ \dot{\phi} + \dot{\psi}\sin\theta \end{pmatrix} \times \begin{pmatrix} I_r\left(\dot{\theta}\sin\phi + \dot{\psi}\cos\phi\right) \\ I_r\left(\dot{\theta}\cos\phi - \dot{\psi}\sin\phi\right) \\ I_p\left(\dot{\phi} + \dot{\psi}\sin\theta\right) \end{pmatrix}$$

which subsequently leads to the following equations that govern the motion of the rotor in the *xyz*-coordinates.

$$\ddot{\theta} - \left(\frac{I_p}{I_r}\right)\dot{\phi}\dot{\psi} + \dot{\psi}\sin\theta - \left(\frac{I_p}{I_r}\right)\dot{\psi}^2\sin\theta = \frac{M_x}{I_r} \tag{2.7}$$

$$\ddot{\psi} + \left(\frac{I_p}{I_r}\right)\dot{\phi}\dot{\theta} + \left(\frac{I_p}{I_r}\right)\dot{\psi}\dot{\theta}\sin\theta - \dot{\psi}\dot{\theta}\sin\theta + \dot{\psi}^2\sin\theta\cos\phi\left(\sin\phi - \cos\theta\right) = \frac{M_y}{I_r} \tag{2.8}$$

$$\ddot{\phi} + \ddot{\psi}\sin\theta + \dot{\psi}\cos\theta\dot{\theta} = \frac{M_x\sin\theta + M_z}{I_p} \tag{2.9}$$

In the interest of studying the motion of the rotor in the *xy*-plane, it is assumed that there is no force applied along, or moment exerted about, the *z*-axis. The non-zero moments are therefore

$$M_x = -f_{ax}\frac{l}{2} + f_{bx}\frac{l}{2} \tag{2.10}$$

$$M_y = f_{ay}\frac{l}{2} - f_{by}\frac{l}{2} \tag{2.11}$$

It is self-explanatory in Eqs. (2.14)-(2.17) below that f_{ax}, f_{bx}, f_{ay}, and f_{by} are the electro-magnetic actuation force components generated by the bearings A and B in the x- and y-directions. As is noted in [9], f_{ax} and f_{ay} are coupled. So are f_{bx} and f_{by}. The coupling is established in the following through α, a physical quantity called geometry coupling parameter,

$$f_{ax} = f_{a1} - f_{a2} + \alpha\left(\frac{x_a}{h}\right)\left(f_{a3} + f_{a4}\right) \tag{2.12}$$

$$f_{bx} = f_{b1} - f_{b2} + \alpha\left(\frac{x_b}{h}\right)\left(f_{b3} + f_{b4}\right) \tag{2.13}$$

$$f_{ay} = f_{a3} - f_{a4} + \alpha\left(\frac{y_a}{h}\right)\left(f_{a1} + f_{a2}\right) \tag{2.14}$$

$$f_{by} = f_{b3} - f_{b4} + \alpha\left(\frac{y_b}{h}\right)\left(f_{b1} + f_{b2}\right) \tag{2.15}$$

When the small angle assumption is considered, that is, when $\sin\theta \approx 0$, the governing equations become

$$\ddot{\theta} - \left(\frac{I_p}{I_r}\right)\dot{\phi}\dot{\psi} = \frac{M_x}{I_r} \tag{2.16}$$

$$\ddot{\psi} + \left(\frac{I_p}{I_r}\right)\dot{\phi}\dot{\theta} = \frac{M_y}{I_r} \tag{2.17}$$

Eqs. (2.18) and (2.19) are commonly employed to represent the dynamics of a spinning rotor. However, such a linearized version is not valid for describing rotor motions at high speed.

In the case of a long rotor, gyroscopic effects are anything but negligible. When the length of the rotor, *l*, is prominent, the displacement components, x_a and y_a, of the shaft at Bearing A, and the displacement components, x_b and y_b at Bearing B, are correlated with the displacements of the mass center of the rotor, *x* and *y*, as follows:

$$x_a = x + l\sin\theta \tag{2.18}$$

$$y_a = y - l\sin\psi \tag{2.19}$$

$$x_b = x - l\sin\theta \tag{2.20}$$

$$y_b = y + l\sin\psi \tag{2.21}$$

The rotor is initially set at and aligned with the geometric centers of the active magnetic bearings A and B. However, the presence of the rotor's own weight induces a static eccentricity, μ , and a dynamic eccentricity , τ, that are both non-zero. Although small in magnitude, nevertheless, neglecting the eccentricities is considered inappropriate. The imbalances due to the eccentricities can be determined as force components as

$$f_{dy} = m_r \mu \dot{\phi}^2 \cos\left(\dot{\phi} t\right) \tag{2.22}$$

$$f_{dx} = m_r \mu \dot{\phi}^2 \sin\left(\dot{\phi} t\right) \tag{2.23}$$

$$f_{d\theta} = {2\left(I_p - I_r\right)}\Big/{l}\ \tau \dot{\phi}^2 \cos\left(\dot{\phi} t\right) \tag{2.24}$$

$$f_{d\psi} = {2\left(I_p - I_r\right)}\Big/{l}\ \tau \dot{\phi}^2 \sin\left(\dot{\phi} t\right) \tag{2.25}$$

The motion of the rotor in the *xy*-plane can be fully characterized using the following four equations:

$$\ddot{x} = \frac{1}{m_r}\left(f_{ax} + f_{bx} + f_{dx}\right) \tag{2.26}$$

$$\ddot{y} = \frac{1}{m_r}\left(f_{ay} + f_{by} + f_{dy}\right) \tag{2.27}$$

$$\ddot{\theta} - \left(\frac{I_p}{I_r}\right)\dot{\phi}\dot{\psi} + \dot{\psi}\sin\theta - \left(\frac{I_p}{I_r}\right)\dot{\psi}^2 \sin\theta = \frac{M_x}{I_r} \tag{2.28}$$

$$\ddot{\psi} + \left(\frac{I_p}{I_r}\right)\dot{\phi}\dot{\theta} + \left(\frac{I_p}{I_r}\right)\dot{\psi}\dot{\theta}\sin\theta - \dot{\psi}\dot{\theta}\sin\theta + \dot{\psi}^2 \sin\theta\cos\phi\left(\sin\phi - \cos\theta\right) = \frac{M_y}{I_r} \tag{2.29}$$

Of the 4 model cases studied in the thesis; namely, (1) model without considering gyroscopic effect, (2) model without considering geometry coupling, (3) model with both gyroscopic effect and geometry coupling included, and (4) model with a broad bandwidth, brief duration impulse excitation, Eqs. (2.28)-(2.31) correspond to Model Case (3).

When gyroscopic effect is ignored, the motion of the rotor is exclusively translational. The dynamics of the rotor can then be described by the following set of equations which involve no angular motions:

$$\ddot{x} = \frac{1}{m_r}\left(f_{ax} + f_{bx} + f_{dx}\right) \tag{2.30}$$

$$\ddot{y} = \frac{1}{m_r}\left(f_{ay} + f_{by} + f_{dy}\right) \tag{2.31}$$

$$f_{ax} = f_{a1} - f_{a2} + \alpha\left(\frac{x_a}{h}\right)\left(f_{a3} + f_{a4}\right) \tag{2.32}$$

$$f_{bx} = f_{b1} - f_{b2} + \alpha\left(\frac{x_b}{h}\right)\left(f_{b3} + f_{b4}\right) \tag{2.33}$$

$$f_{ay} = f_{a3} - f_{a4} + \alpha\left(\frac{y_a}{h}\right)\left(f_{a1} + f_{a2}\right) \tag{2.34}$$

$$f_{by} = f_{b3} - f_{b4} + \alpha\left(\frac{y_b}{h}\right)\left(f_{b1} + f_{b2}\right) \tag{2.35}$$

where

$$x_a = x_b = x \tag{2.36}$$

$$y_a = y_b = y \tag{2.37}$$

It is understood that Eqs. (2.32)-(2.39) correspond to Model Case (1).

The decoupling of electro-magnetic forces given in Eqs. (2.14)-(2.17) constitutes Model Case (2). The corresponding equations of motion are listed in Eqs. (2.40)-(2.47) below

$$\ddot{x} = \frac{1}{m_r}\left(f_{ax} + f_{bx} + f_{dx}\right) \tag{2.38}$$

$$\ddot{y} = \frac{1}{m_r}(f_{ay} + f_{by} + f_{dy}) \tag{2.39}$$

$$\ddot{\theta} - \left(\frac{I_p}{I_r}\right)\dot{\phi}\dot{\psi} + \dot{\psi}\sin\theta - \left(\frac{I_p}{I_r}\right)\dot{\psi}^2\sin\theta = \frac{M_x}{I_r} \tag{2.40}$$

$$\ddot{\psi} + \left(\frac{I_p}{I_r}\right)\dot{\phi}\dot{\theta} + \left(\frac{I_p}{I_r}\right)\dot{\psi}\dot{\theta}\sin\theta - \dot{\psi}\dot{\theta}\sin\theta + \dot{\psi}^2\sin\theta\cos\phi\left(\sin\phi - \cos\theta\right) = \frac{M_y}{I_r} \tag{2.41}$$

where

$$f_{ax} = f_{a1} - f_{a2} \tag{2.42}$$

$$f_{bx} = f_{b1} - f_{b2} \tag{2.43}$$

$$f_{ay} = f_{a3} - f_{a4} \tag{2.44}$$

$$f_{by} = f_{b3} - f_{b4} \tag{2.45}$$

In Model Case (4) an impulse is applied to the rotor in the x-direction. This is implemented by incorporating the impulse excitation $\delta_x(t)$ in Model Case (3) into the equation below

$$\ddot{x} = \frac{1}{m_r}\left(f_{ax} + f_{bx} + f_{dx} + \delta_x(t)\right) \tag{2.46}$$

CHAPTER III

ELECTRO-MECHANICAL DYNAMICS

In the first half of the Chapter III the physical principles governing the electromagnetic actuation force are derived in detail. The electro-mechanical system model is then presented as the state-variable representation that describes the dynamics of the AMB-rotor model.

3.1 Electromagnetic Actuation Force

An active magnetic bearing is comprised of a stator and a rotor. The rotor is a shaft elevated in the bearing cavity by the electromagnetic attraction forces induced by the stator, which is the electromagnetic force generator. Two stators are considered in this investigation and each of them consists of four individual components. Fig. 1.1 in the Chapter I gives such an arrangement where the 2 stators exert forces that drive the radial motion of the rotor in the *xy*-plane. Each individual component of the stator is wrapped by conducting coils. When current is induced in the coils, the electro-magnet pairs create a field of magnetic flux that elevates the rotor and maintains a spatial clearance between the rotor and the stator. The clearance is called the air gap.

The quantity of magnetic lines created by an electro-magnet is characterized by the magnetic flux, Φ. Since the total magnetic flux is uniform, a parameter named magnetic flux density, B, can be defined as follows which is the number of magnetic lines per unit area:

$$B = \frac{\Phi}{A_g} \tag{3.1}$$

where A_g is the area under the air gap in the electro-magnet.

The ability of a coil in producing flux is defined as the magneto-motive force, which is the product of the number of coils, *N*, and the current running through the coils, *i*. The magnetic field intensity *H*, which is the magneto-motive force per unit length, is described using the flux path length l whose definition is depicted in Fig. 3.1:

$$H = \frac{Ni}{l} \tag{3.2}$$

Magnetic field intensity and flux intensity are correlated through two permeability constants:

$$B = \mu_0 \mu_r H \tag{3.3}$$

where $\mu_0 = 4\pi \times 10^{-7}\ H/m$ is the permeability of the free space and μ_r is the relative permeability whose value depends on the medium on which the magnetic field exerts. For air and most non-magnetic materials the relative permeability $\mu_r = 1.0$.

Analogous to resistance in electric circuits, reluctance is the parameter introduced to characterize the resistance in magnetic circuits,

$$R = \frac{Ni}{\Phi} \tag{3.4}$$

Or alternatively using Eqs. (3.1)–(3.3),

$$R = \frac{l}{\mu_0 \mu_r A_g} \tag{3.5}$$

Before proceeding further with derivations, the following assumptions are made:

(1) Flux leakage is negligibly small, meaning that the flux goes through the rotor and stator without losses.

(2) Fringing effect, the spreading of the magnetic flux lines in the air gap, is negligible.

(3) Constant permeability of the iron. That is, the permeability of the rotor and stator stays constant.

(4) The cross-section of the iron is uniform along the entire magnetic loop.

The force is generated along the magnetic loop l, which is constituted by the loop length l_{iron} in the iron and h, the nominal air gap at the initial equilibrium state. Considering Eqs. (3.4) and (3.5) and substituting l_{iron} and h, yields a new expression for Φ as follows,

$$\Phi = \frac{Ni}{\frac{2h}{\mu_0 A_g} + \frac{l_{iron}}{\mu_0 \mu_{r(iron)} A_g}} \tag{3.6}$$

Substituting Eq. (3.6) into Eq. (3.1) results in the following alternative expression for B,

$$B = \frac{Ni\mu_0}{2h + \frac{l_{iron}}{\mu_{r(iron)}}} \tag{3.7}$$

Since the permeability of iron is approximately 20,000, which is significantly greater than 1, Eq. (3.7) can be reduced to be

$$B = \frac{Ni\mu_0}{2h} \tag{3.8}$$

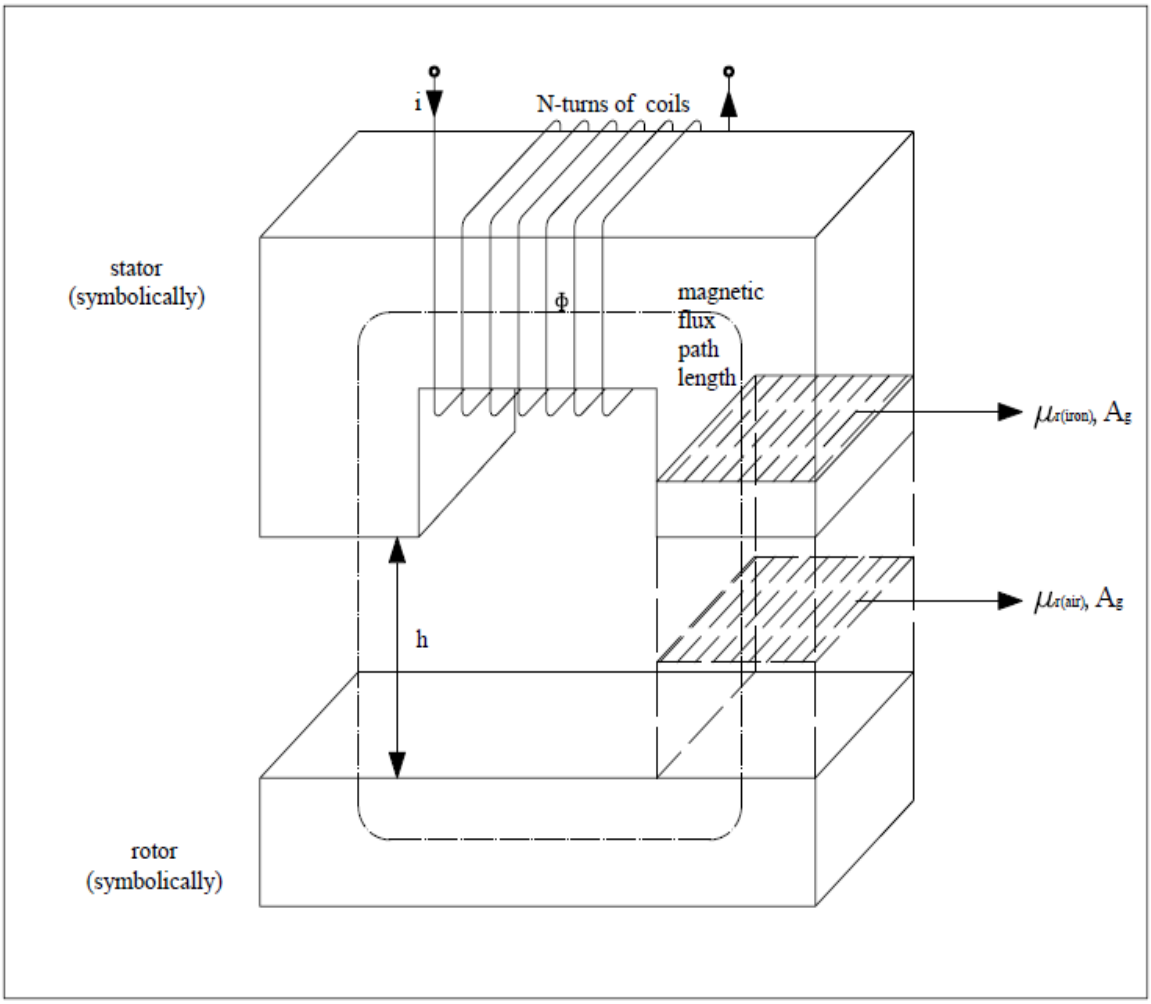

Fig. 3.1 Schematic of an electro-magnet

Also, the magnetic flux can be represented as

$$\Phi = \frac{N\mu_0 A_g i}{2h} \tag{3.9}$$

The magnetic bearing actuator force is given by

$$f = \frac{B^2 A_g}{\mu_0} \tag{3.10}$$

The force can now be shown to be a function of N, i, μ_0, A_g, and h,

$$f = \frac{\mu_0 N^2 A_g i^2}{4h^2} \tag{3.11}$$

As is seen in Fig. 3.2, the electromagnetic force in the radial direction is the resultant of two perpendicular components f_{p1} and f_{p2}. Hence, the force can be shown to be

$$f = \cos\beta \frac{\mu_0 N^2 A_g i^2}{4h^2} \tag{3.12}$$

where α is the geometry coupling parameter defined as follow [20, 21],

$$\alpha = \frac{f_n}{f_p} = \tan\beta \tag{3.13}$$

As the rotor spins, the geometric centers of the rotor at both ends do not stay in line with the bearing centers, thus necessarily resulting in time-varying air gaps in both the bearings. This renders it imperative that electromagnetic forces be modeled as the function of the rotor position. In this thesis, two active magnetic bearings are employed to support the motion of a flexible rotor. At each bearing, four actuator forces are generated by two pairs of electromagnets driven by a specified current. The magnetic actuation forces in Bearing A as seen in Fig. 3.3 are:

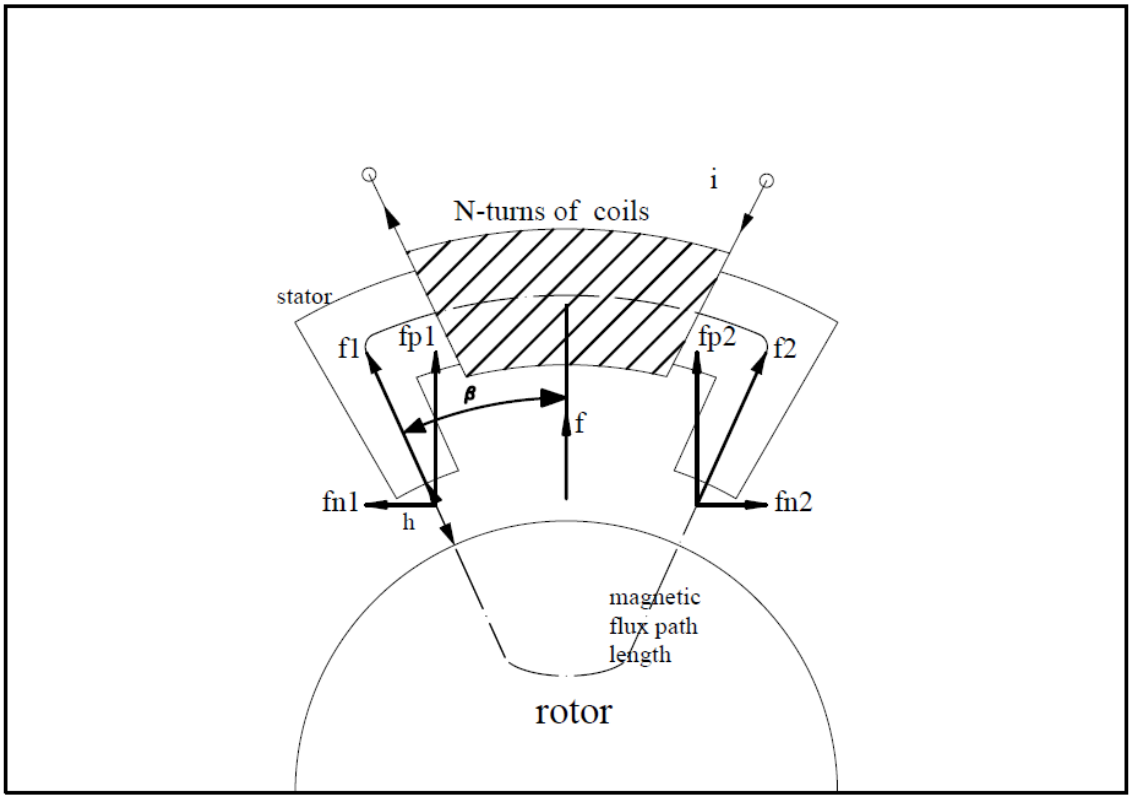

Fig. 3.2 Configuration of electro-magnetic forces

$$f_{a1} = \cos\beta \frac{k i_{a1}^2}{\left(h + x_a\right)^2} \tag{3.14}$$

$$f_{a2} = \cos\beta \frac{k i_{a2}^2}{\left(h - x_a\right)^2} \tag{3.15}$$

$$f_{a3} = \cos\beta \frac{k i_{a3}^2}{\left(h + y_a\right)^2} \tag{3.16}$$

$$f_{a4} = \cos\beta \frac{k i_{a4}^2}{\left(h - y_a\right)^2} \tag{3.17}$$

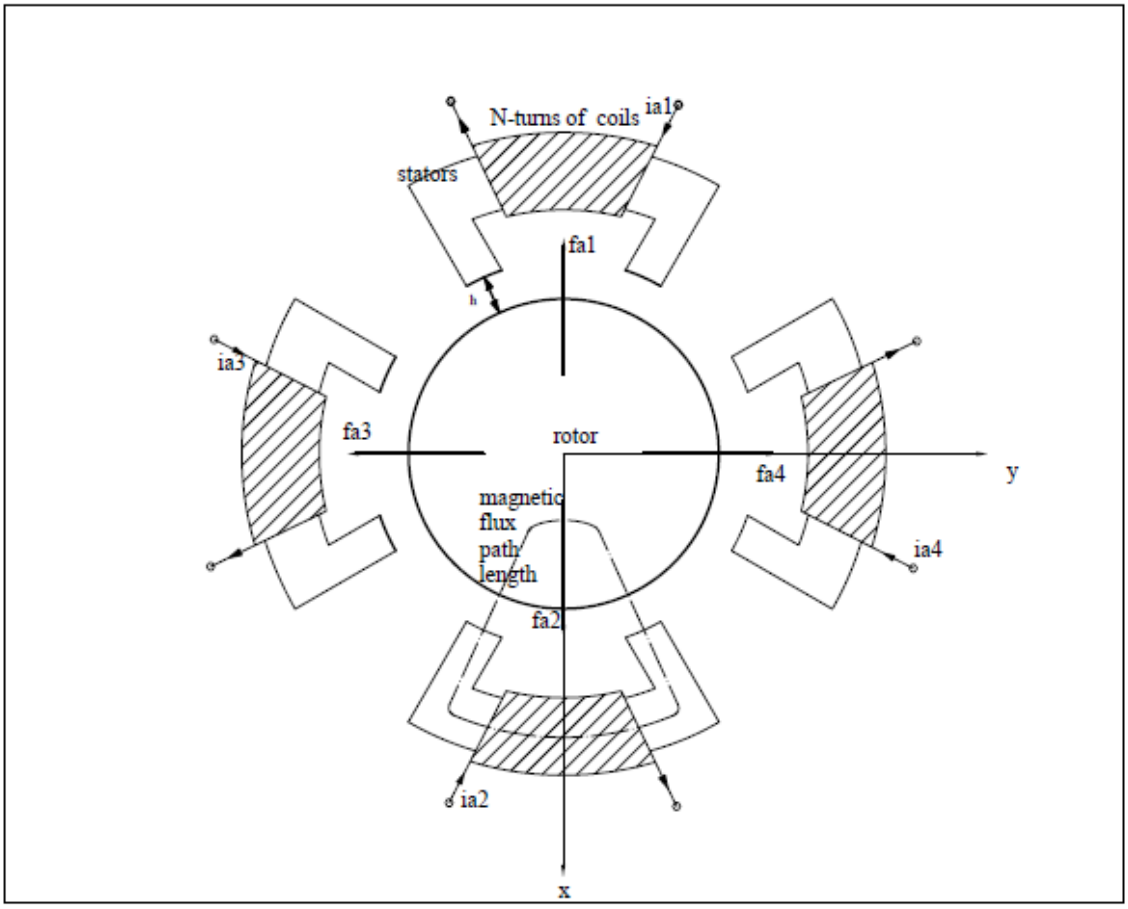

Fig. 3.3 Cross-section of bearing A

The forces generated in Bearing B can also be seen in Fig 3.4 they are similar as follows:

$$f_{b1} = \cos\beta \frac{ki_{b1}^2}{\left(h + x_b\right)^2} \tag{3.18}$$

$$f_{b2} = \cos\beta \frac{ki_{b2}^2}{\left(h - x_b\right)^2} \tag{3.19}$$

$$f_{b3} = \cos\beta \frac{ki_{b3}^2}{\left(h + y_b\right)^2} \tag{3.20}$$

$$f_{b4} = \cos\beta \frac{k i_{b4}^2}{\left(h - y_b\right)^2} \tag{3.21}$$

where $k = \dfrac{\mu_0 N^2 A_g}{4}$ is the magnetic force parameter.

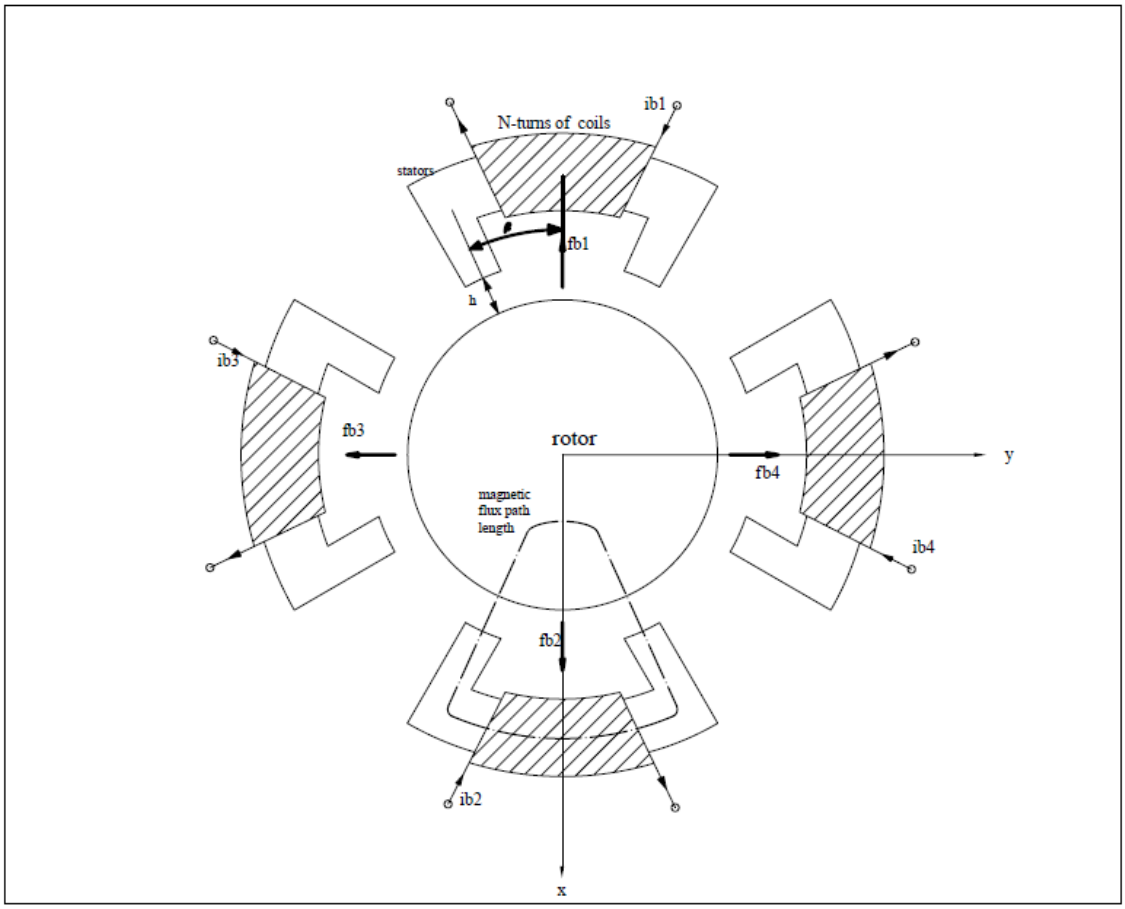

Fig. 3.4 Cross-section of bearing B

3.2 State-Variable Representation

Applying notations $x = x_1$, $\dot{x} = x_2$, $y = y_1$, $\dot{y} = y_2$, $\theta = \theta_1$, $\dot{\theta} = \theta_2$, $\psi = \psi_1$, $\dot{\psi} = \psi_2$, $\omega = \dot{\phi}$ to Eqs. (2.20)-(2.23), (2.24)-(2.27), (2.28)-(2.31), and (3.14)-(3.21), the state-

variable representation of the AMB-rotor model system is then

$$\dot{x}_1 = x_2 \tag{3.22}$$

$$\dot{x}_2 = \frac{1}{m_r}\left(f_{ax} + f_{bx} + f_{dx} + \delta_x(t)\right) \tag{3.23}$$

$$\dot{y}_1 = y_2 \tag{3.24}$$

$$\dot{y}_2 = \frac{1}{m_r}(f_{ay} + f_{by} + f_{dy}) \tag{3.25}$$

$$\dot{\theta}_1 = \theta_2 \tag{3.26}$$

$$\dot{\psi}_1 = \psi_2 \tag{3.27}$$

$$f_{dx} = m_r \mu \omega^2 \sin(\omega t) \tag{3.28}$$

$$f_{dy} = m_r \mu \omega^2 \cos(\omega t) \tag{3.29}$$

$$\dot{\theta}_2 = \left(\frac{I_p}{I_r}\right)\omega\psi_2 - \psi_2 \sin\theta_1 + \left(\frac{I_p}{I_r}\right)\psi_2^2 \sin\theta_1 + \frac{l}{2I_r}\left(-f_{ax} + f_{bx} + f_{d\theta}\right) \tag{3.30}$$

$$\dot{\psi}_2 = -\frac{I_p}{I_r}\omega\theta_2 - \frac{I_p}{I_r}\psi_2\theta_2 \sin\theta_1 + \psi_2\theta_2 \sin\theta_1 - \psi_2{}^2 \sin\theta_1 \cos(\omega t)(\sin(\omega t) - \cos\theta_1) + \frac{l}{2I_r}\left(f_{ay} - f_{by} + f_{d\psi}\right) \tag{3.31}$$

$$f_{d\theta} = {}^{2\left(I_p - I_r\right)}\!\Big/_{l}\ \tau\omega^2 \cos(\omega t) \tag{3.32}$$

$$f_{d\psi} = {}^{2\left(I_p - I_r\right)}\!\Big/_{l}\ \tau\omega^2 \sin(\omega t) \tag{3.33}$$

$$f_{ax} = f_{a1} - f_{a2} + \alpha\left(\frac{x_a}{h}\right)\left(f_{a3} + f_{a4}\right)$$

$$= k\cos\beta\left(\frac{i_{a1}^2}{(h+(x_1+\frac{l}{2}\sin\theta_1))^2} - \frac{i_{a2}^2}{(h-(x_1+\frac{l}{2}\sin\theta_1))^2} + \alpha\left(\frac{i_{a3}^2}{(h+(y_1+\frac{l}{2}\sin\psi_1))^2} + \frac{i_{a4}^2}{(h-(y_1+\frac{l}{2}\sin\psi_1))^2}\right)\right)$$

(3.34)

$$f_{bx} = f_{b1} - f_{b2} + \alpha\left(\frac{x_b}{h}\right)\left(f_{b3} + f_{b4}\right)$$

$$= k\cos\beta\left(\frac{i_{b1}^2}{(h+(x_1-\frac{l}{2}\sin\theta_1))^2} - \frac{i_{b2}^2}{(h-(x_1-\frac{l}{2}\sin\theta_1))^2} + \alpha\left(\frac{i_{b3}^2}{(h+(y_1-\frac{l}{2}\sin\psi_1))^2} + \frac{i_{b4}^2}{(h-(y_1-\frac{l}{2}\sin\psi_1))^2}\right)\right)$$

(3.35)

$$f_{ay} = f_{a3} - f_{a4} + \alpha\left(\frac{y_a}{h}\right)\left(f_{a1} + f_{a2}\right)$$

$$= k\cos\beta\left(\frac{i_{a3}^2}{(h+(y_1+\frac{l}{2}\sin\psi_1))^2} - \frac{i_{a4}^2}{(h-(y_1+\frac{l}{2}\sin\psi_1))^2} + \alpha\left(\frac{i_{a1}^2}{(h+(x_1+\frac{l}{2}\sin\theta_1))^2} + \frac{i_{a2}^2}{(h-(x_1+\frac{l}{2}\sin\theta_1))^2}\right)\right)$$

(3.36)

$$f_{by} = f_{b3} - f_{b4} + \alpha\left(\frac{y_b}{h}\right)\left(f_{b1} + f_{b2}\right)$$

$$= k\cos\beta\left(\frac{i_{b3}^2}{(h+(y_1-\frac{l}{2}\sin\psi_1))^2} - \frac{i_{b4}^2}{(h-(y_1-\frac{l}{2}\sin\psi_1))^2} + \alpha\left(\frac{i_{b1}^2}{(h+(x_1-\frac{l}{2}\sin\theta_1))^2} + \frac{i_{b2}^2}{(h-(x_1-\frac{l}{2}\sin\theta_1))^2}\right)\right)$$

(3.37)

Eqs. (3.22) - (3.33) describe the mechanical dynamics, while Eqs. (3.34) - (3.37) govern the electro-magnetic force dynamics. It is noted that functions $\delta_x(t)$ are the external excitations applied along the x-axis.

CHAPTER IV

CONTROLLER DESIGN

4.1 Nonlinear Time-frequency Control Theory

Nonlinear control of active magnetic bearings and magnetic levitation systems was studied in [22] and [23] in which linearization was employed. In this thesis, a novel control scheme is developed and applied to the AMB-rotor system model elaborated in the previous chapters. The scheme utilizes the discrete wavelet transformation (DWT) and Filtered-x LMS algorithm (FXLMS) to build a controller dedicated to the control of the system. The controller is developed without resorting to linearization. With the incorporation of the FXLMS algorithm, the mathematical singularity and physical instability at uncontrollable frequencies are avoided. The algorithm ensures the updating of controller in *real-time* and also guarantees a desired system response at all time.

The novel control scheme consists of two major components: DWT and least-mean-square adaptive filters to realize feed-forward control and on-line identification. Generally, the DWT can be expressed as a two-channel filters as shown in Fig 4.1.

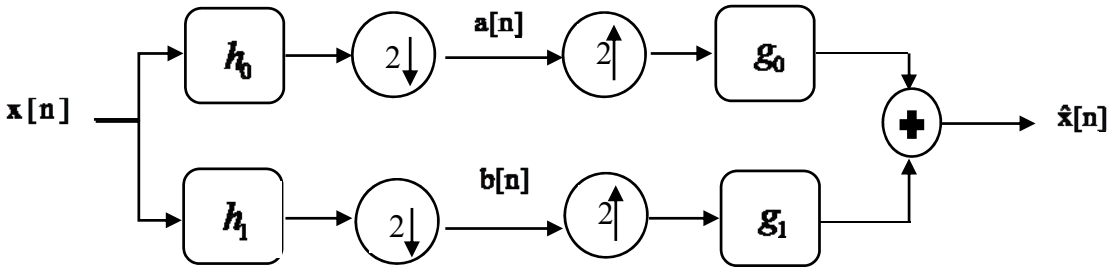

Fig. 4.1 Two-channel filter bank

The approximation, a[n], and detail, b[n], coefficients can be calculated as follows:

$$a[n] = \sum_k h_0[2n-k]x[k] = \sum_k h_0[k]x[2n-k] \tag{4.1}$$

$$d[n] = \sum_k h_1[2n-k]x[k] = \sum_k h_1[k]x[2n-k] \tag{4.2}$$

where $n = 0,1,2\ldots\infty$. Assume that the length of the high-pass filter and the low-pass filters are both 4, Eqs. (4.1) and (4.2) can be expressed as:

$$Y = T_a X \tag{4.3}$$

where T_a is the infinite analysis matrix of the following form:

$T_a =$

$$\begin{bmatrix}
\ddots & \ddots & \ddots & \ddots & \ddots & \ddots & & & & & & & & \\
\cdots & 0 & h_0[3] & h_0[2] & h_0[1] & h_0[0] & 0 & 0 & 0 & 0 & 0 & 0 & 0 & \cdots \\
\cdots & 0 & 0 & 0 & h_0[3] & h_0[2] & h_0[1] & h_0[0] & 0 & 0 & 0 & 0 & 0 & \cdots \\
\cdots & 0 & 0 & 0 & 0 & 0 & h_0[3] & h_0[2] & h_0[1] & h_0[0] & 0 & 0 & 0 & \cdots \\
\cdots & 0 & 0 & 0 & 0 & 0 & 0 & 0 & h_0[3] & h_0[2] & h_0[1] & h_0[0] & 0 & \cdots \\
 & \vdots & \vdots & \vdots & \vdots & \vdots & \vdots & \vdots & \vdots & \vdots & \vdots & \vdots & \vdots & \\
\cdots & 0 & h_1[3] & h_1[2] & h_1[1] & h_1[0] & 0 & 0 & 0 & 0 & 0 & 0 & 0 & \cdots \\
\cdots & 0 & 0 & 0 & h_1[3] & h_1[2] & h_1[1] & h_1[0] & 0 & 0 & 0 & 0 & 0 & \cdots \\
\cdots & 0 & 0 & 0 & 0 & 0 & h_1[3] & h_1[2] & h_1[1] & h_1[0] & 0 & 0 & 0 & \cdots \\
\cdots & 0 & 0 & 0 & 0 & 0 & 0 & 0 & h_1[3] & h_1[2] & h_1[1] & h_1[0] & 0 & \cdots \\
 & & & & & & & & \ddots & \ddots & \ddots & \ddots & \ddots & \ddots
\end{bmatrix}$$

(4.4)

Since X is the infinite array signal, Y can be expressed as:

$$Y = [\cdots, a[0], a[1], a[3], d[0], d[1], d[2], \cdots]^T \tag{4.5}$$

In [24], a procedure named periodization is employed to substitute the infinite input signal as a finite one as follows

$$X^N = [x[0], x[1], x[2], \cdots, x[N-1], x[N]]^T \tag{4.6}$$

Since the input signal is truncated in this operation, T_a, the analysis matrix, also needs to be truncated as an $N \times N$ matrix, T_a^N. The truncated filter coefficients are put back into a proper positon in the matrix to make the signal consistent with the periodic signal. Eq. (4.4) then takes up the form below

$$Y_{p+1}^N = T_a^X X_p^N \tag{4.7}$$

where p is the decomposition level. In this research, a second level decomposition is considered. For $N = 8$, the truncated analysis matrix is

$T_a^X =$

$$\begin{bmatrix} h_0[3] & h_0[2] & h_0[1] & h_0[0] & 0 & 0 & 0 & 0 \\ 0 & 0 & h_0[3] & h_0[2] & h_0[1] & h_0[0] & 0 & 0 \\ 0 & 0 & 0 & 0 & h_0[3] & h_0[2] & h_0[1] & h_0[0] \\ h_0[1] & h_0[0] & 0 & 0 & 0 & 0 & h_0[3] & h_0[2] \\ h_1[3] & h_1[2] & h_1[1] & h_1[0] & 0 & 0 & 0 & 0 \\ 0 & 0 & h_1[3] & h_1[2] & h_1[1] & h_1[0] & 0 & 0 \\ 0 & 0 & 0 & 0 & h_1[3] & h_1[2] & h_1[1] & h_1[0] \\ h_1[1] & h_1[0] & 0 & 0 & 0 & 0 & h_1[3] & h_1[2] \end{bmatrix} \tag{4.8}$$

Eq. (4.7) can be rearranged using Eq. (4.8) into a concise form

$$\begin{bmatrix} A_{p+1} \\ D_{p+1} \end{bmatrix} = T_a^N X_p^N \tag{4.9}$$

with

$$A_{p+1} = \left[a[0] \quad a[1] \quad \cdots \quad a[N/2 - 1] \right]^T \tag{4.10}$$

$$D_{p+1} = \left[d[0] \quad d[1] \quad \cdots \quad d[N/2 - 1] \right]^T \tag{4.11}$$

The synthesis can be expressed as:

$$T_a^N T_s^N = I^N \tag{4.12}$$

where I^N is the identity matrix, meaning that

$$T_s^N = \left(T_a^N \right)^{-1} \tag{4.13}$$

When $p = 0$, Eq. (4.9) is defined as the first level decomposition. The second level decomposition can be expressed as follows

$$\begin{bmatrix} A_{p+2} \\ D_{p+2} \\ D_{p+1} \end{bmatrix} = \begin{bmatrix} T_a^{N/2} & 0 \\ 0 & I^{N/2} \end{bmatrix} T_a^N X_p^N \tag{4.14}$$

FXLMS is effective in noise reduction, in which adaptive filters use the noise near the sound source as the reference to generate a compensating signal to cancel the noise. The residual error is then used to adapt (update) the coefficients of the active filter to minimize the mean-square-error in real-time. In this section, the wavelet transformation matrix is employed to transform an input signal into its corresponding wavelet coefficient array. The scheme is demonstrated using the architecture shown in Fig. 4.2. In the figure the input signal x(n) is the electric current that runs through the AMB-rotor system. d(n) is the desired displacement of the rotor at where the two magnetic bearings are mounted,

which is set to be 0. $u(n)$ is the current after being controlled. To incorporate the $N \times N$ analysis matrix, the signal vector is digitized as follows

$$X(n) = [x(n), x(n-1) \cdots, x(n-N+1)]^T \tag{4.15}$$

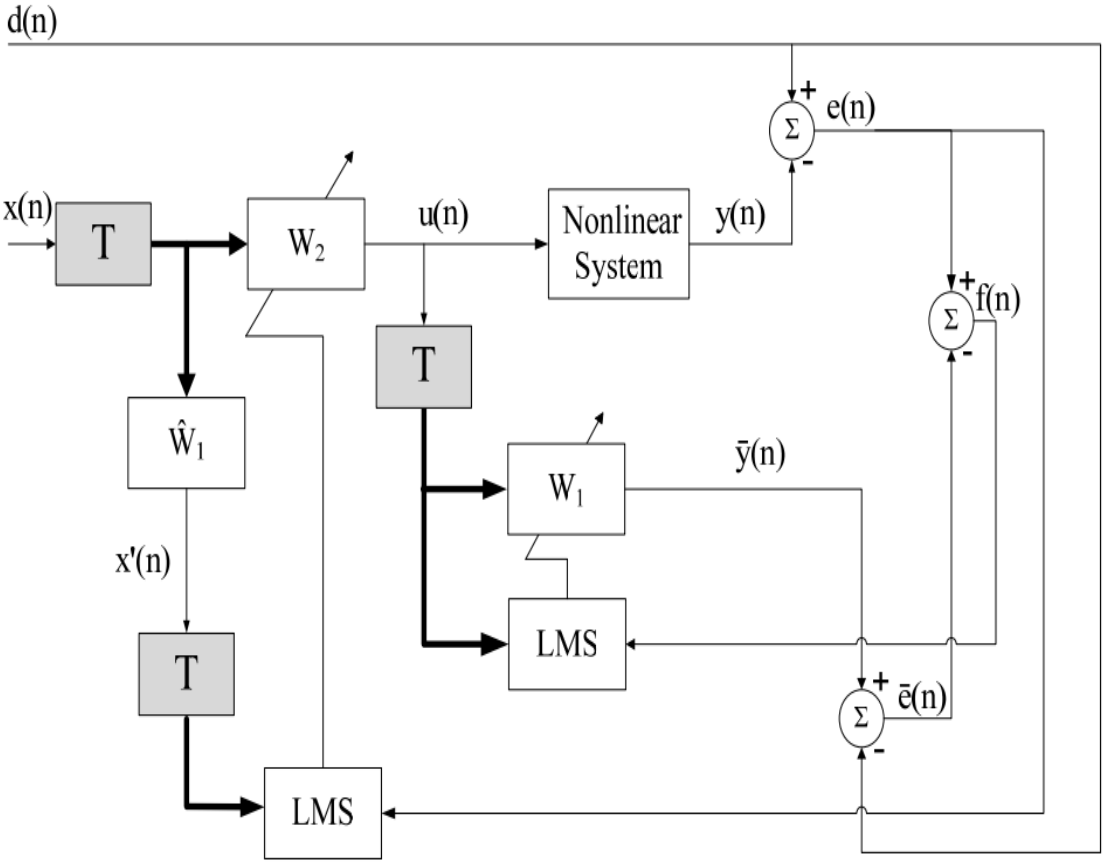

Fig. 4.2 Architecture of wavelet based time-frequency controller

$$U(n) = [u(n), u(n-1) \cdots, u(n-N+1)]^T \tag{4.16}$$

$$X'(n) = [x'(n), x'(n-1) \cdots, x'(n-N+1)]^T \tag{4.17}$$

$$E(n) = [e(n), e(n-1) \cdots, e(n-N+1)]^T \tag{4.18}$$

$$F(n) = [f(n), f(n-1)\cdots, f(n-N+1)]^T \tag{4.19}$$

All the vectors are first-in-last-out arrays (FILO), i.e. the N-th data is replaced by the incoming one. Hence one vector shares most of the terms with the last one. The first adaptive filter W_1 aims to identify the instability including chaotic response of the system on-line. The second adaptive filter W_2 aims to adapt the weight on-line, thus preforming as a feed-forward controller.

The weights of the two filters are

$$W_1(n) = [w_{1,0}(n), w_{1,1}(n-1), \cdots, w_{1,N-1}(n-N+1)]^T \tag{4.20}$$

$$W_2(n) = [w_{2,0}(n), w_{2,1}(n-1), \cdots, w_{2,N-1}(n-N+1)]^T \tag{4.21}$$

$\bar{e}(n)$, the identification error between the desired displacement d(n) and the output from the adaptive filter, W_1, are calculated as

$$\bar{e}(n) = \bar{y}(n) - d(n) \tag{4.22}$$

in which $\bar{y}(n)$ can be expressed using Eq. (4.23) below

$$\bar{y}(n) = W_1^T(n) TU(n) \tag{4.23}$$

The error between the desired displacement of the rotor and the output of W_2 is

$$e(n) = y(n) - d(n) \tag{4.24}$$

The difference between the 'identification error' and the 'error' is therefore

$$f(n) = e(n) - \bar{e}(n) \tag{4.25}$$

The weights of the two adaptive filters are updated by a least- mean-square algorithm as follows

$$W_1(n+1) = W_1(n) - \mu_1 TU(n) f(n) \tag{4.26}$$

$$W_2(n+1) = W_2(n) + \mu_2 TX'(n) f(n) \tag{4.27}$$

where $x'(n) = W_1^T(n) TX(n)$, and μ_1, μ_2 are filter step sizes.

4.2 Controller Configuration and Control Scheme

Each electromagnet is controlled individually. Hence a total of eight controllers are employed. The electric current provided to each electromagnet is a combination of the control current (controlled by the dedicated controller) and the bias current added to the coil. The current running through the coils of each magnet is therefore not a constant but rather varying as follows

$$i_{an} = i_{bias} + i_{can}, \quad n = 1,2,3,4 \tag{4.28}$$

$$i_{bm} = i_{bias} + i_{cbm}, \quad m = 1,2,3,4 \tag{4.29}$$

where $i_{bias} = 2A$ is biased from the power supply, $i_{ref,can}$ and $i_{ref,cbm}$ are the currents before control, which is constant at $0.5A$, and i_{can}, i_{cbm} are the currents after control.

The following flow chart depicts the control logic developed for the control of the AMB-rotor model system.

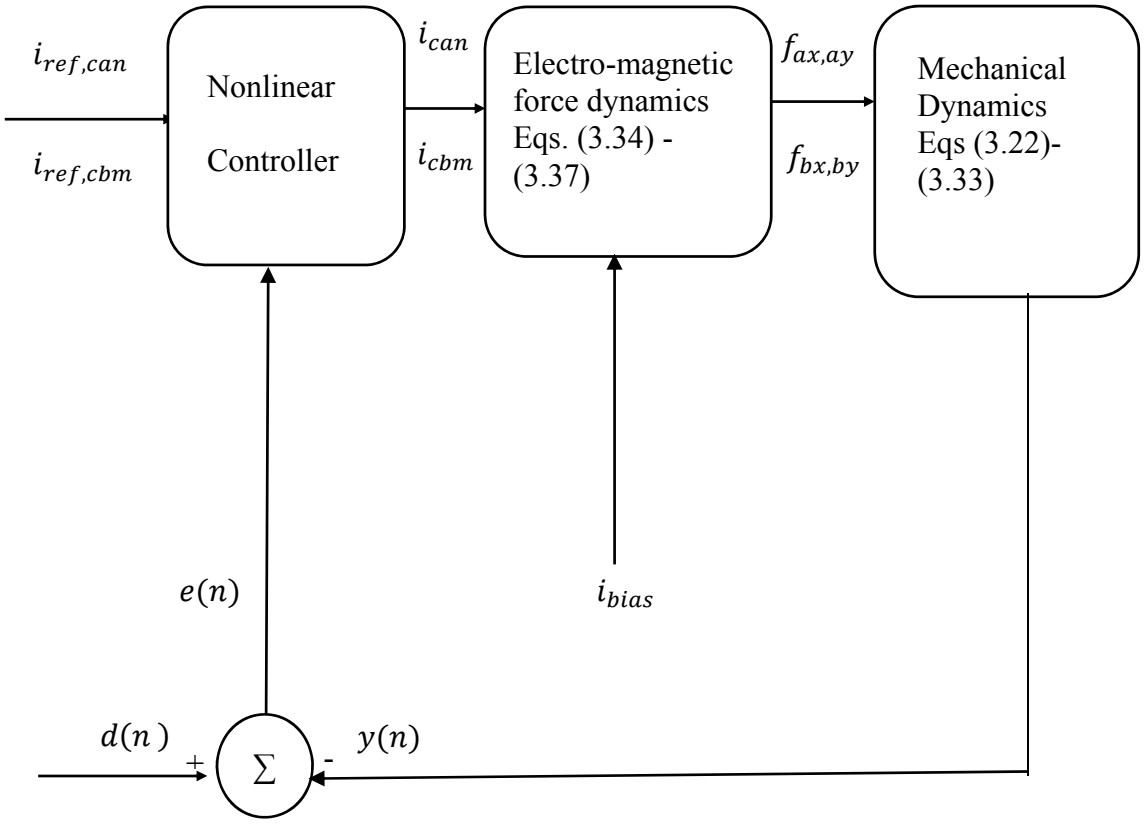

Fig. 4.3 Control flow chart

In the Fig.4.3, $d(n)$ is the desired response of the rotor and $y(n)$ is the output response. It is understood that the current input to the electro-magnetic force dynamics equations is the sum of the bias current and the current after control, i.e. i_{an} and i_{bn}, which followed from Eqs. (4.28)- (4.29).

CHAPTER V

NUMERICAL RESULTS AND DISCUSSION

In this chapter, the control of the AMB-rotor model system is performed using a 0.00001s integration step size in the MATLAB/Simulink environment. System responses with and without considering gyroscopic effect and geometry coupling are discussed in the first two sections of the chapter. The maximum speed within which the AMB-rotor system maintains a specified range of vibrations is determined in the time-domain using the system's time response. This specified range of vibrations is set to be one-fourth of the air-gap. The effectiveness of the controller design is demonstrated under the particular speed using visualization tools including phase portraits and Poincare sections. In the third part of Chapter V the control scheme developed for the AMB-rotore system is validated in the simultaneous time-frequency domain by employing instantaneous frequency (IF). An external impact of 5,000 m/s^2 in magnitude and 0.001s in duration is also applied at 0.1s while the system is operating at 187,500rpm. Controlled responses to the impulse are discussed in the final section. Table 5.1 tabulates all the system parameters used to generate the results found in the following sections.

Table 5.1 System parameters

Parameters	**Symbol**	**Value**	**Unit**
Mass of rotor	m	13.9	kg
Polar moments of Inertia	I_p	1.34×10^{-2}	$kg\cdot m^2$
Radial moment of Inertia	I_r	2.32×10^{-1}	$kg\cdot m^2$
Area of coil	A_g	1.532×10^{-3}	m^2
Nominal air gap	h	0.55	*millimeters*
Coil resistance	R	10.7	*ohm*
Nominal coil inductance	L	2.85	*miliHenry*
Number of turns of coil	N	400	*Turns*
Permeability of free space	μ_0	$4\pi\times10^{-7}$	$Henry/meter$
Magnetic force parameters	k	7.7×10^{-5}	Nm^2/A
Excitation signal at X-direction	$\delta_x(t)$	5000	m/s^2
Excitation signal at Y-direction	$\delta_y(t)$	0	m/s^2
Static eccentricity	ε	1×10^{-5}	*meter*
Dynamic eccentricity	τ	4×10^{-4}	*rad*
Geometry coupling parameter	α	0.414	*NULL*

5.1 System Responses with and without Gyroscopic Effect

Gyroscopic effect, which is characteristic of all spinning shafts (rotors), is commonly ignored in rotor-dynamic modeling [9, 10]. When the rotor is short, the assumption of negligible gyroscopic effect is acceptable because the displacements at both ends of the rotor are almost identical. However, for the case of the long flexible rotor considered in this thesis, the displacements at either end of the rotor are non-negligibly different. With the controller off-line and no external perturbation applied, the impact of disregarding gyroscopic effect is considered when the model system is operating at 15,000rpm. In the followings the case of without considering gyroscopic effect is made through setting both the polar and radial moments of inertia to zero.

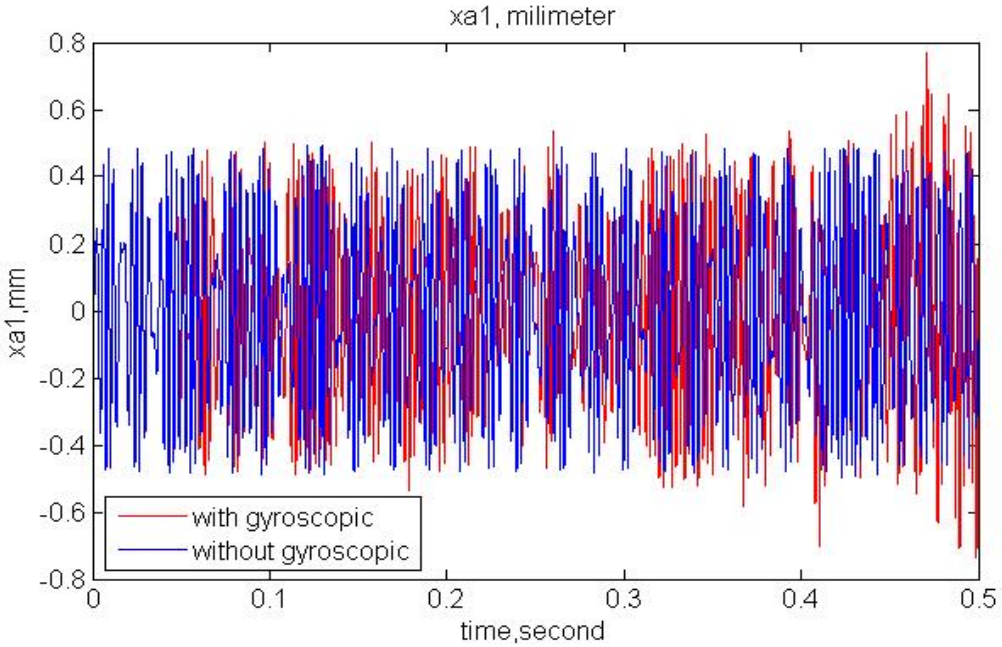

Fig. 5.1 Displacements of rotor at bearing A in X-direction with and without gyroscopic effect at 15,000rpm

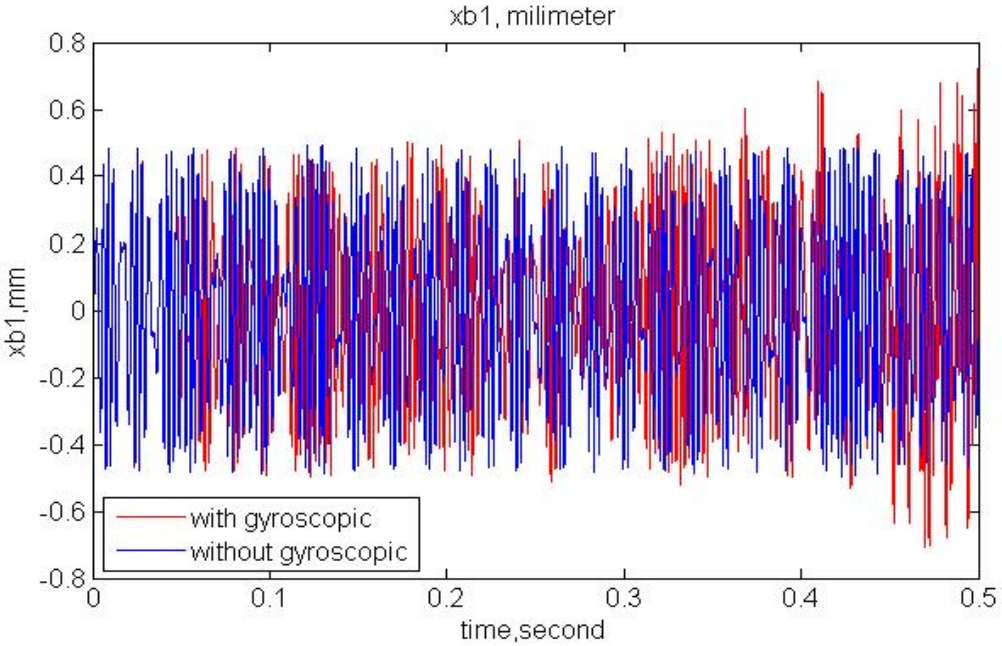

Fig. 5.2 Displacements of rotor at bearing B in X-direction with and without gyroscopic effect at 15,000rpm

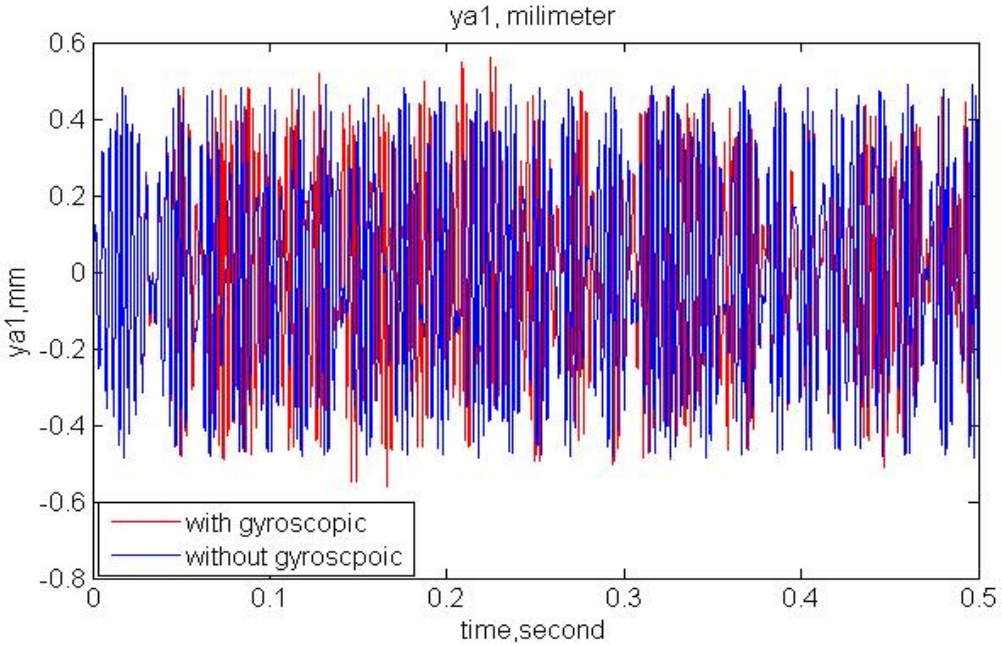

Fig. 5.3 Displacements of rotor at bearing A in Y-direction with and without gyroscopic effect at 15,000rpm

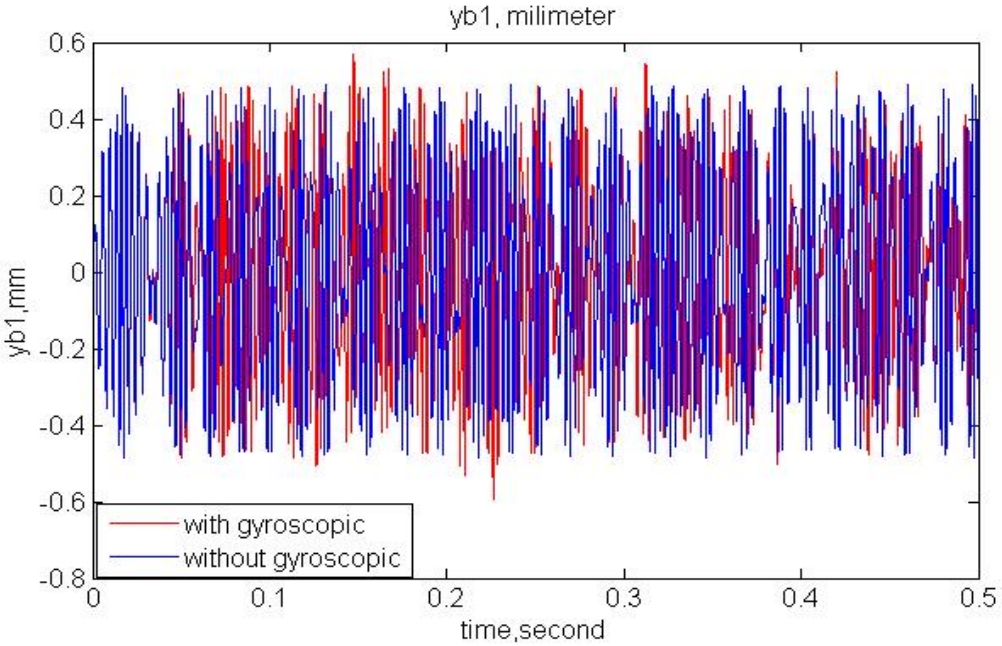

Fig. 5.4 Displacements of rotor at bearing B in Y-direction with and without gyroscopic effect at 15,000rpm

The responses of the AMB-rotor system that consider gyroscopic effect are plotted in Figs. 5.1-5.4 against their counterparts that do not. Since gyroscopic effect is not accounted for, the displacement components at both bearing locations are identical. Consequently the blue response lines in Figs. 5.1 and 5.2 are found to be the same. The same observation can be made with the blue lines in Figs. 5.3 and 5.4. Unlike the case without considering gyroscopic effect, the time responses in red that correspond to retaining gyroscopic effect are different in each case. The deviation of the red lines from the blue ones in Figs. 5.1-5.4 is significant enough to suggest that the dynamics of the rotor as described by the cases in which gyroscopic effect is disregarded is fundamentally different from the cases that consider the effect. This is further confirmed by the spectral responses in Fig. 5.5 which demonstrate different dynamic signatures.

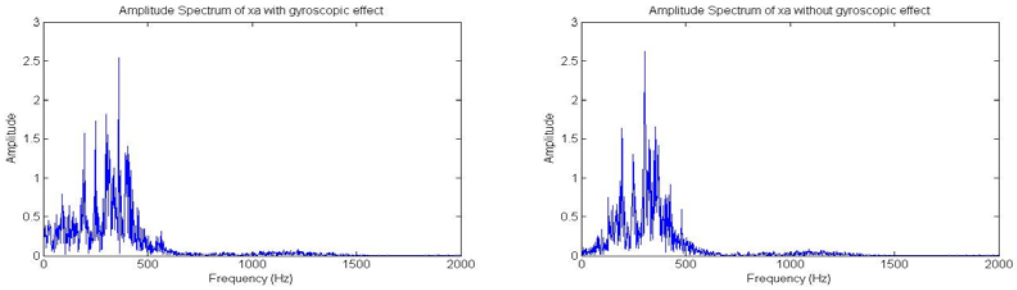

(a)

(e)

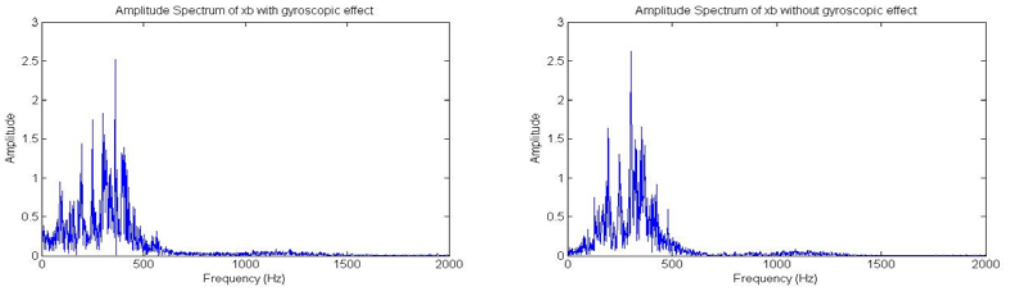

(b)

(f)

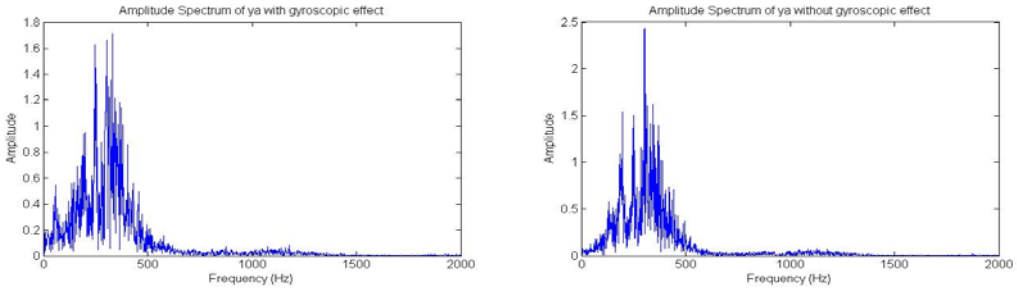

(c)

(g)

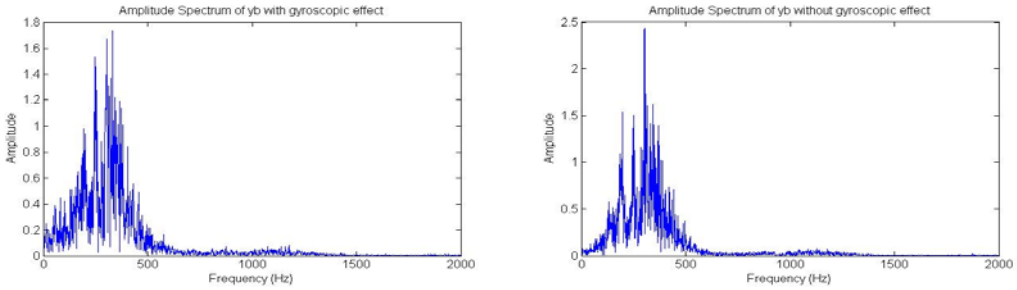

(d)

(h)

Fig. 5.5 Spectral responses of model with gyrosopic effect (a)-(d) and without gyrosopic effect (e)-(h)

In addition to the noted disagreements in the time responses, the statement that considering gyroscopic effect or not renders different dynamics is further supported by re-examining Figs. 5.1 and 5.2 up close. While the time responses of the cases without gyroscopic effect are all bounded, the time responses with gyroscopic effect are not. The corresponding vibration amplitude is seen to increase with time, thus portraying a state of motion that is characteristically dissimilar to the state described by the blue lines. Also, it is seen that the oscillation frequencies and spectra are not identical. The implication of dropping gyroscopic effect in rotor-dynamic modeling is particularly consequential in misinterpreting the true characteristics of the rotor at high speed. Given such prominent disagreements and the potential risk of generating misleading results, it is only proper that gyroscopic effect is considered throughout the rest of the chapter.

5.2 System Responses without and with Geometry Coupling

As shown in Fig. 3.3, the radial component of the electromagnetic force generated by the magnet has two sets of orthogonal components, f_{p1} and f_{n1} , f_{p2} and f_{n2} . When the geometric center of the rotor is not aligned with the bearing center, the symmetry of the 2 components along the y-axis, f_{p1} and f_{p2} , is broken, thus resulting in varying resultant forces of elevation, f_a and f_b , in Bearings A and B. This effect is accounted for by employing the geometry coupling parameter α which was previously defined in Chapter III. Given the 8-magnet configuration of the AMB system explored in this study, the angle of the magnet is therefore $\beta = \pi / 8$. Hence, $\alpha = \tan(\beta) = 0.414$.

The primary objective of the section is to determine the impact of the geometry coupling parameter on the system response. Knowledge to be established as to whether the parameter can be ignored is essential to the accurate control of the AMB-rotor system. In the followings, two cases, namely $\alpha = 0.414$ and $\alpha = 0$, are considered for the AMB-rotor model system running at 15,000rpm with the developed controller off-line and the gyroscopic effect being retained.

When the geometry coupling parameter is taken as zero in Fig. 3.3, the horizontal force component vanishes, thus risking overestimating the elevation force, *f*, and underestimating the dynamics of the rotor along the horizontal direction. Figs. 5.6-5.9 give the comparisons of the displacement responses of the model system at the 2 bearing locations, where the red lines correspond to the cases when geometry coupling is considered, while the blue lines are the time histories correspond to without geometry coupling. The corresponding frequency responses are also examined in the Fourier domain. Fig.5.10 provides a visual comparison of the spectra, with the column on the left-hand side demonstrating a spectral signature that is definitively different from the one associated with the column on the right-hand side.

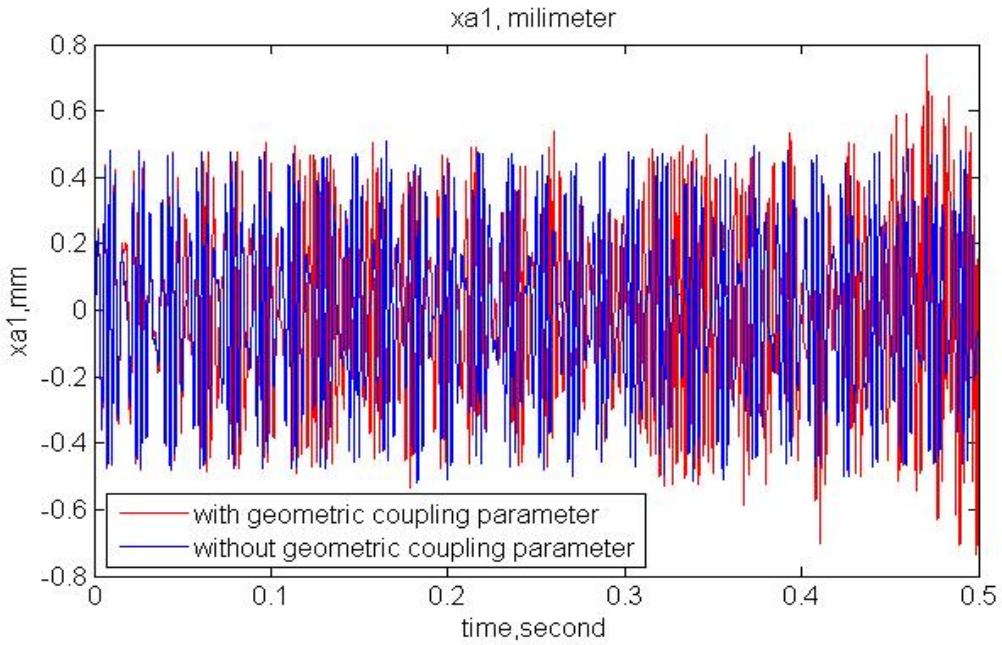

Fig. 5.6 Comparison of rotor displacements at bearing A in X-direction for $\alpha = 0$ and $\alpha = 0.414$ with gyroscopic effect at 15,000rpm

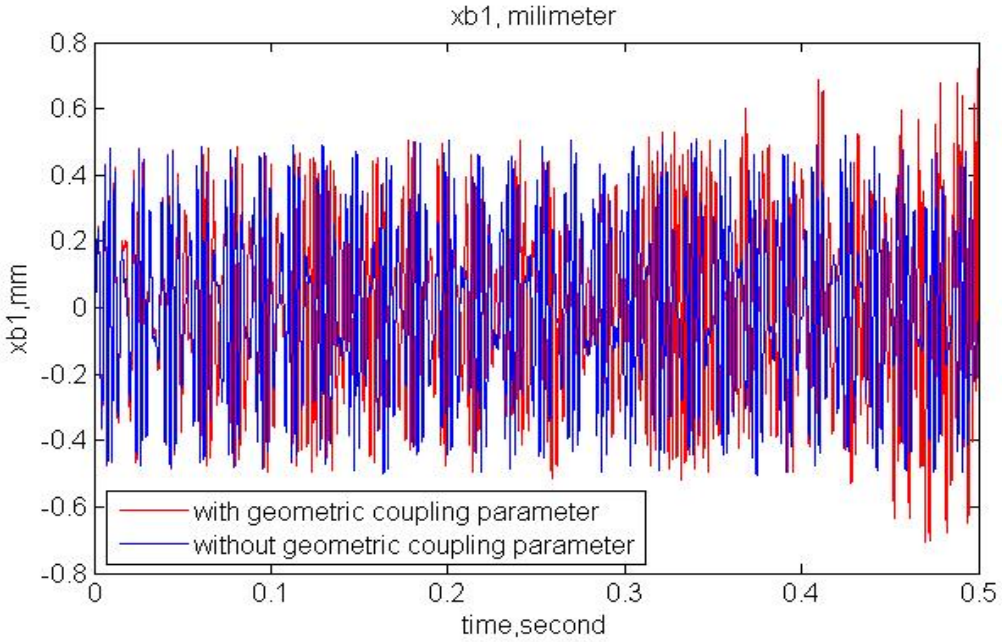

Fig. 5.7 Comparison of rotor displacements at bearing B in X-direction for $\alpha = 0$ and $\alpha = 0.414$ with gyroscopic effect at 15,000rpm

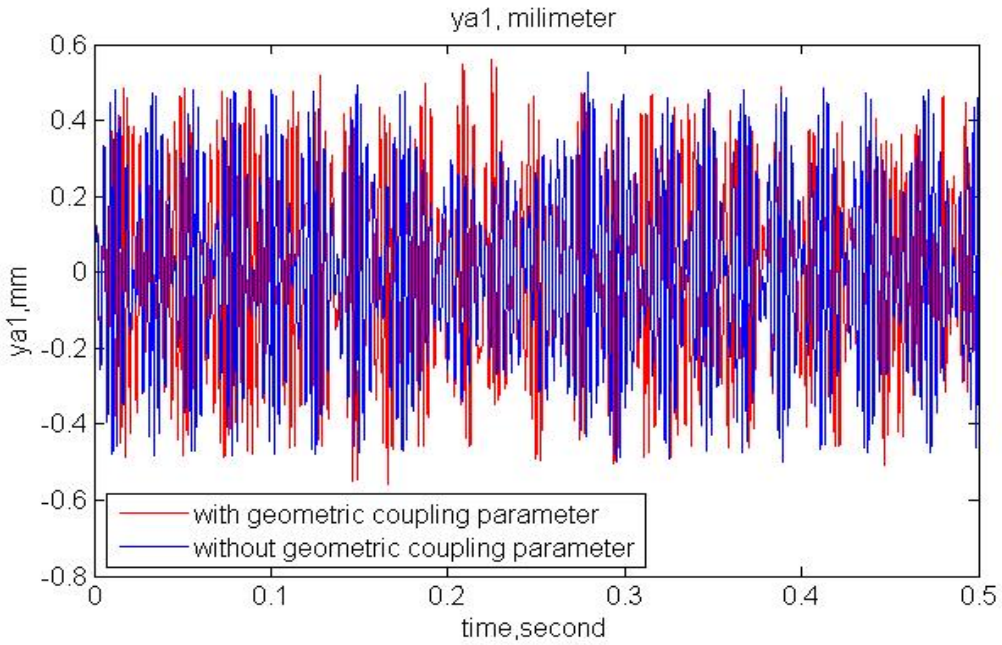

Fig. 5.8 Comparison of rotor displacements at bearing A in Y-direction for $\alpha = 0$ and $\alpha = 0.414$ with gyroscopic effect at 15,000rpm

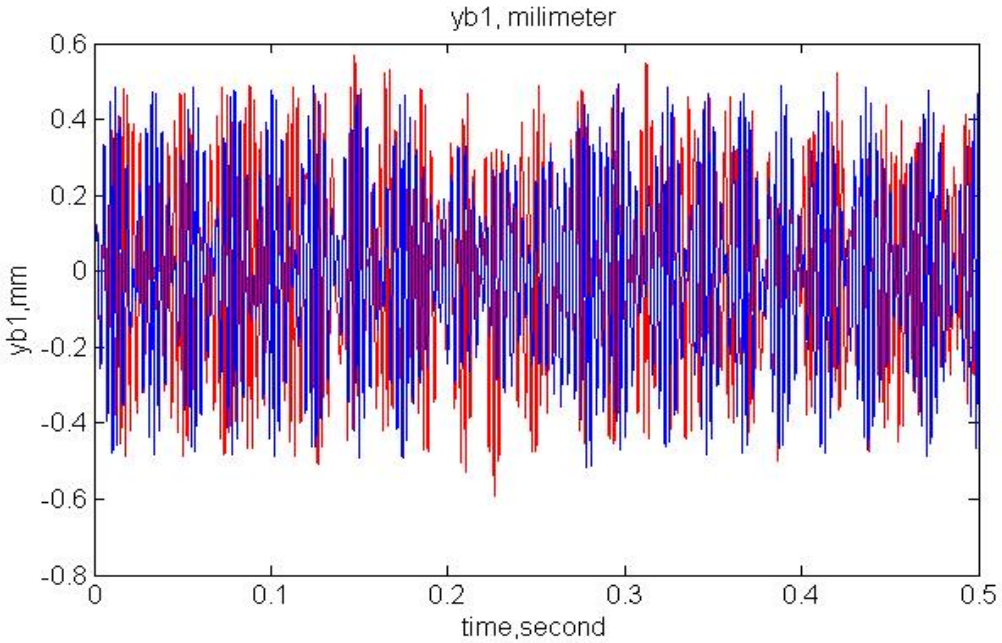

Fig. 5.9 Comparison of rotor displacements at bearing B in Y-direction for $\alpha = 0$ and $\alpha = 0.414$ with gyroscopic effect at 15,000rpm

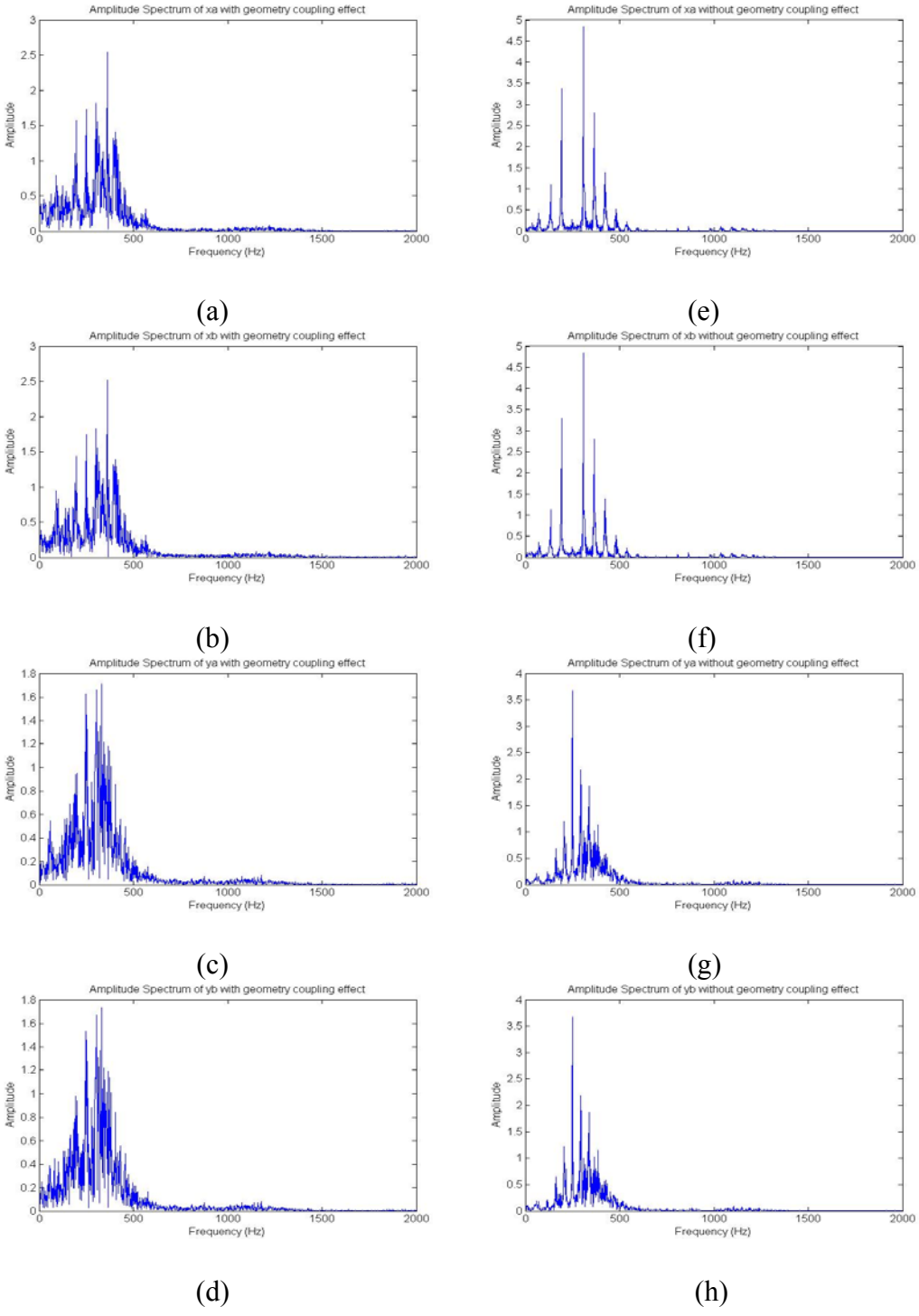

Fig. 5.10 Spectral responses of model with geometry coupling (a)-(d) and without geometry coupling (e)-(h)

It is evident that the time and frequency responses of the two cases differ at the fundamental level. Since the horizontal force components, f_{n1} and f_{n2}, are both nonexistent when geometry coupling is ignored, the dynamics manifested through vibration amplitude and oscillation frequency is not in agreement with the motion states described by the red lines. The disagreement is most noted in the frequency domain in in Fig. 5.10, thus indicative of 2 distinctive sets of inherent characteristics. Similar to the conclusion drawn in the previous section, the implication of disregarding geometry coupling in AMB modeling is in erroneously describing the true dynamics of the rotor at high speed. Such prominent disagreements could very well lead to physically erroneous description of the rotor behavior. Geometry coupling is therefore considered in the study to avoid bearing the risk of misinterpretation.

5.3 Performance of Controller Design

With the rotor being flexible, whirling becomes prominent with increasing speed and, as a direct result, serves to aggravate the vibrations of the rotor. It is crucial for the vibration amplitude of the AMB supported rotor to be controlled with desired accuracy. To mitigate the impact due to whirling so as to ensure the proper control of the AMB-rotor system, the displacement of the rotor needs to be controlled within a specified tolerance. The tolerance specified for the study is 0.1375 mm, which is 25% of the air gap. With the controller on-line, the maximum speed at which the displacement of the rotor abides to the desired tolerance is found to be 187,500rpm. A 20% lower speed at

150,000rpm is also considered alongside this maximum speed of 187,500rpm to provide contrast and, in so doing, to examine the performance of the controller design in controlling the highly nonlinear system whose response is also highly non-stationary at such extreme speeds.

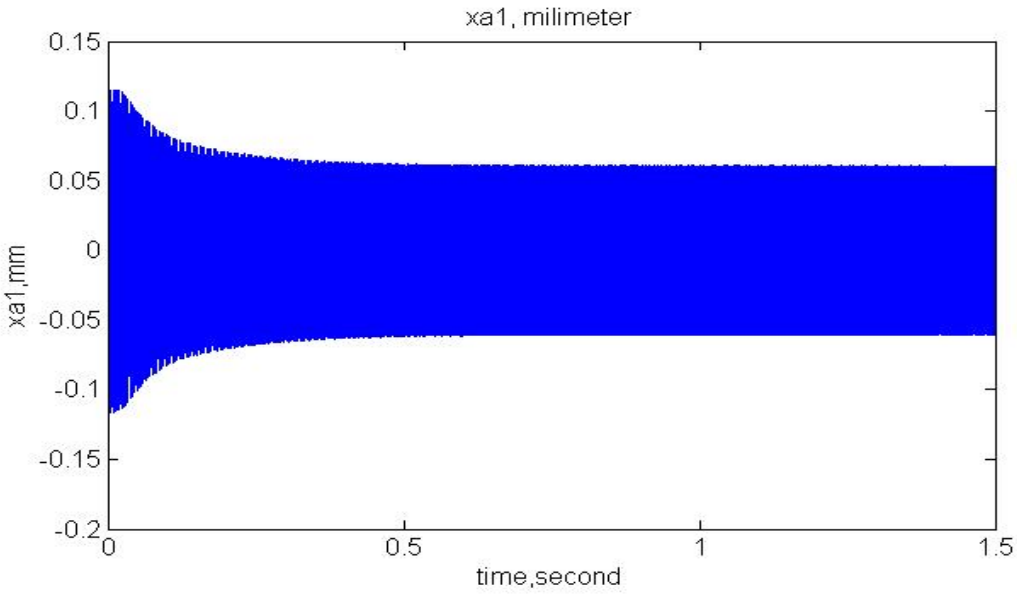

Fig. 5.11 Rotor displacement at bearing A in X-direction with $\alpha = 0.414$ and gyroscopic effect at 187,500rpm (controlled)

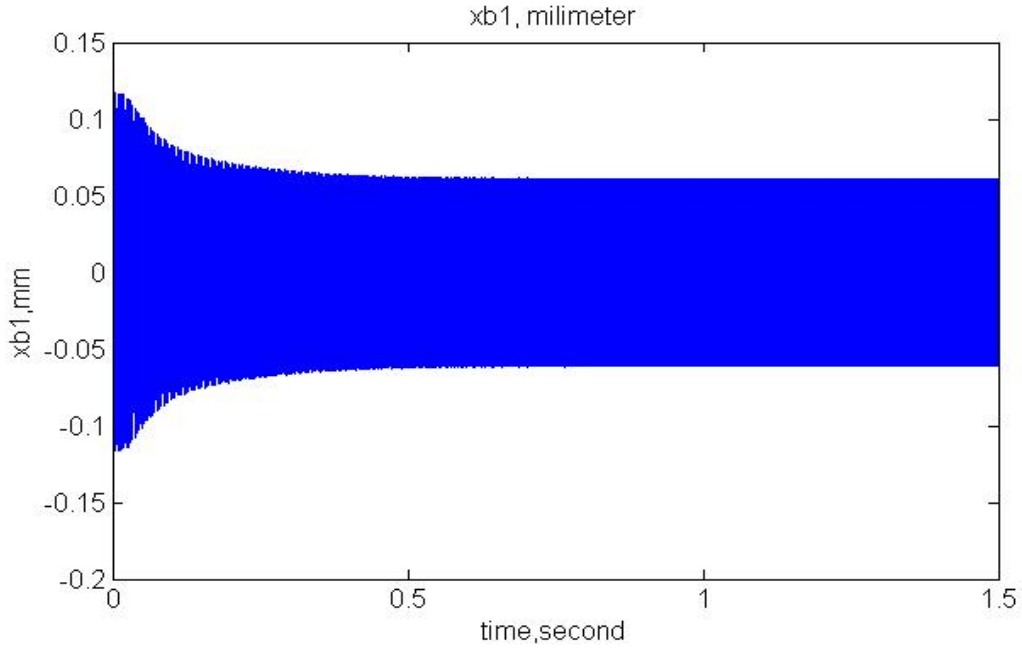

Fig. 5.12 Rotor displacement at bearing B in X-direction with $\alpha = 0.414$ and gyroscopic effect at 187,500rpm (controlled)

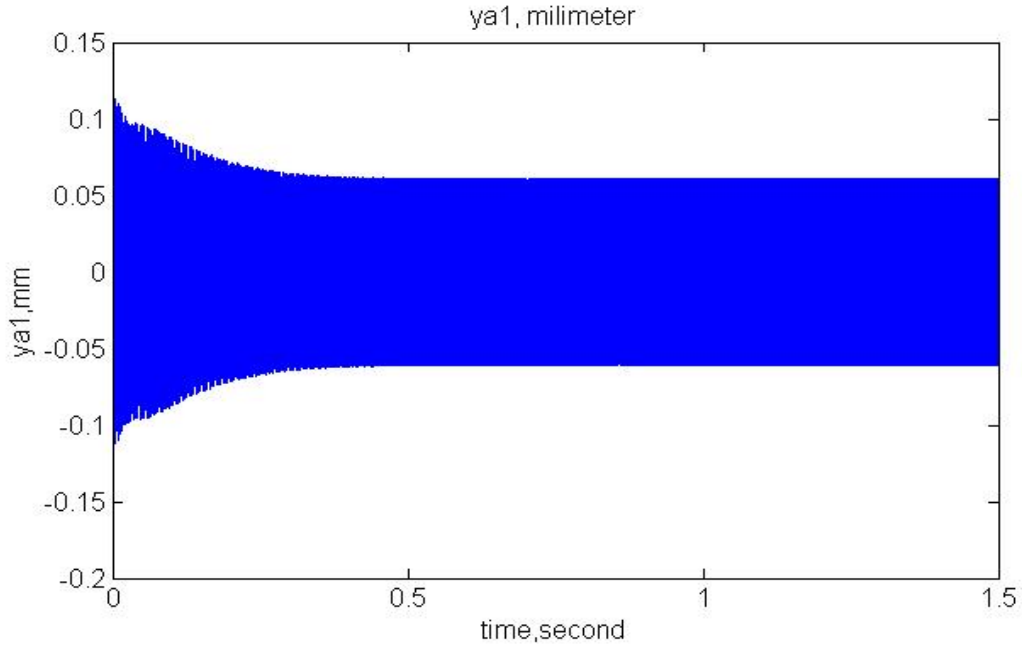

Fig. 5.13 Rotor displacement at bearing A in Y-direction with $\alpha = 0.414$ and gyroscopic effect at 187,500rpm (controlled)

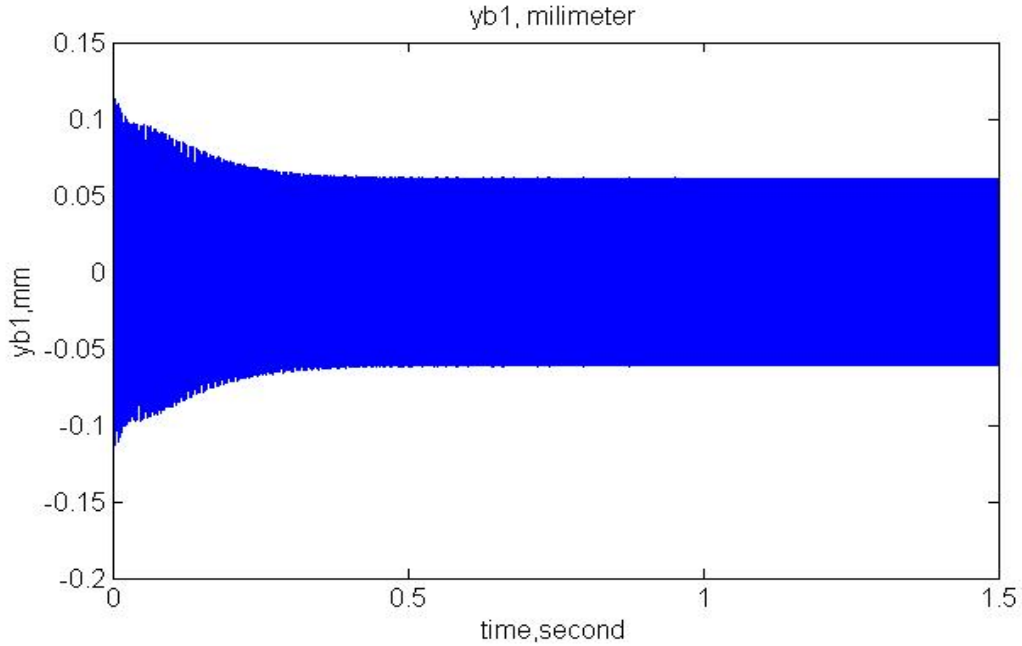

Fig. 5.14 Rotor displacement at bearing B in Y-direction with $\alpha = 0.414$ and gyroscopic effect at 187,500rpm (controlled)

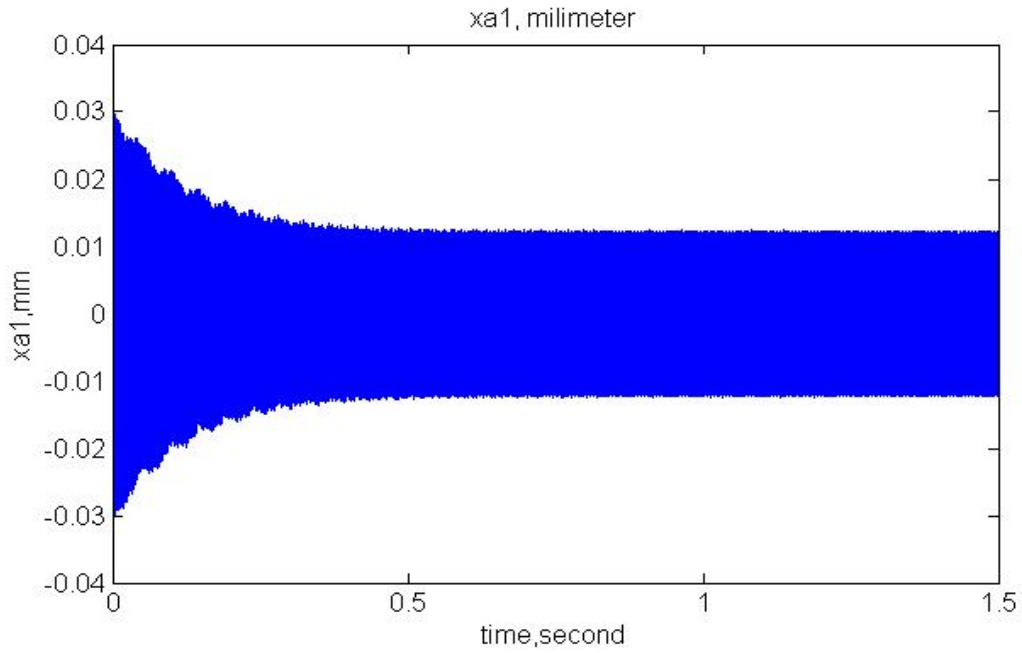

Fig. 5.15 Rotor displacement at bearing A in X-direction with $\alpha = 0.414$ and gyroscopic effect at 150,000rpm (controlled)

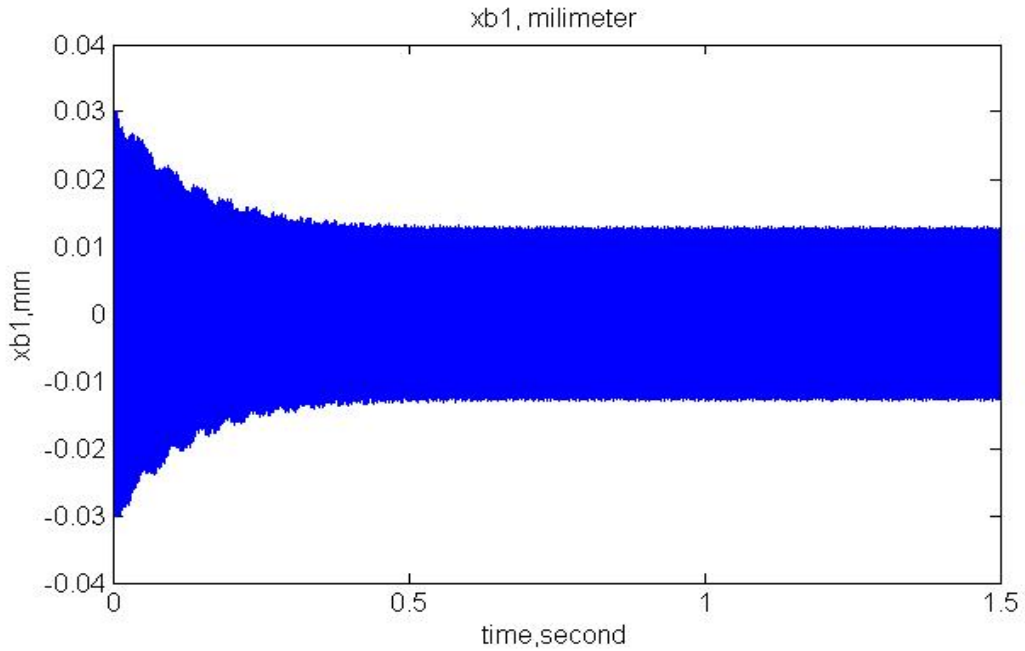

Fig. 5.16 Rotor displacement at bearing B in X-direction with $\alpha = 0.414$ and gyroscopic effect at 150,000rpm (controlled)

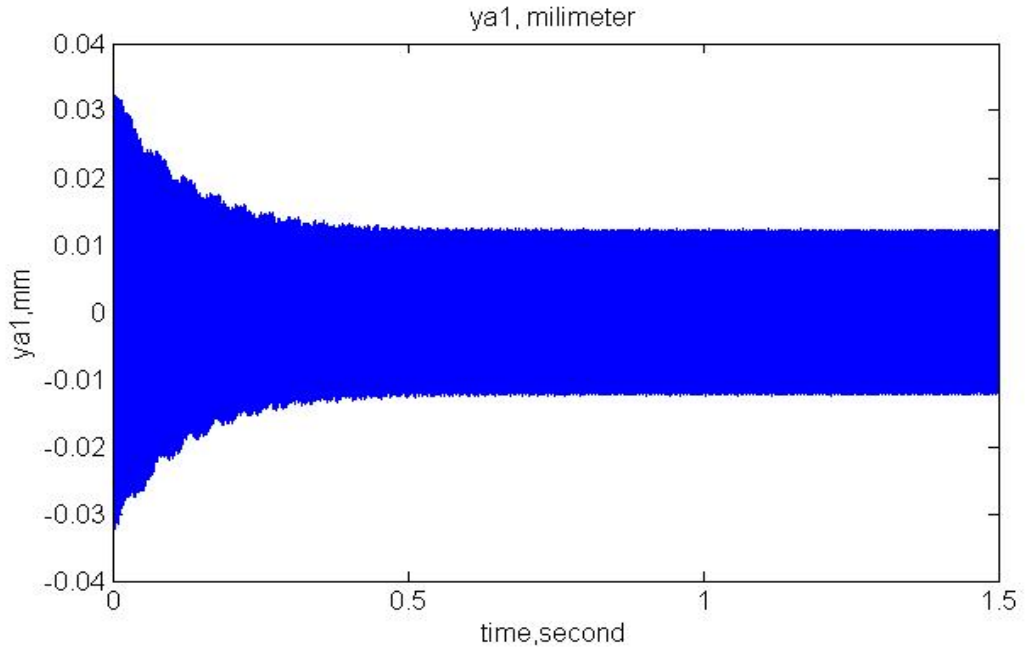

Fig. 5.17 Rotor displacement at bearing A in Y-direction with $\alpha = 0.414$ and gyroscopic effect at 150,000rpm (controlled)

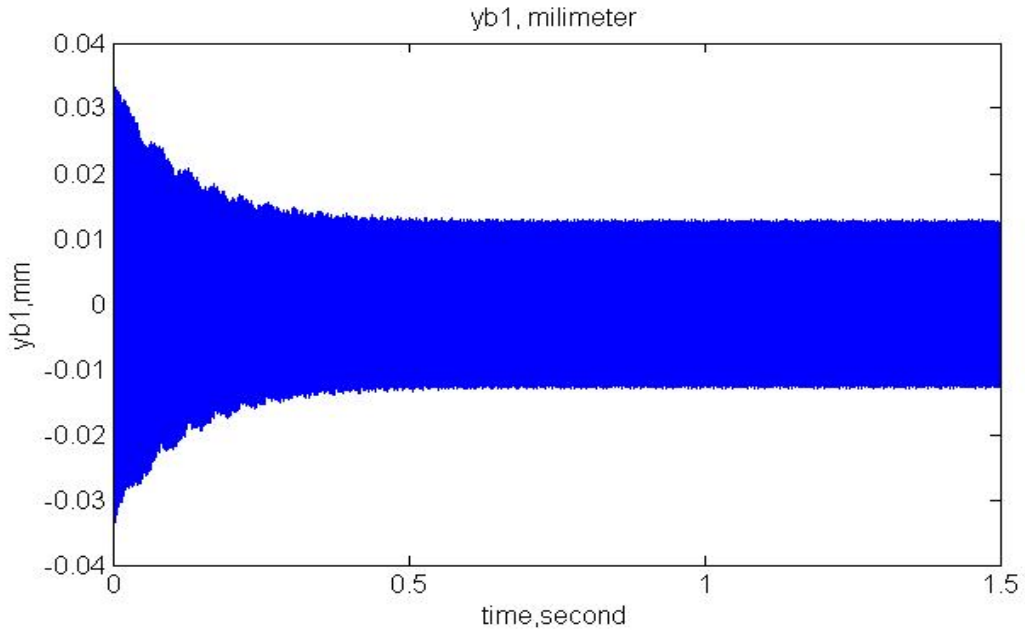

Fig. 5.18 Rotor displacement at bearing B in Y-direction with $\alpha = 0.414$ and gyroscopic effect at 150,000rpm (controlled)

Using the data provided in Figs. 5.11-5.18, the maximum and minimum displacements of the rotor at the 2 bearing locations in response to 150,000rpm and 187,500rpm are tabulated. Table 5.2 shows the vibration amplitudes in the negative direction and Table 5.3 gives those that are in the positive direction.

Table 5.2 Comparison of rotor displacement amplitude at 150,000rpm and 187,500rpm in negative direction

Speed (rpm) / Amplitude (mm)	150,000	187,500
Bearing A X-direction	0.03002	0.1166
Bearing B X-direction	0.03008	0.1164
Bearing A Y-direction	0.03311	0.1149
Bearing B Y-direction	0.03371	0.1168

Table 5.3 Comparison of rotor displacement amplitude at 150,000rpm and 187,500rpm in positive direction

Speed (rpm) / Amplitude (mm)	150,000	187,500
Bearing A X-direction	0.02761	0.1162
Bearing B X-direction	0.02727	0.1176
Bearing A Y-direction	0.02959	0.1167
Bearing B Y-direction	0.02983	0.1159

In Tables 5.2 and 5.3 one sees that the vibration displacements at 187,500rpm are at least 350% greater than their counterparts at 150,000rpm in either direction. The controller is seen to effectively keep the rotor displacements within the given 0.1375mm tight tolerance at both speeds. A second examination of the figures and tables show that after the initial 0.5 seconds, the time responses at 150,000rpm are bounded within ±0.01 mm. The corresponding time responses within the same time window at 187,500 rpm are between +0.06 and –0.06 mm. While the speed increases only by 20%, the controlled bound achieved by the controller is 600% greater. The impact of speed on the stability of the rotor and the functioning quality of the controller is therefore unmistakable.

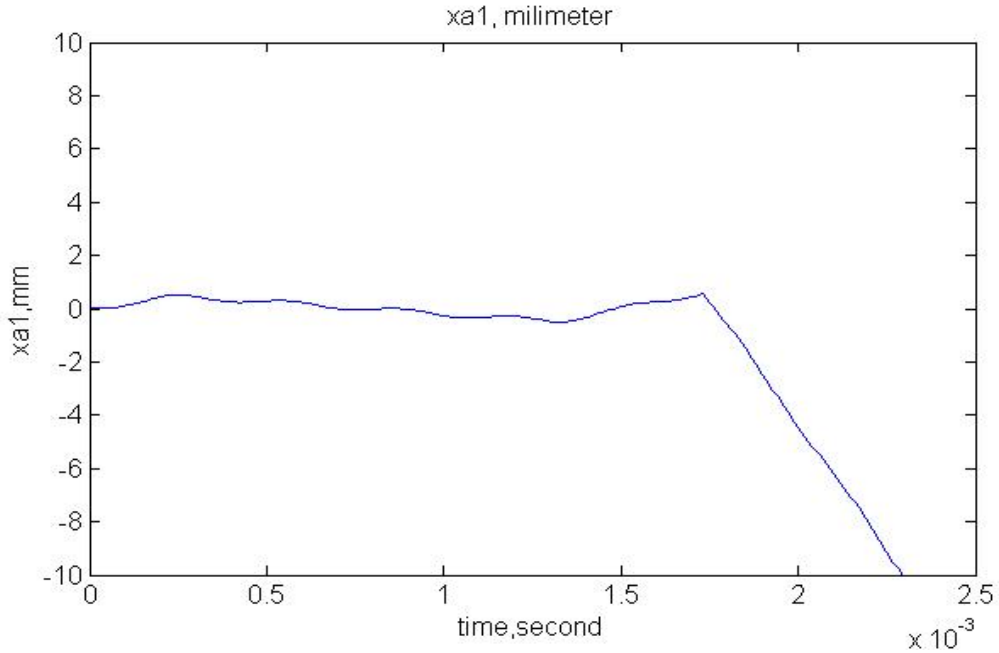

Fig. 5.19 Rotor displacement at bearing A in X-direction with $\alpha = 0.414$ and gyroscopic effect at 187,500rpm (uncontrolled)

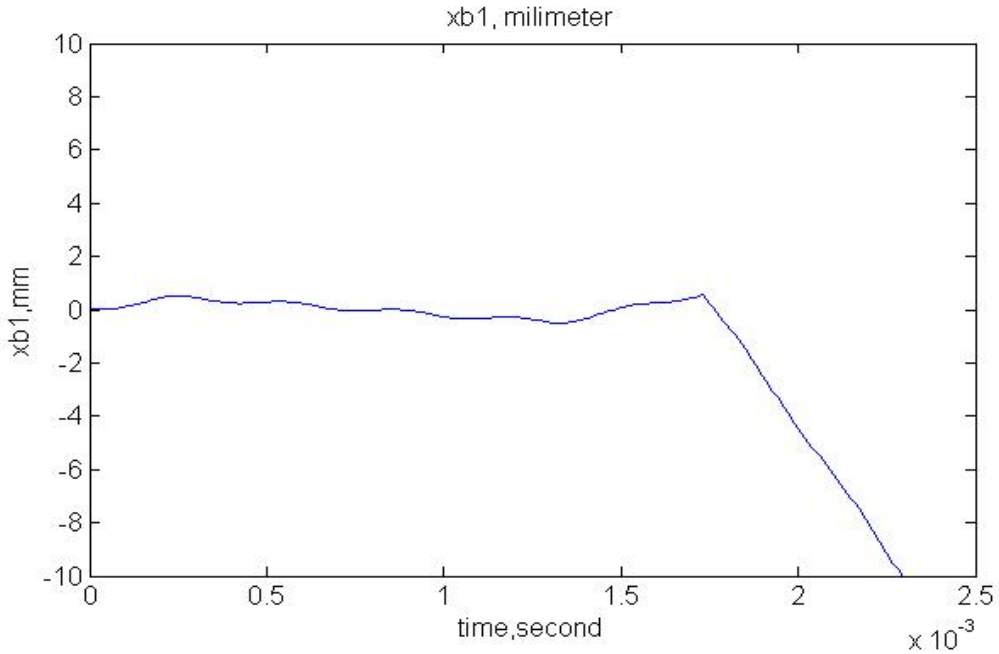

Fig. 5.20 Rotor displacement at bearing B in X-direction with $\alpha = 0.414$ and gyroscopic effect at 187,500rpm (uncontrolled)

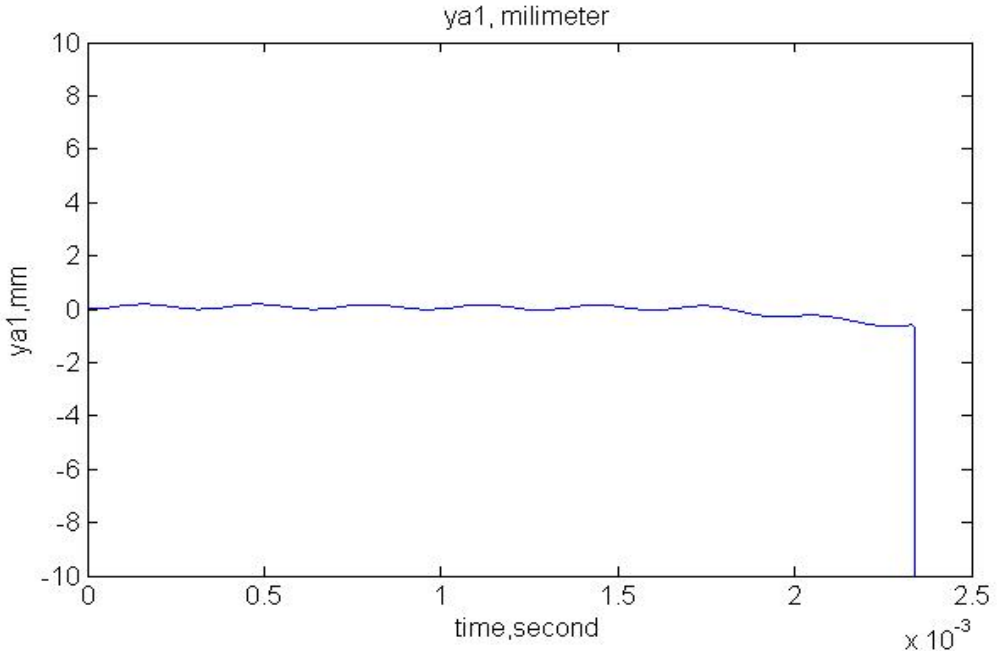

Fig. 5.21 Rotor displacement at bearing A in Y-direction with $\alpha = 0.414$ and gyroscopic effect at 187,500rpm (uncontrolled)

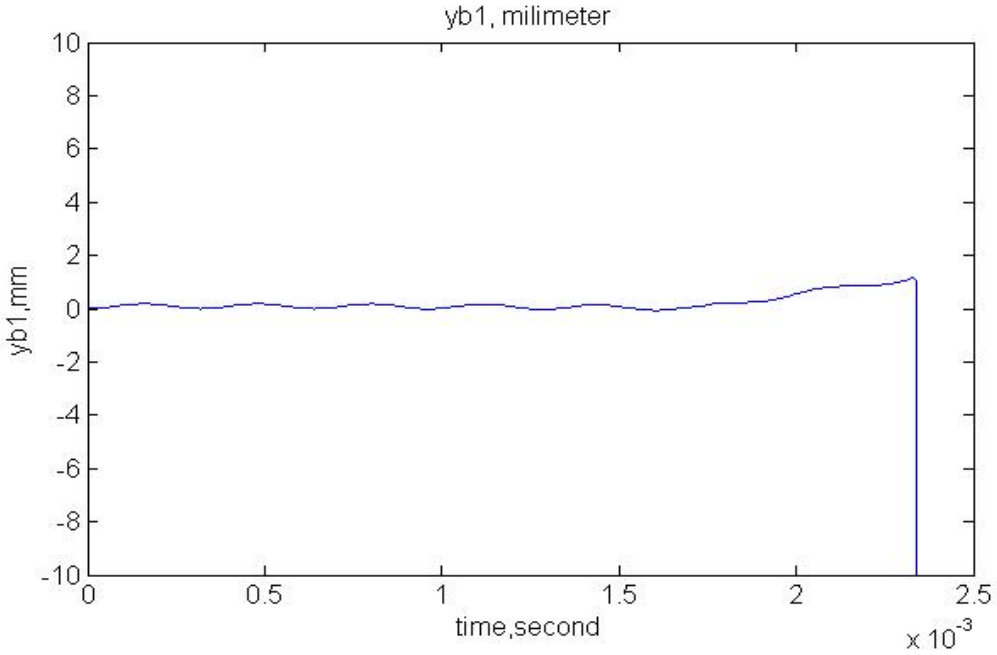

Fig. 5.22 Rotor displacement at bearing B in Y-direction with $\alpha = 0.414$ and gyroscopic effect at 187,500rpm (uncontrolled)

As is indicated by the crash lines in Figs. 5.19-5.22, the AMB-rotor system is extremely unstable at speed 187,500 rpm without the controller being brought on-line. The state of motion of the system rapidly deteriorates and the 0.55mm air gap is seen violated almost immediately at approximately 0.0012 seconds in Figs. 5.19 and 5.20. The various time responses of the AMB-rotor model system in Figs. 5.11-5.18 are all bounded under the maximum speed. However, it is difficult to tell from the bounded time responses as to the dynamic state of the system and whether the instability was properly mitigated and replaced with stability with the presence of the controller.

A phase portrait is the geometric representation of the trajectory of a dynamic system in the state space. The periodic or otherwise aperiodic motion of the system can be visually established by studying the geometric characteristics and flow path of the trajectory. Figs 5.23-5.26 are the phase portraits of the rotor motion corresponding to the first 1.5 seconds upon system start-up. They all present symmetrical, well-defined geometries understood as limit-cycles that necessarily suggest a stable state of quasi-periodic motion. In other words, while the controlled system responses are periodic, nevertheless, they are also not chaotic.

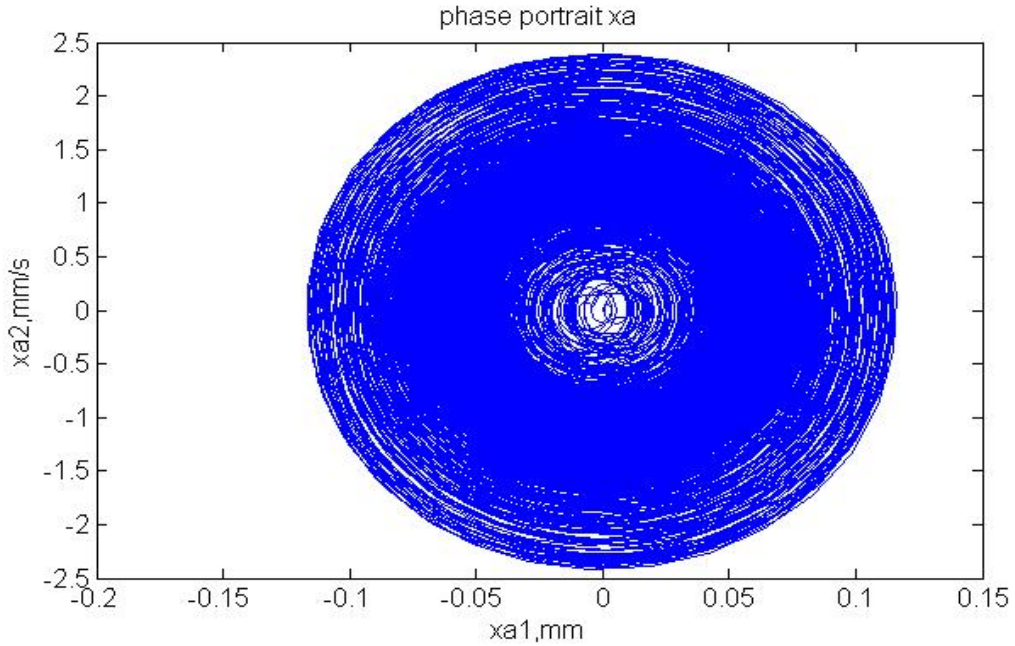

Fig. 5.23 Phase portrait of rotor motion at bearing A in X-direction with $\alpha = 0.414$ and gyroscopic effect at 187,500rpm

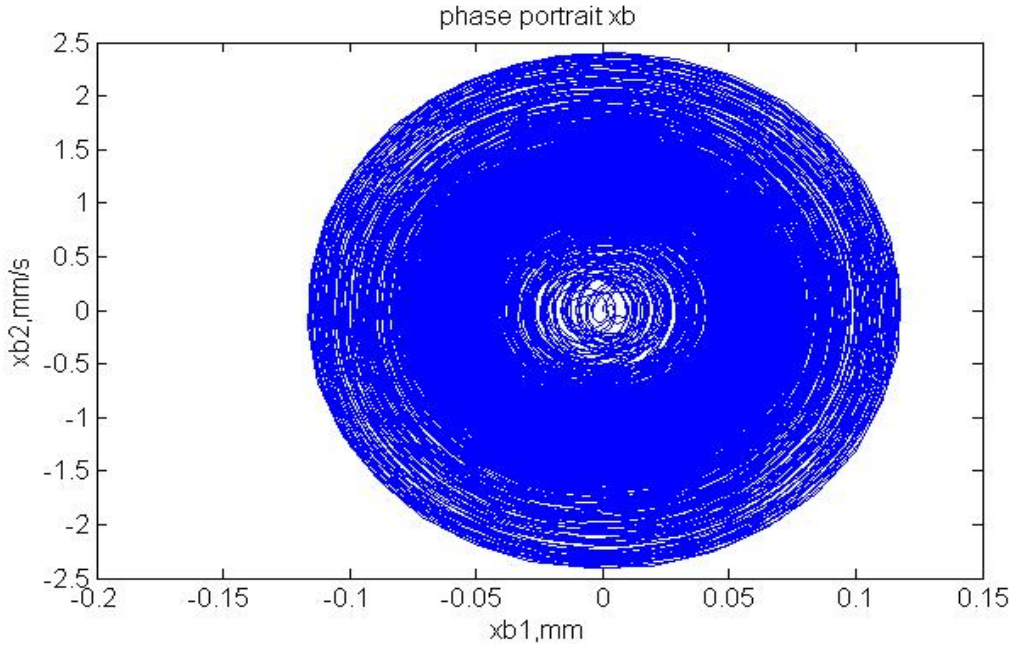

Fig. 5.24 Phase portrait of rotor motion at bearing B in X-direction with $\alpha = 0.414$ and gyroscopic effect at 187,500rpm

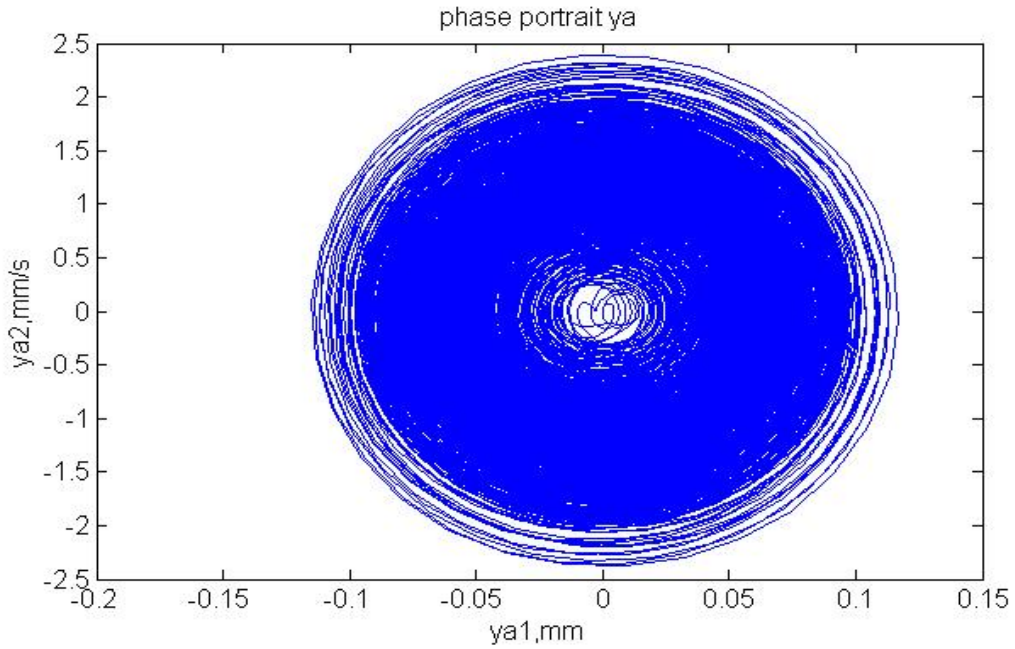

Fig. 5.25 Phase portrait of rotor motion at bearing A in Y-direction with $\alpha = 0.414$ and gyroscopic effect at 187,500rpm

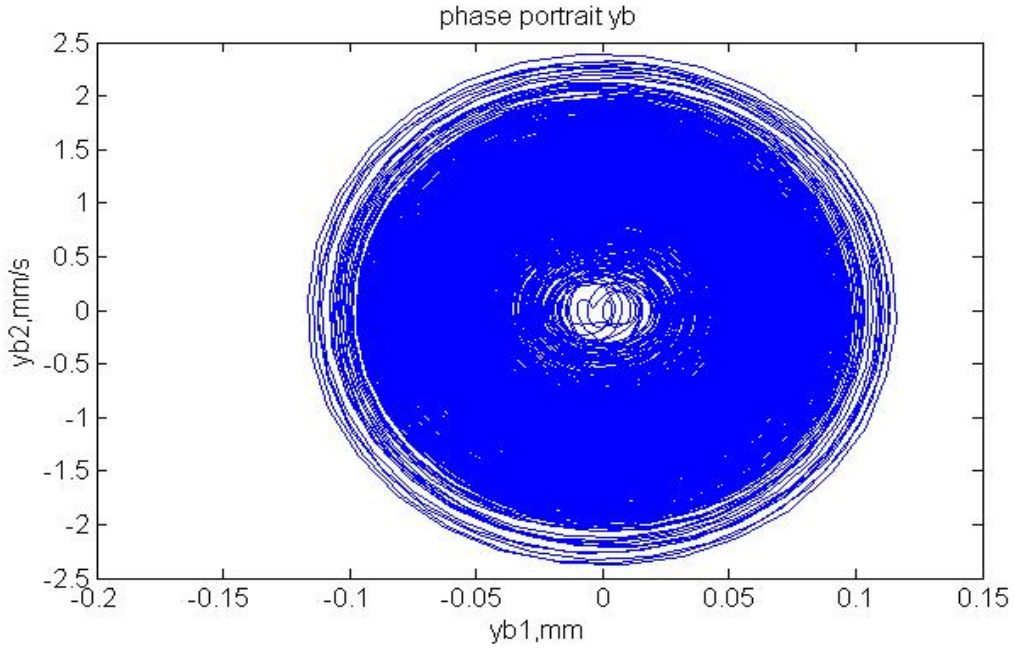

Fig. 5.26 Phase portrait of rotor motion at bearing B in Y-direction with $\alpha = 0.414$ and gyroscopic effect at 187,500rpm

As oppose to the controlled responses whose state space variables follow a trajectory that evolves into a limit-cycle, as depicted in the phase portraits in Figs. 5.27-5.30, the system responses without the controller exerting control to mitigate instability are anything but a limit-cycle.

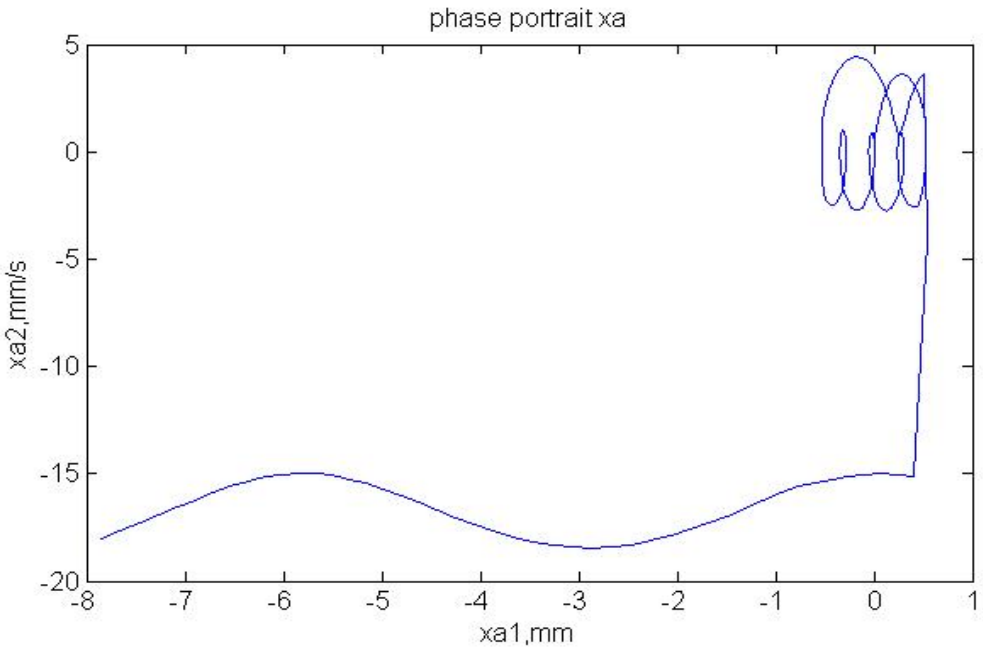

Fig. 5.27 Phase portrait of rotor motion at bearing A in X-direction with $\alpha = 0.414$ and gyroscopic effect at 187,500rpm (uncontrolled)

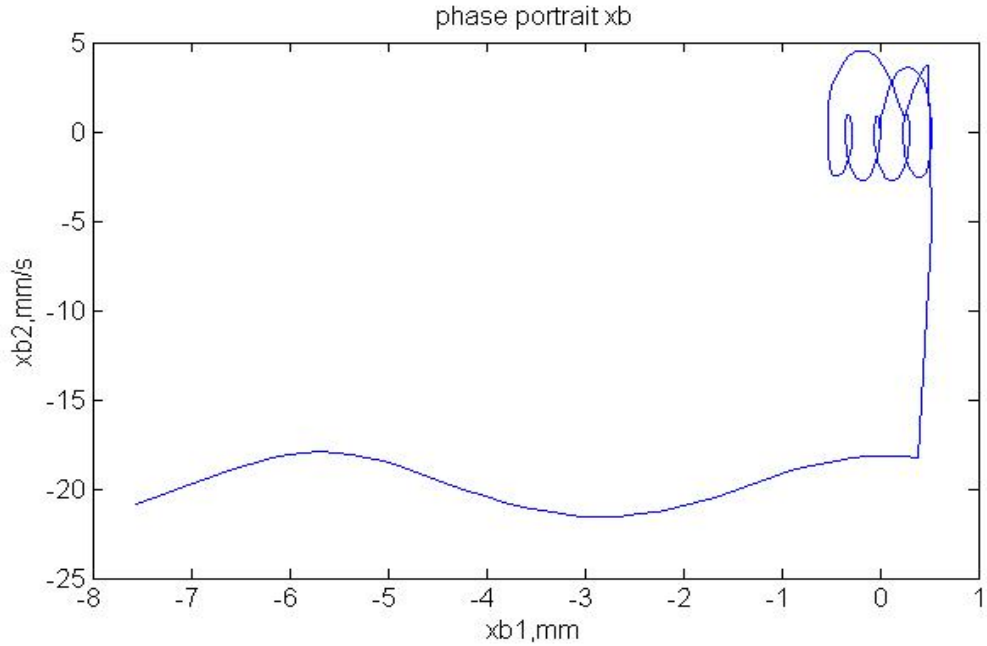

Fig. 5.28 Phase portrait of rotor motion at bearing B in X-direction with $\alpha = 0.414$ and gyroscopic effect at 187,500rpm (uncontrolled)

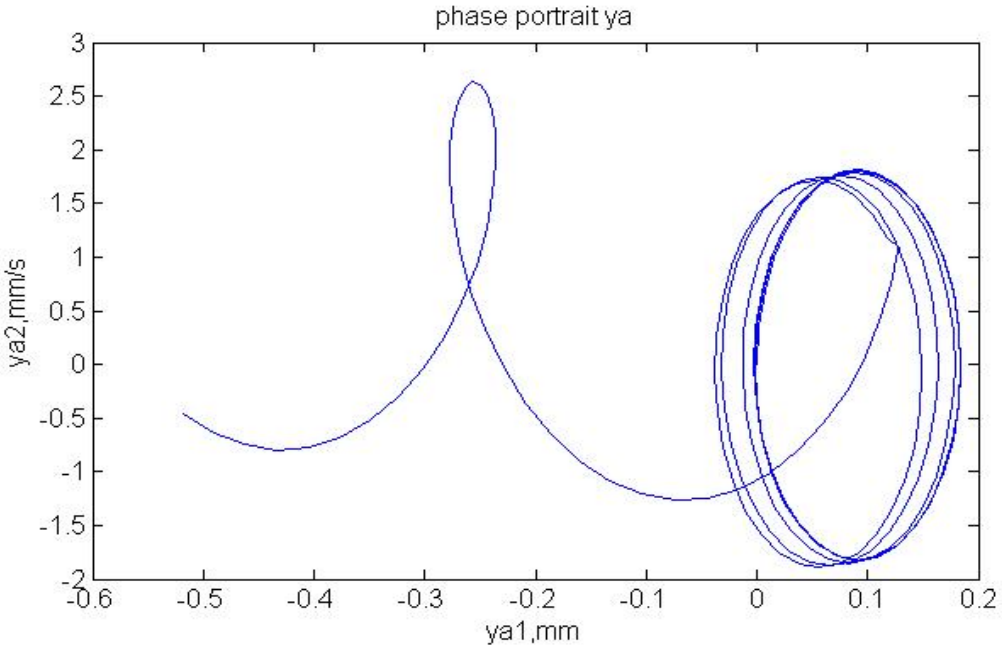

Fig. 5.29 Phase portrait of rotor motion at bearing A in Y-direction with $\alpha = 0.414$ and gyroscopic effect at 187,500rpm (uncontrolled)

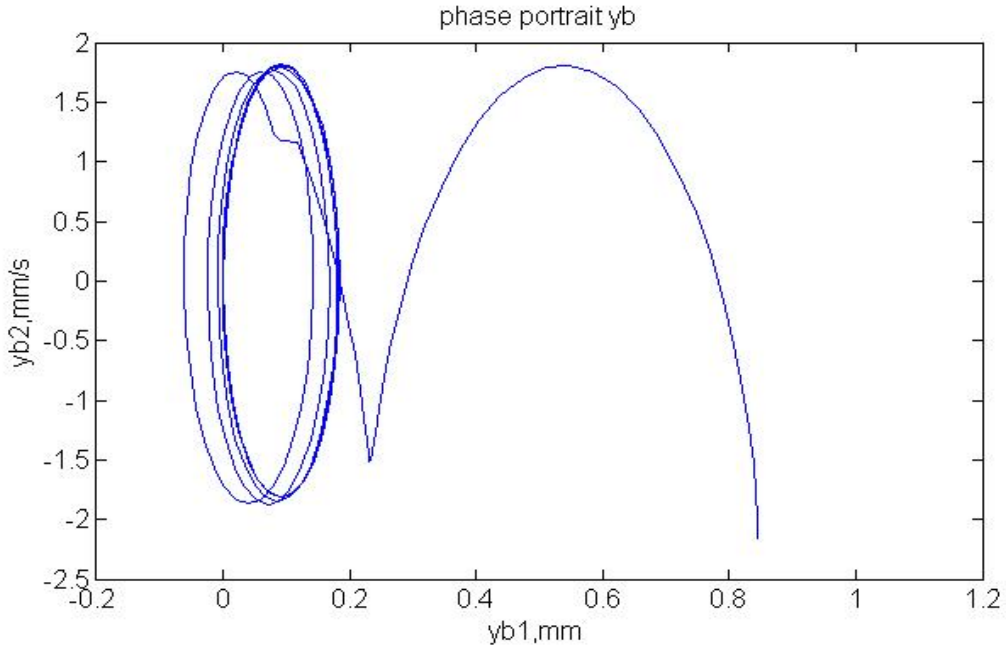

Fig. 5.30 Phase portrait of rotor motion at bearing B in Y-direction with $\alpha = 0.414$ and gyroscopic effect at 187,500rpm (uncontrolled)

It is seen in Figs. 5.11-5.18 that the system responses are all bounded between 0.5 seconds and 1.5 seconds subject to the action of the controller. The phase portraits correspond to this time window are displayed in Figs. 5.31-5.34 below. It is understood that these figures are reproductions of Figs. 5.23-5.26 by removing the portion of each of the trajectory that corresponds to the initial 0.5 seconds of the time response. That the system responses are symmetrically bounded and quasi-periodically stable is evident from the figures.

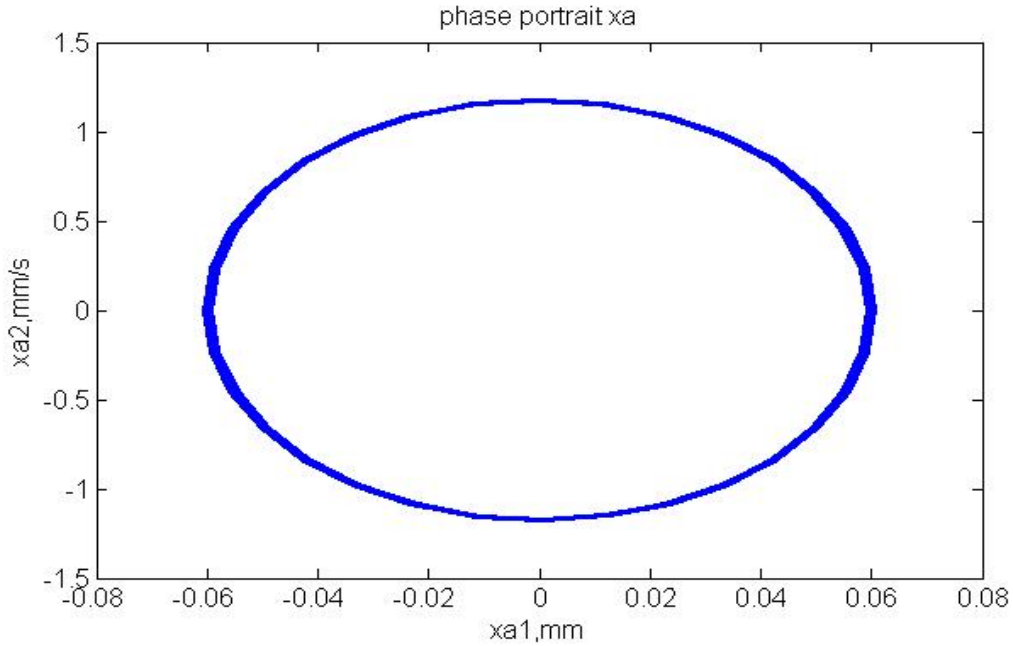

Fig. 5.31 Phase portrait of rotor motion at bearing A in X-direction with $\alpha = 0.414$ and gyroscopic effect at 187,500rpm (after 0.5 seconds)

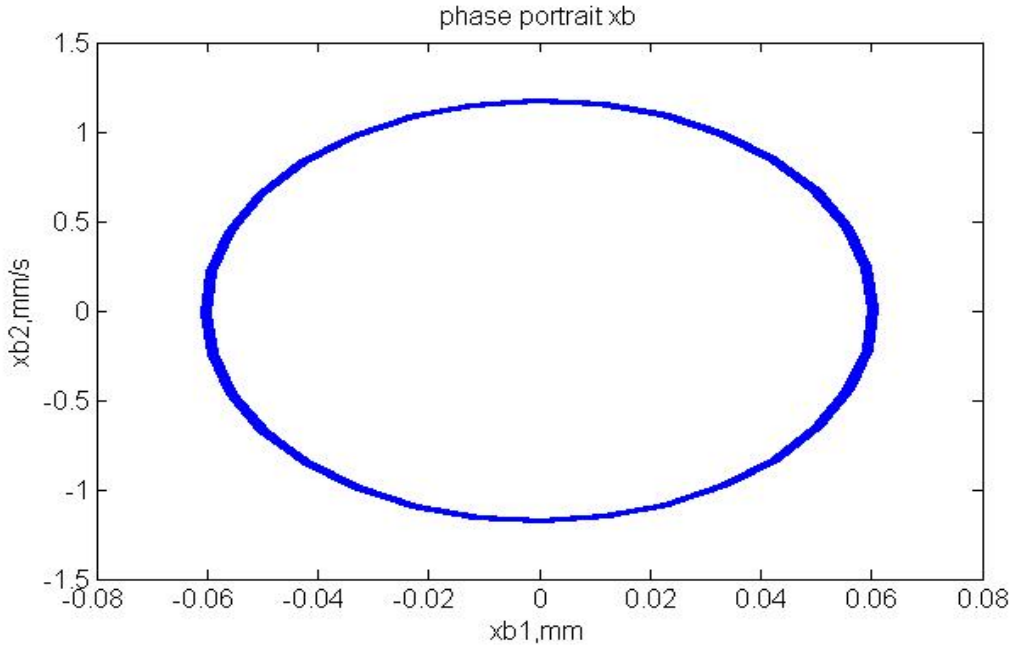

Fig. 5.32 Phase portrait of rotor motion at bearing B in X-direction with $\alpha = 0.414$ and gyroscopic effect at 187,500rpm (after 0.5 seconds)

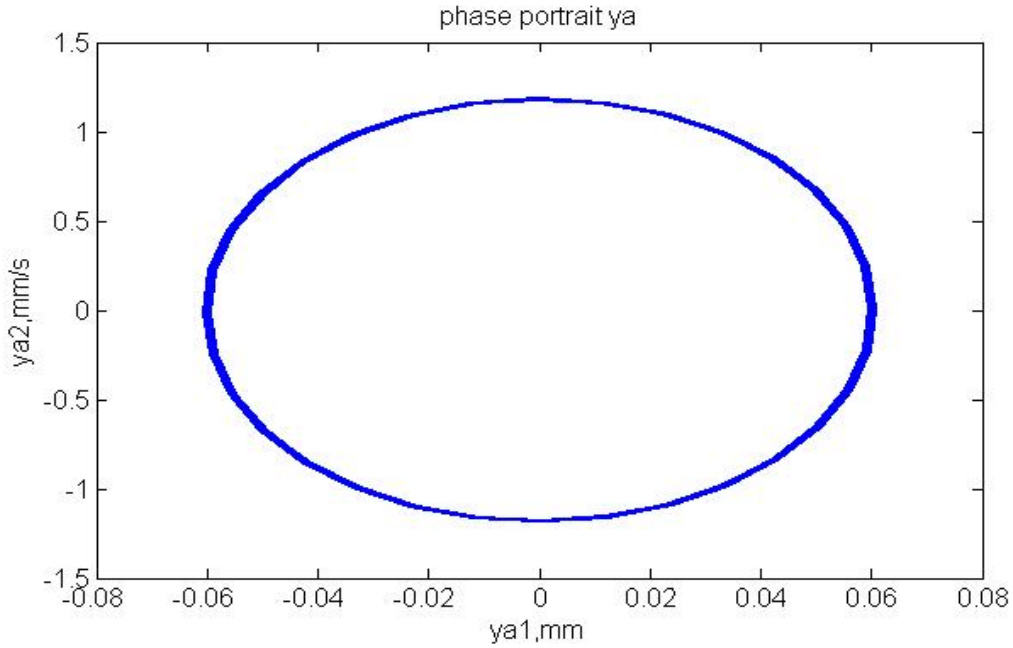

Fig. 5.33 Phase portrait of rotor motion at bearing A in Y-direction with $\alpha = 0.414$ and gyroscopic effect at 187,500rpm (after 0.5 seconds)

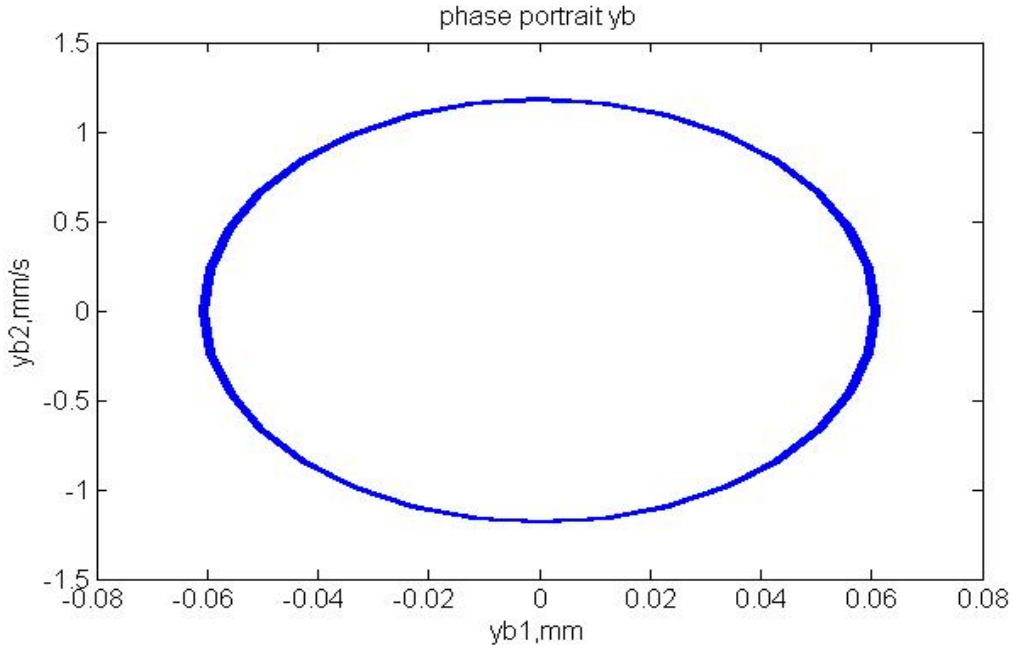

Fig. 5.34 Phase portrait of rotor motion at bearing B in Y-direction with $\alpha = 0.414$ and gyroscopic effect at 187,500rpm (after 0.5 seconds)

Fractals are sets that have fine details at all possible scales and the quality of self-similarity at different scales. However, fractals are hard to discern in the state space described by using phase portraits. Poincare sections are generally considered a better alternative to phase portraits for revealing fractal structures in the state space. In the followings, Poincare sections are generated by sampling the state space trajectory using the reciprocal of the driving frequency of the rotor. Given the maximum rotor speed at 187,500rpm, the sampling period is therefore 0.00032 seconds. The Poincare sections shown in Figs. 5.35 - 5.39 all demonstrate distinctive, well-defined fractal structures that are spiral-like. Such clearly delineated fractals suggest that the controlled system is deterministic and that the controlled response is predictable. A meticulous examination of Fig. 5.35 reveals that the trajectory spirals toward the center of the section. This is demonstrated in Fig. 5.39 where 4 sets of 80 consecutive points are plotted sequentially to show the time evolution of the trajectory following the order of black-red-blue-yellow. It can be seen that the flow starts from the outer perimeter and progresses toward the center. Similar observations can also be made with Figs. 5.36-5.38.

As is evident in Figs. 5.40-5.43 where the Poincare sections plotted therein correspond to the trajectories collected between the 1-to-1.5 seconds window that all spirals evolve into yet another well-defined fractal structure, with the two sections in Figs. 5.40 and 5.41 looking like a ciabatta bun and the two sections in Figs. 5.42 and 5.43 like a crushed ring.

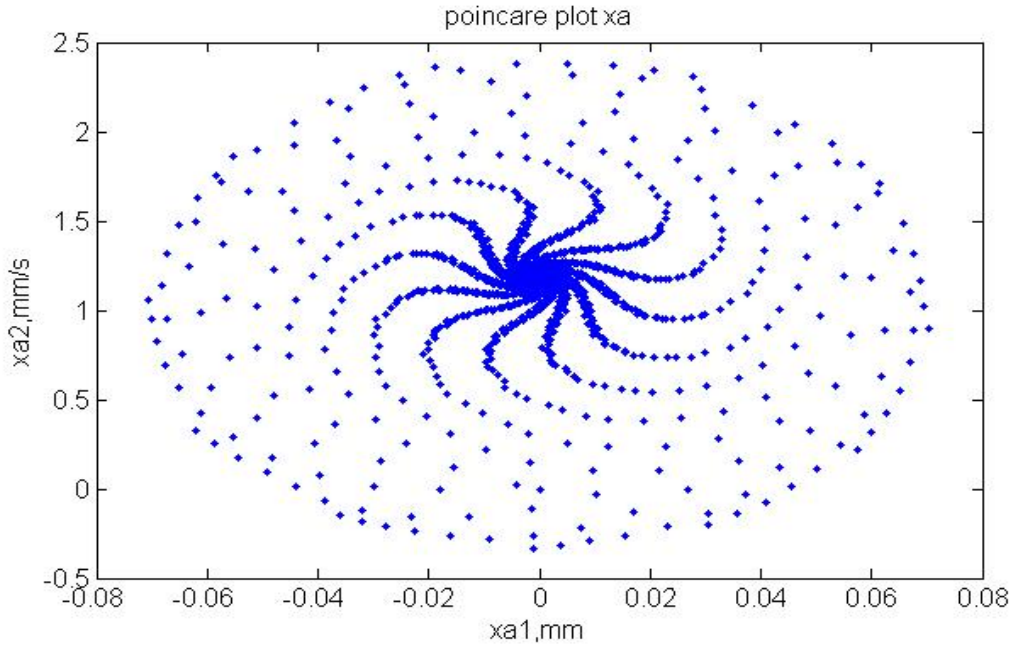

Fig. 5.35 Poincare section of rotor motion at bearing A in X-direction with $\alpha = 0.414$ and gyroscopic effect at 187,500rpm

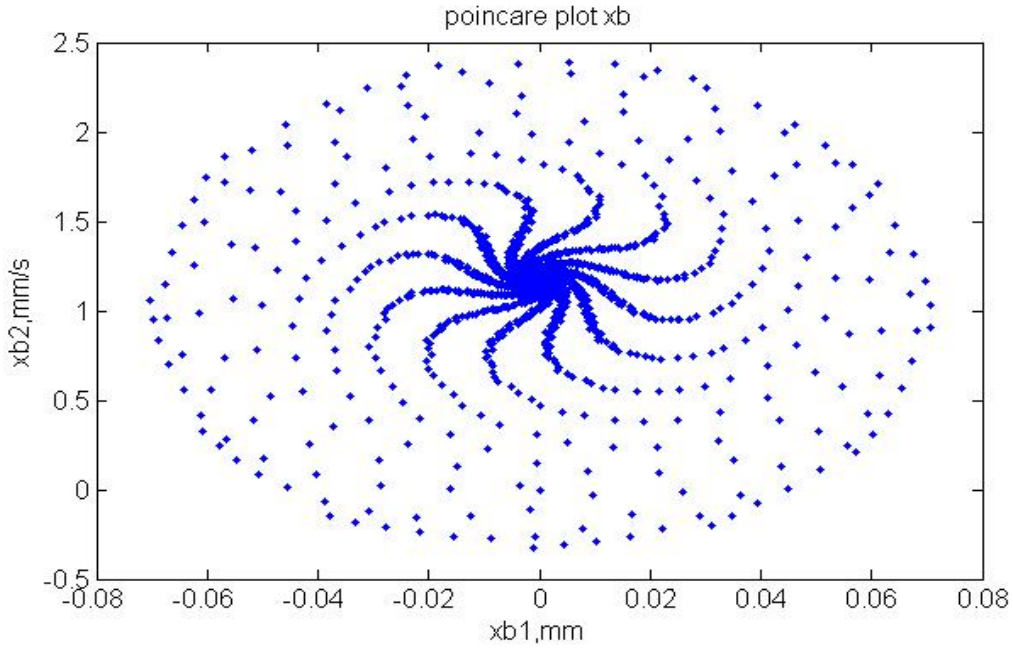

Fig. 5.36 Poincare section of rotor motion at bearing B in X-direction with $\alpha = 0.414$ and gyroscopic effect at 187,500rpm

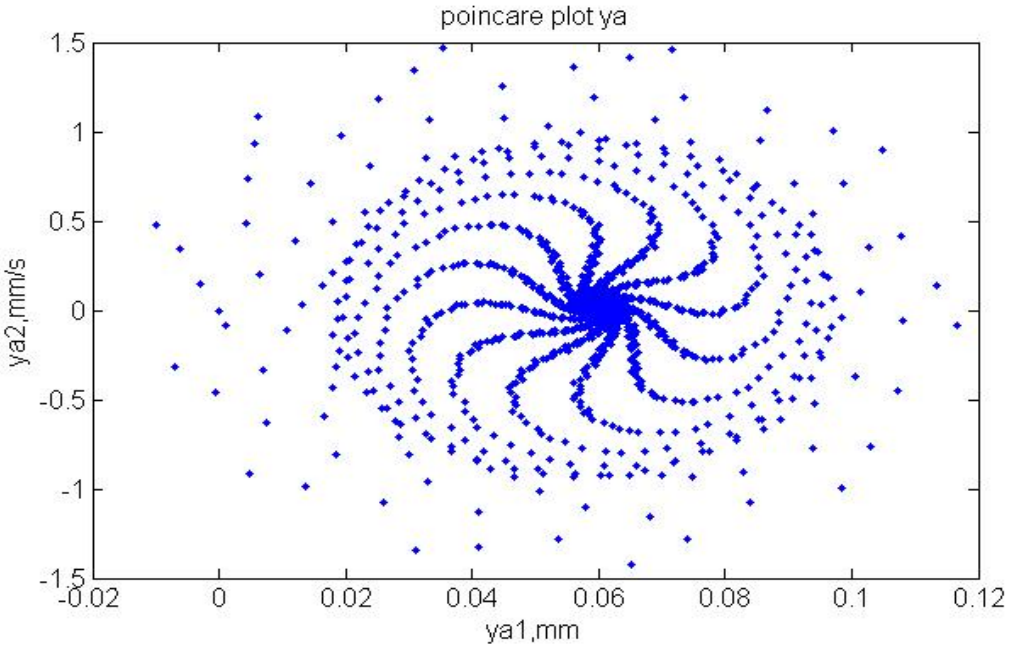

Fig. 5.37 Poincare section of rotor motion at bearing A in Y-direction with $\alpha = 0.414$ and gyroscopic effect at 187,500rpm

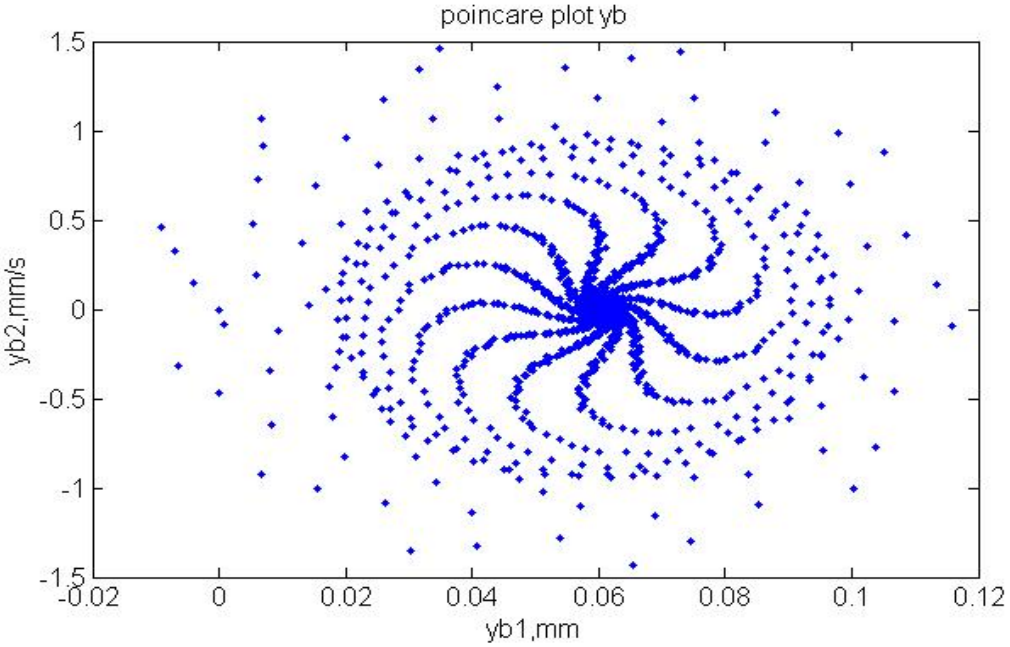

Fig. 5.38 Poincare plot of rotor motion at bearing B in Y-direction with $\alpha = 0.414$ and gyroscopic effect at 187,500rpm

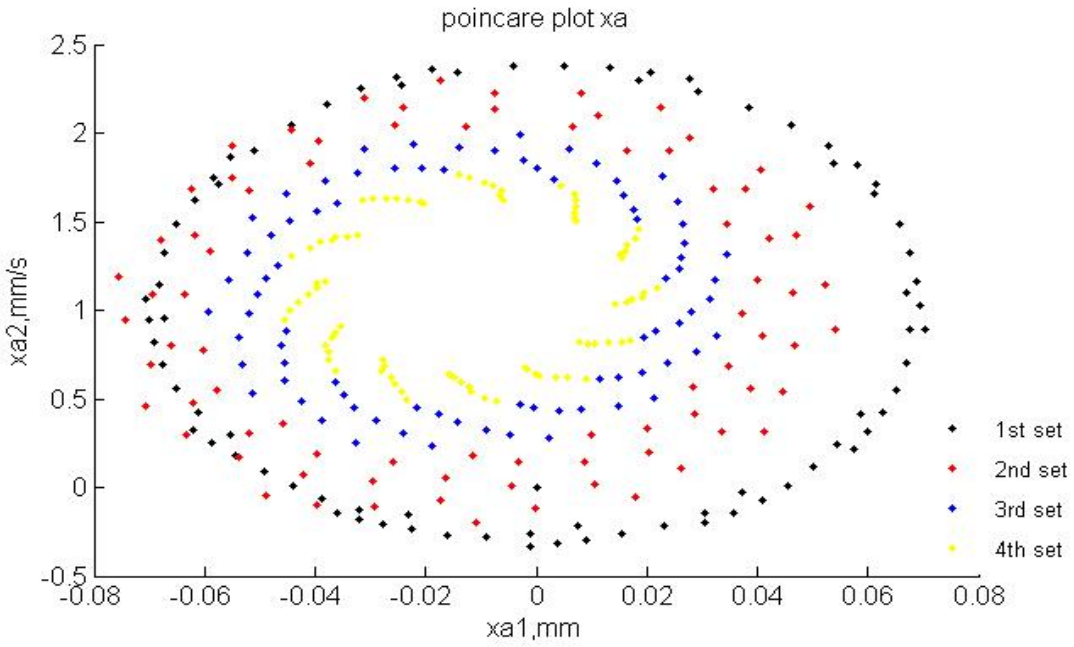

Fig. 5.39 Evolution of Poincare section

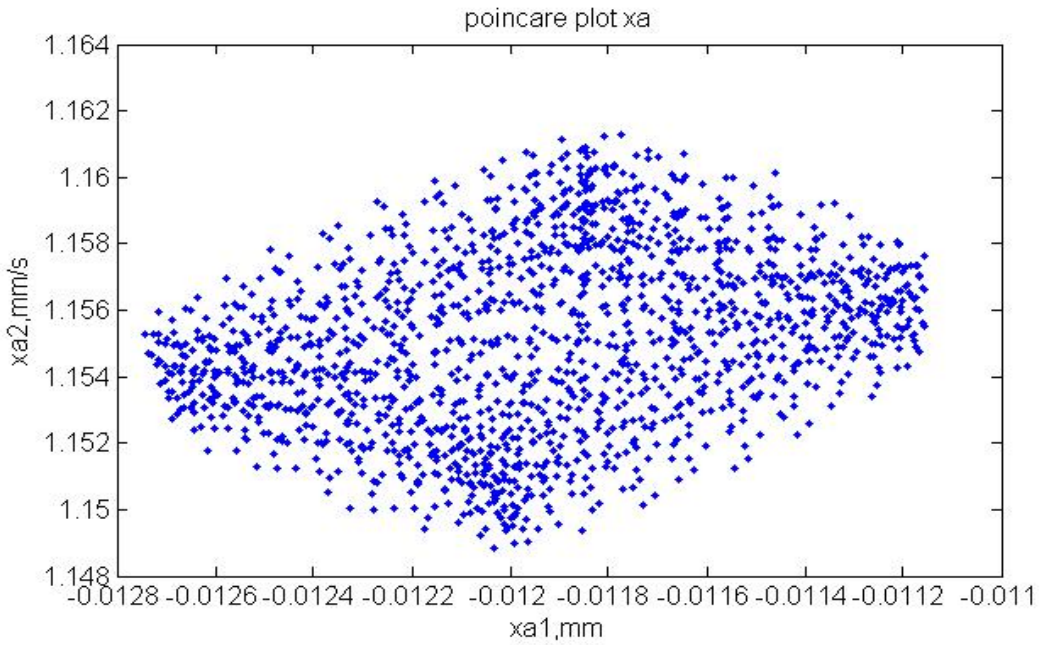

Fig. 5.40 Poincare plot of rotor motion at bearing A in X-direction with $\alpha = 0.414$ and gyroscopic effect at 187,500rpm (after 1 seconds)

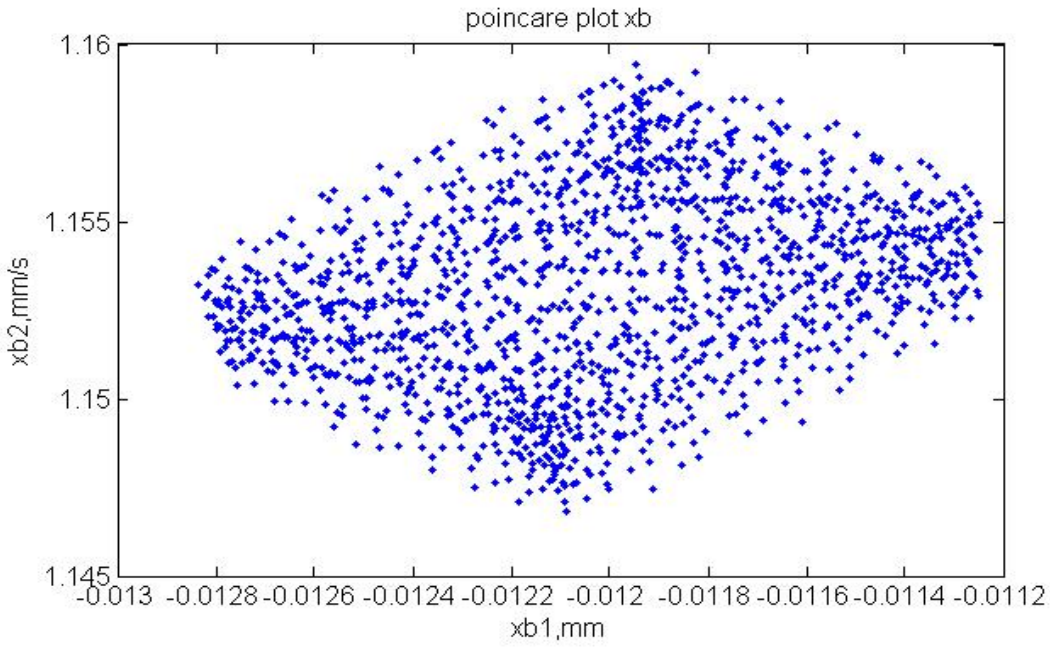

Fig. 5.41 Poincare plot of rotor motion at bearing B in X-direction with $\alpha = 0.414$ and gyroscopic effect at 187,500rpm (after 1 seconds)

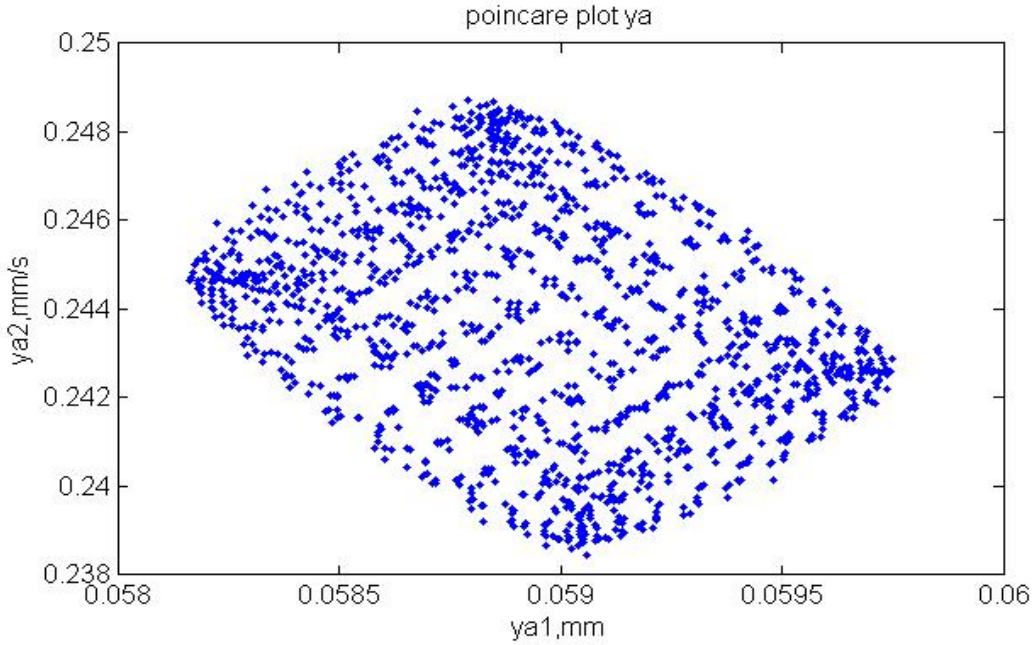

Fig. 5.42 Poincare plot of rotor motion at bearing A in Y-direction with $\alpha = 0.414$ and gyroscopic effect at 187,500rpm (after 1 seconds)

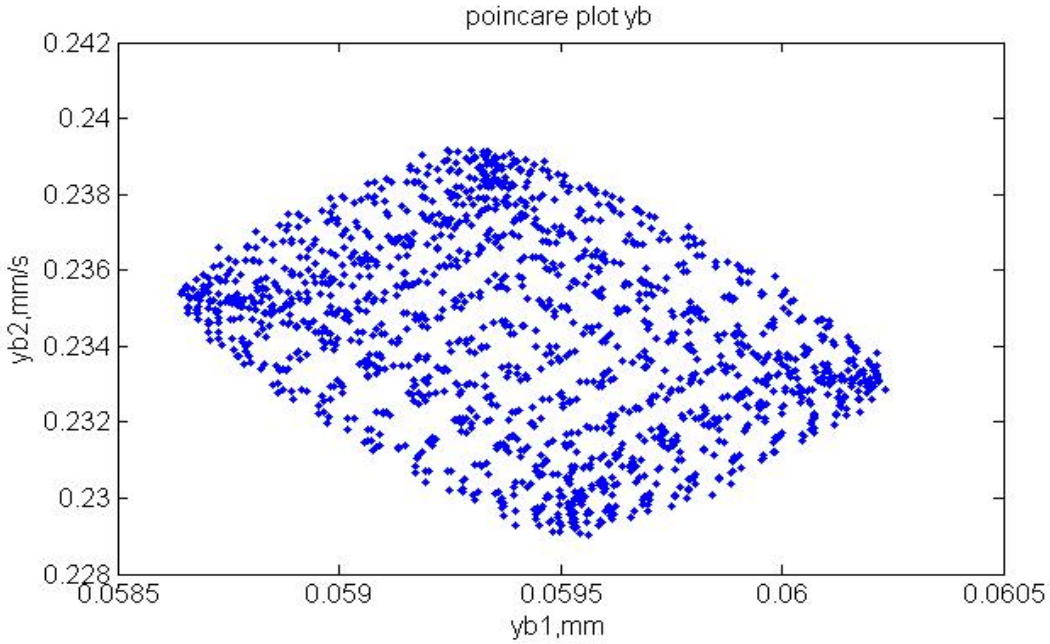

Fig. 5.43 Poincare plot of rotor motion at bearing B in Y-direction with $\alpha = 0.414$ and gyroscopic effect at 187,500rpm (after 1 seconds)

To further demonstrate the performance of the controller design, the controlled responses found in Figs. 5.11-5.14 are transformed into the joint time-frequency domain using the Hilbert-Hung Transform (HHT). Unlike Fourier-based transformation methods, the HHT does not use a set of predetermined basis functions. But rather it uses the Empirical Mode Decomposition (EMD) scheme to extract from the signal itself a set of orthogonal, mono-components called Intrinsic Mode functions (IMFs). IMFs are then processed by Hilbert transform to determine the instantaneous frequency of each of the extracted component. The notion of instantaneous frequency has been found feasible for the accurate estimation of system characteristics and nonlinearities [25]. It is seen in Figs. 5.44-5.47 that, with the online nonlinear time-frequency control, the bandwidths of all the non-stationary spectra are restrained and all the time-varying high frequency components

indicative of strong bifurcated states of nonlinearity are all properly mitigated well before the 0.5 seconds time mark. These observations necessarily testify to the fact that the highly nonlinear AMB-rotor system is under the control of the controller at the extreme speed of 187,500rpm in both the time and frequency domains.

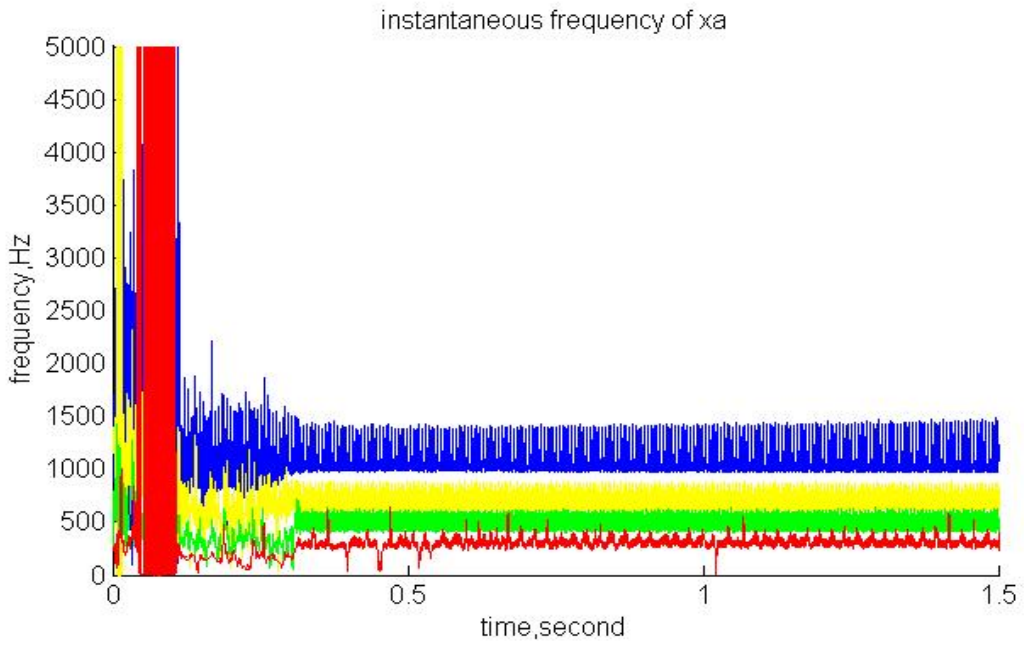

Fig. 5.44 Instantaneous frequency of rotor motion at bearing A in X-direction with $\alpha = 0.414$ and gyroscopic effect at 187,500rpm

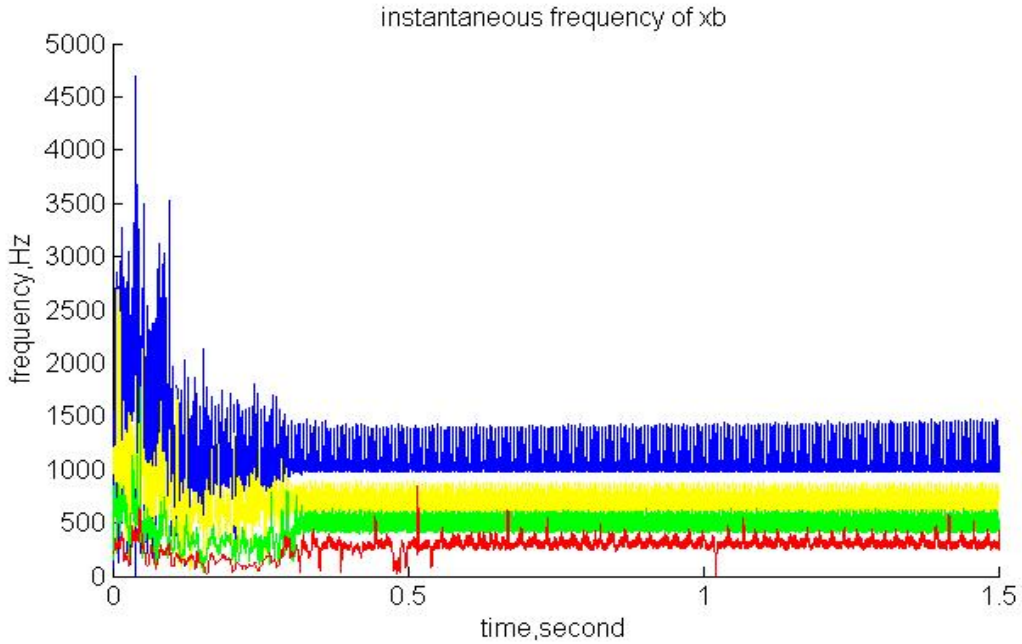

Fig. 5.45 Instantaneous frequency of rotor motion at bearing B in X-direction with $\alpha = 0.414$ and gyroscopic effect at 187,500rpm

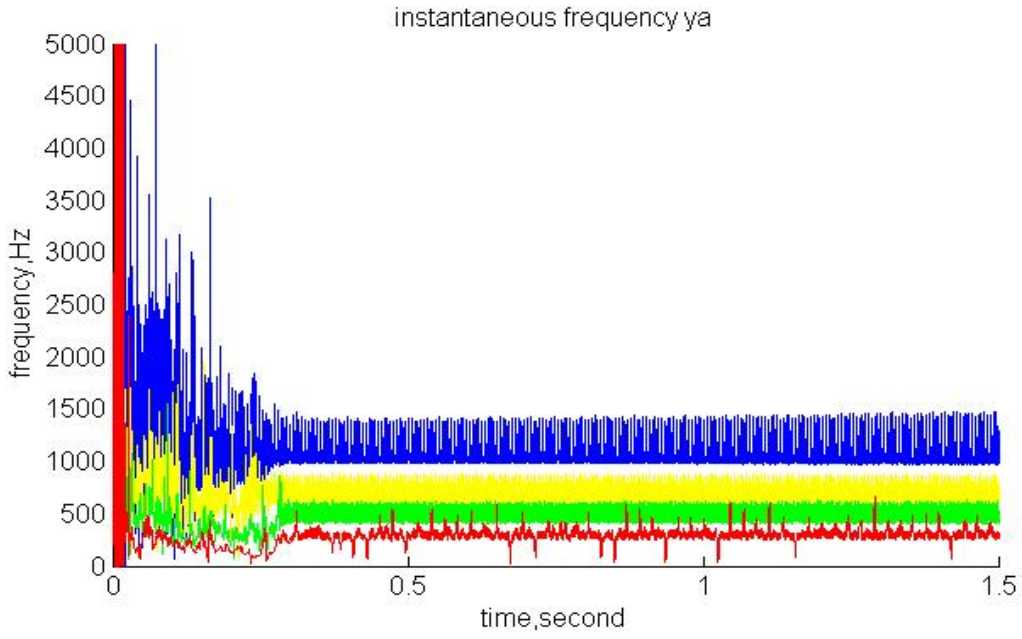

Fig. 5.46 Instantaneous frequency of rotor motion at bearing A in Y-direction with $\alpha = 0.414$ and gyroscopic effect at 187,500rpm

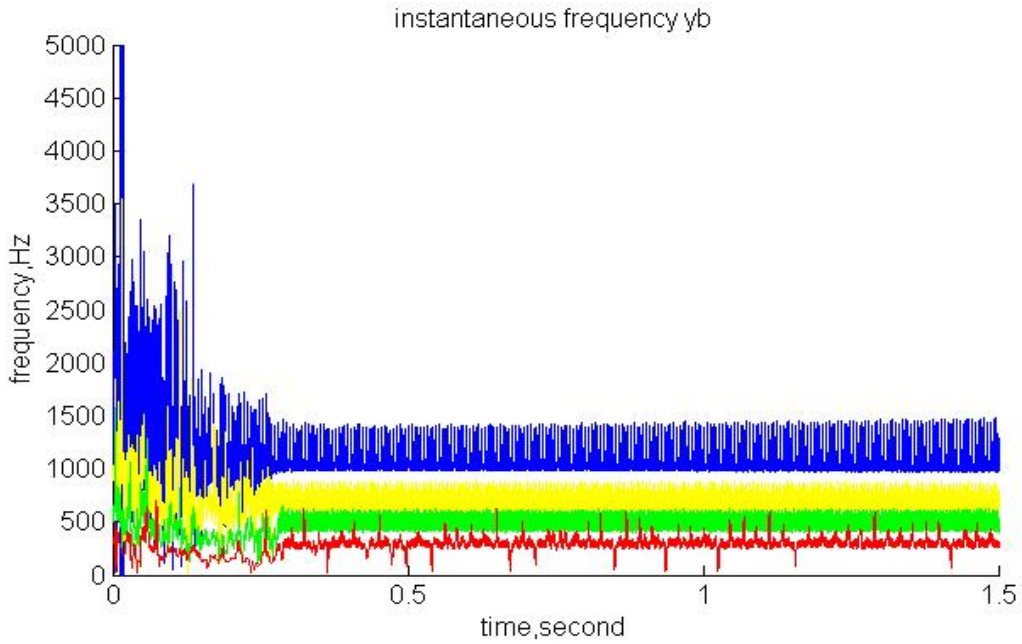

Fig. 5.47 Instantaneous frequency of rotor motion at bearing B in Y-direction with $\alpha = 0.414$ and gyroscopic effect at 187,500rpm

5.4 Robustness of Controller Design

In the preceding section the performance of the controller in properly controlling the AMB-rotor system at extreme speeds was evaluated without considering external excitation or perturbation. However, external excitation is inevitable in real-world applications. Of all the unexpected, potentially harmful external input, impulse of short duration (and thus of broad spectrum) is of great concern for high-speed rotor-dynamic systems. External excitations that are spectrally broad bandwidth are particularly detrimental to the AMB-rotor system. They are most potent in compromising the control quality. In the present section, an impulse of 5,000m/s^2 in magnitude and 0.001seconds in duration is applied to the rotor at 187,500rpm.

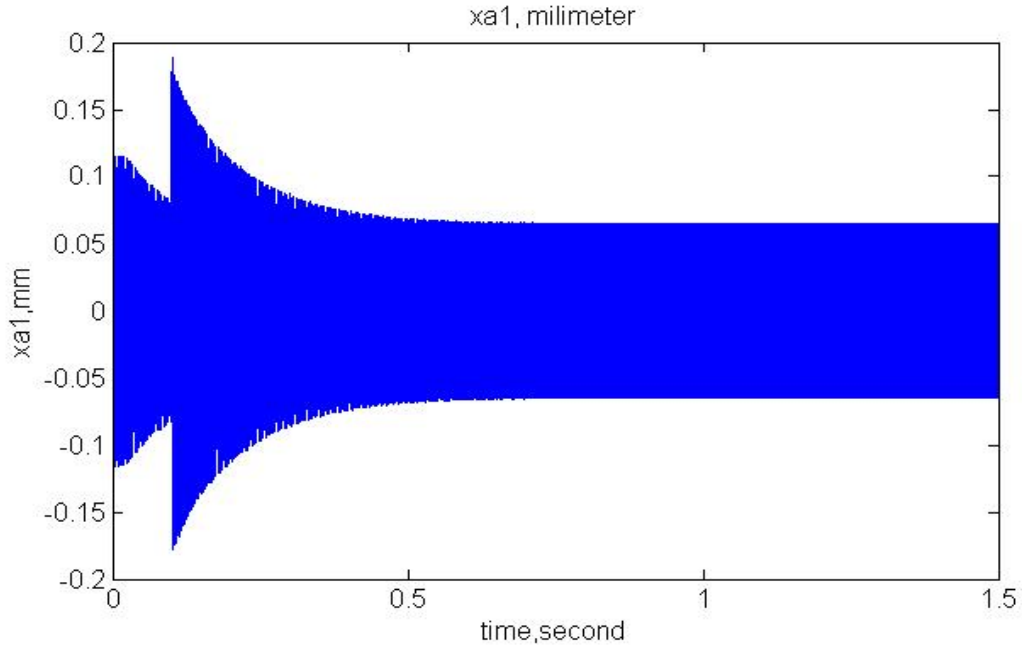

Fig. 5.48 Time response of rotor vibration at bearing A in X-direction with $\alpha = 0.414$, gyroscopic effect and impulse excitation at 187,500rpm

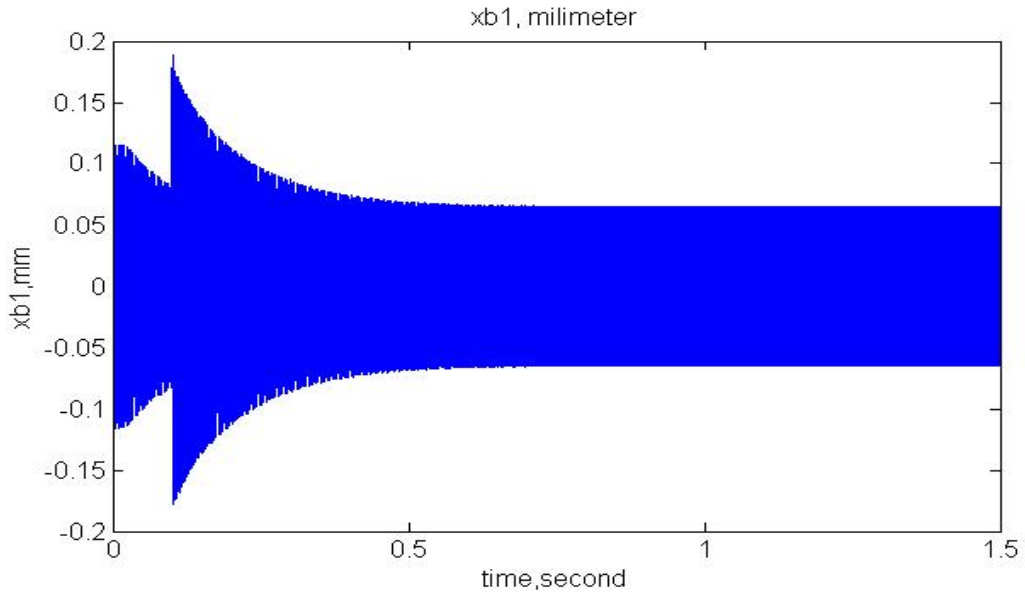

Fig. 5.49 Time response of rotor vibration at bearing B in X-direction with $\alpha = 0.414$, gyroscopic effect and impulse excitation at 187,500rpm

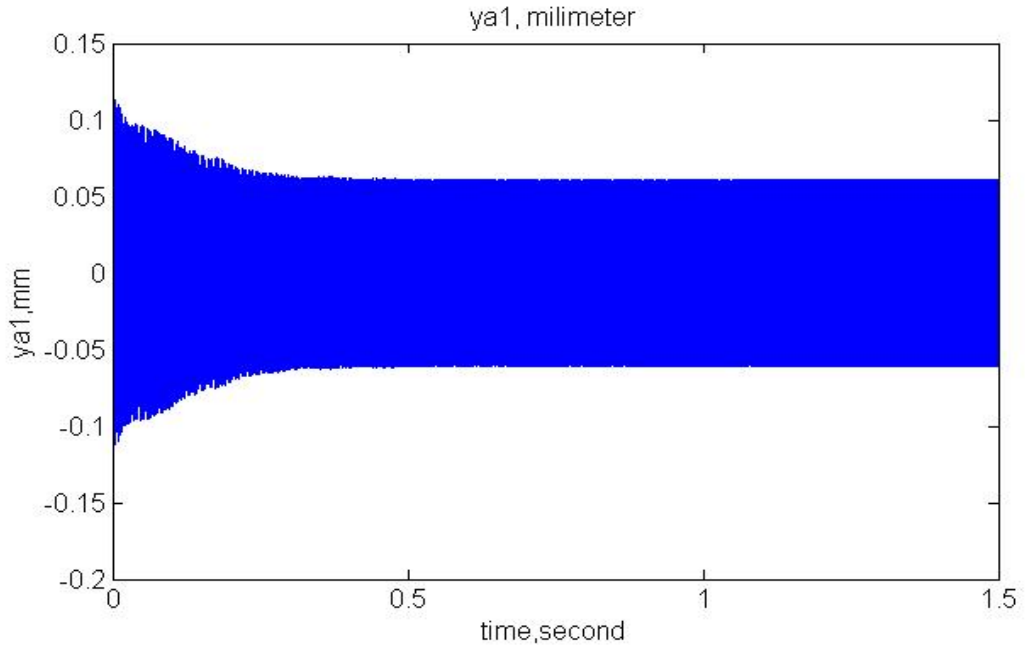

Fig. 5.50 Time response of rotor vibration at bearing A in Y-direction with $\alpha = 0.414$, gyroscopic effect and impulse excitation at 187,500rpm

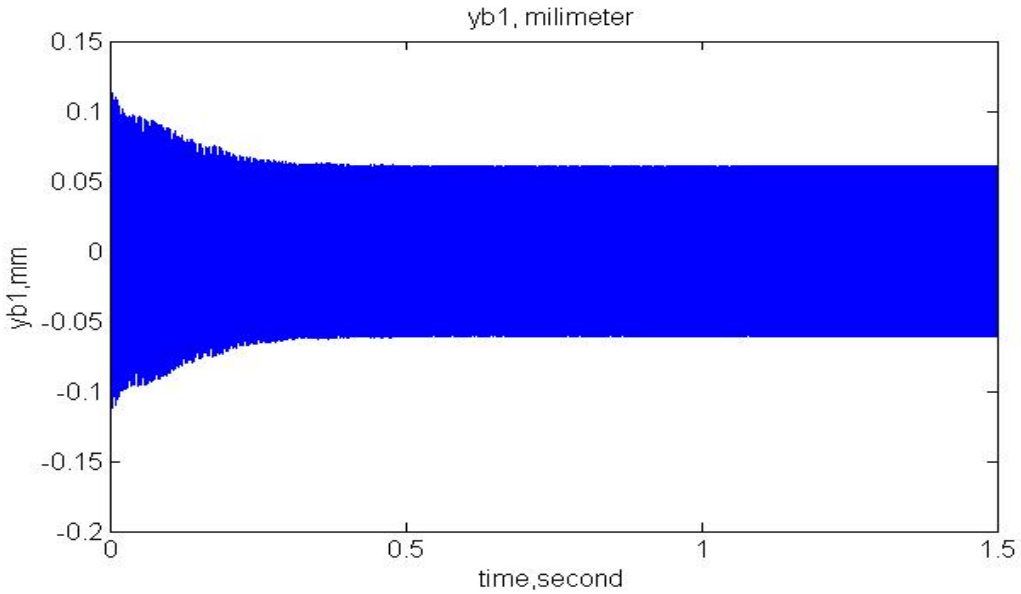

Fig. 5.51 Time response of rotor vibration at bearing B in Y-direction with $\alpha = 0.414$, gyroscopic effect and impulse excitation at 187,500rpm

As shown in Figs. 5.48 and 5.49, the impulse is imposed along the X-direction at where the sudden peaks are registered which is 0.1 seconds after start-up. It is evident from reviewing Figs. 5.48-5.51 that the time-domain X- and Y-direction vibrations of the rotor in response to the short impact are all bounded under the exertion of the nonlinear time-frequency controller.

The phase portraits of the rotor motion given in Figs. 5.52-5.55 are geometrically similar to those seen in Figs. 5.23-5.26 in being symmetrical and bounded. This is the first indication that, under the jurisdiction of the nonlinear time-frequency controller, the controlled response of the AMB-suspended rotor subject to the imposed impact is a limit-cycle. That the controlled motion state of the rotor is indeed a well-defined limit-cycle is further confirmed by Figs. 5.56-5.63. The corresponding phase portraits in Figs. 5.56-5.59 convey that the rotor motion is quasi-periodic and stable. The definitive fractal structures

seen in Figs. 5.60-5.63, on the other hand, suggest that the controlled AMB system is both deterministic and predicable - the same conclusions drawn using Figs. 5.35-5.43 with the case without considering the exertion of the impact.

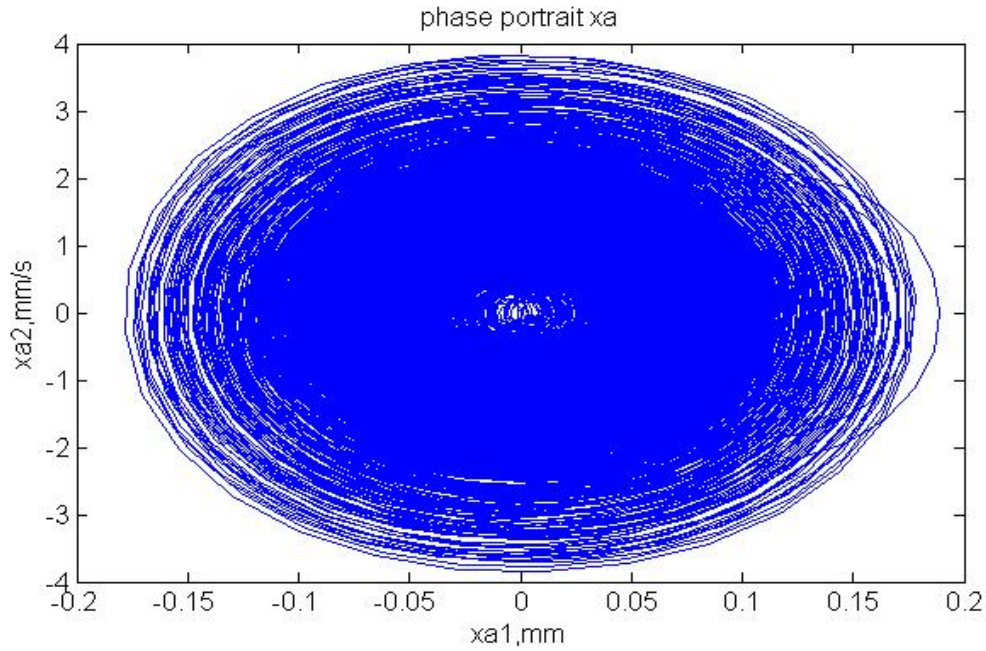

Fig. 5.52 Phase portrait of rotor motion at bearing A in X-direction with $\alpha = 0.414$, gyroscopic effect and impulse excitation at 187,500rpm

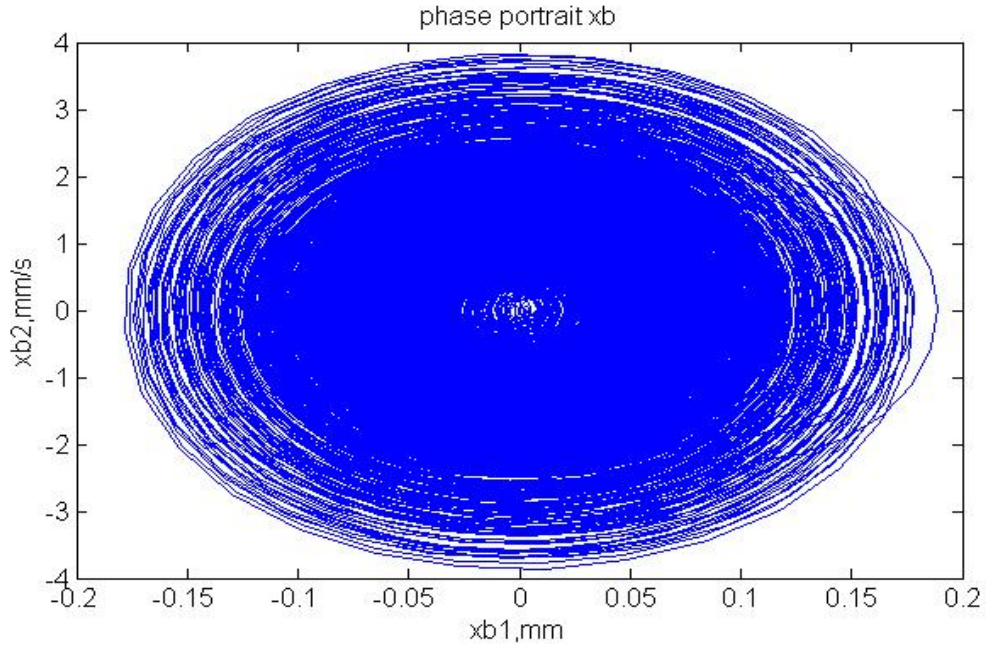

Fig. 5.53 Phase portrait of rotor motion at bearing B in X-direction with $\alpha = 0.414$, gyroscopic effect and impulse excitation at 187,500rpm

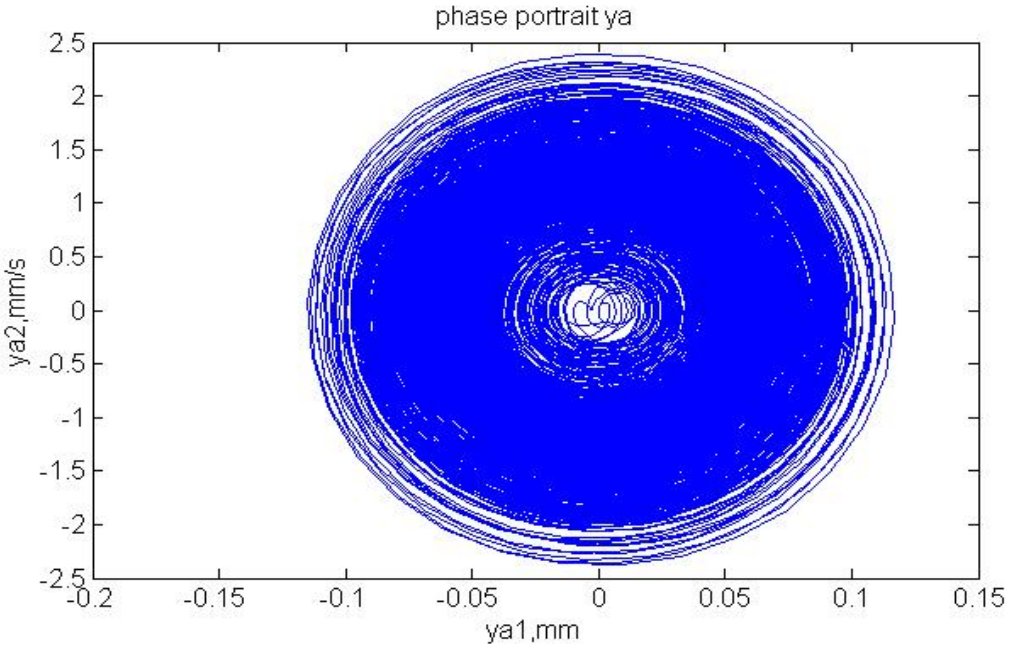

Fig. 5.54 Phase portrait of rotor motion at bearing A in Y-direction with $\alpha = 0.414$, gyroscopic effect and impulse excitation at 187,500rpm

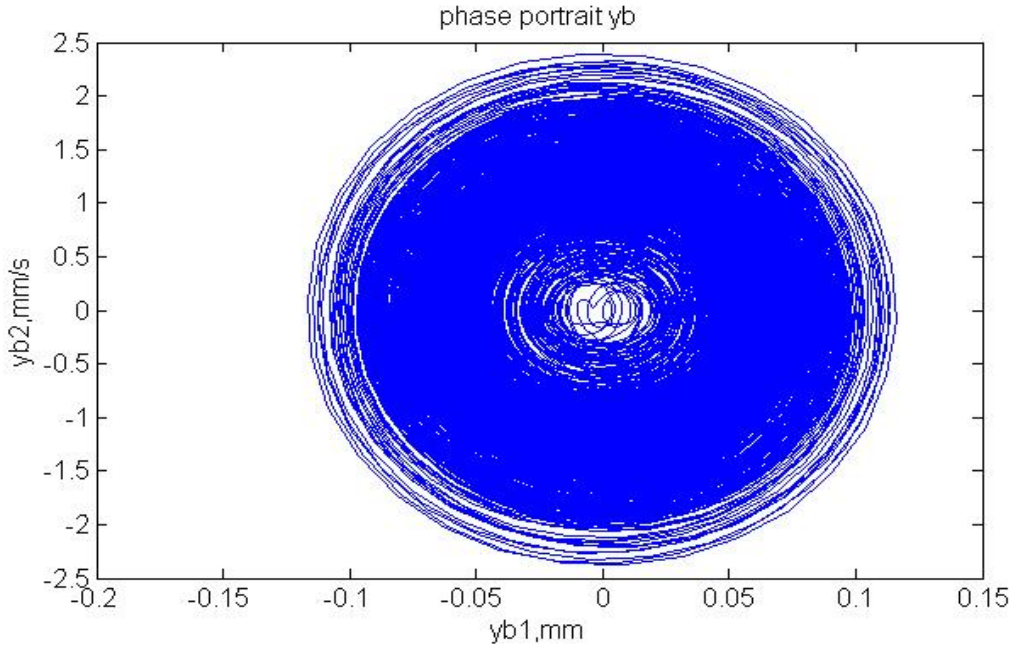

Fig. 5.55 Phase portrait of rotor motion at bearing B in Y-direction with $\alpha = 0.414$, gyroscopic effect and impulse excitation at 187,500rpm

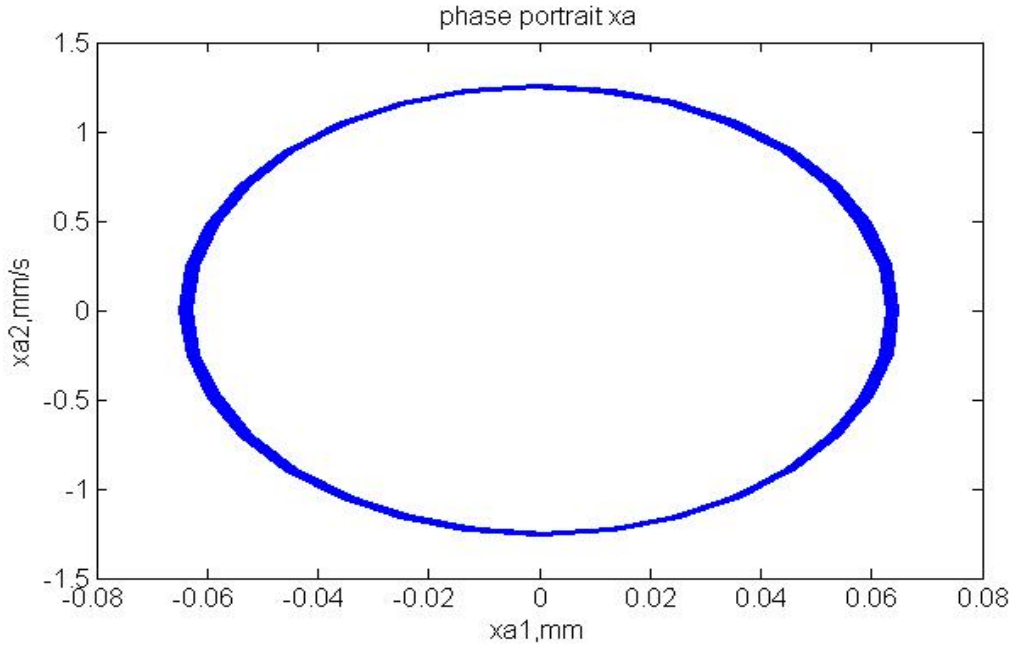

Fig. 5.56 Phase portrait of rotor motion at bearing B in X-direction with $\alpha = 0.414$, gyroscopic effect and impulse excitation at 187,500rpm (after 1 seconds)

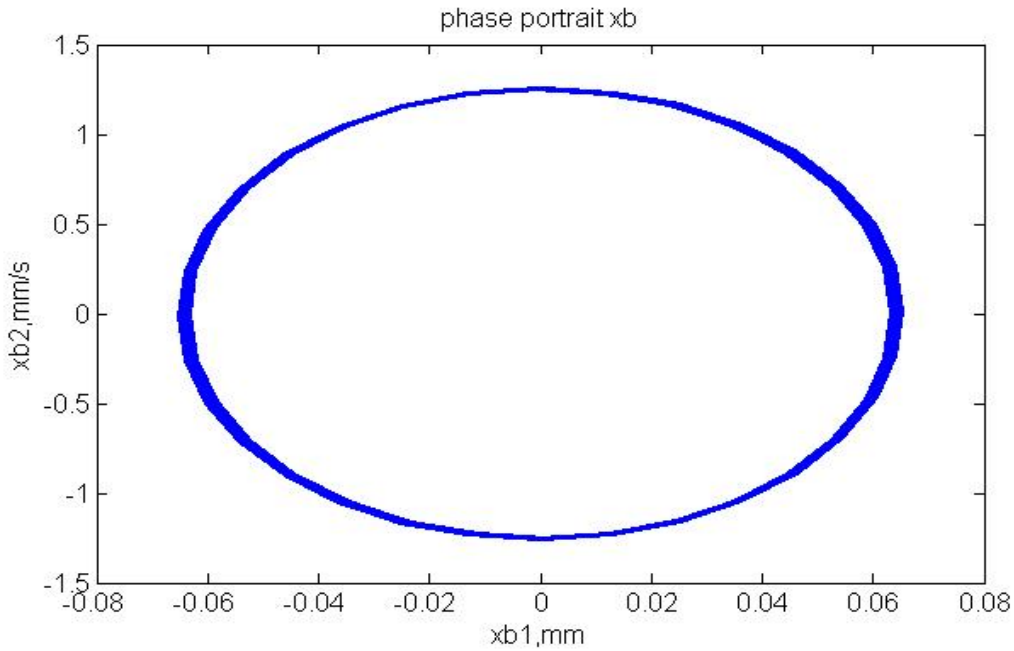

Fig. 5.57 Phase portrait of rotor motion at bearing A in Y-direction with $\alpha = 0.414$, gyroscopic effect and impulse excitation at 187,500rpm (after 1 seconds)

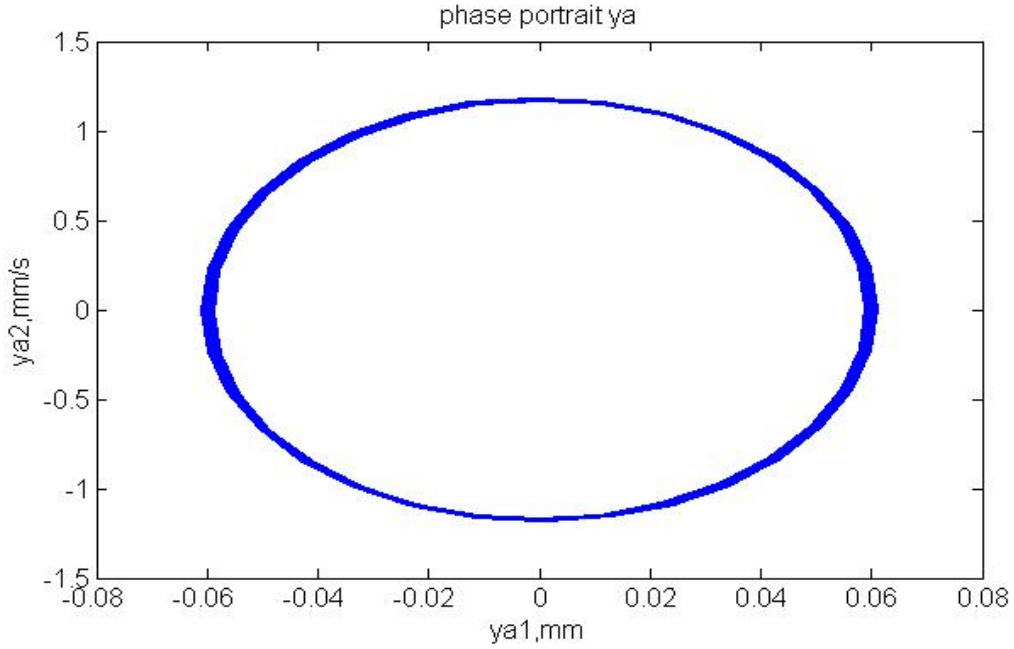

Fig. 5.58 Phase portrait of rotor motion at bearing A in Y-direction with $\alpha = 0.414$, gyroscopic effect and impulse excitation at 187,500rpm (after 1 seconds)

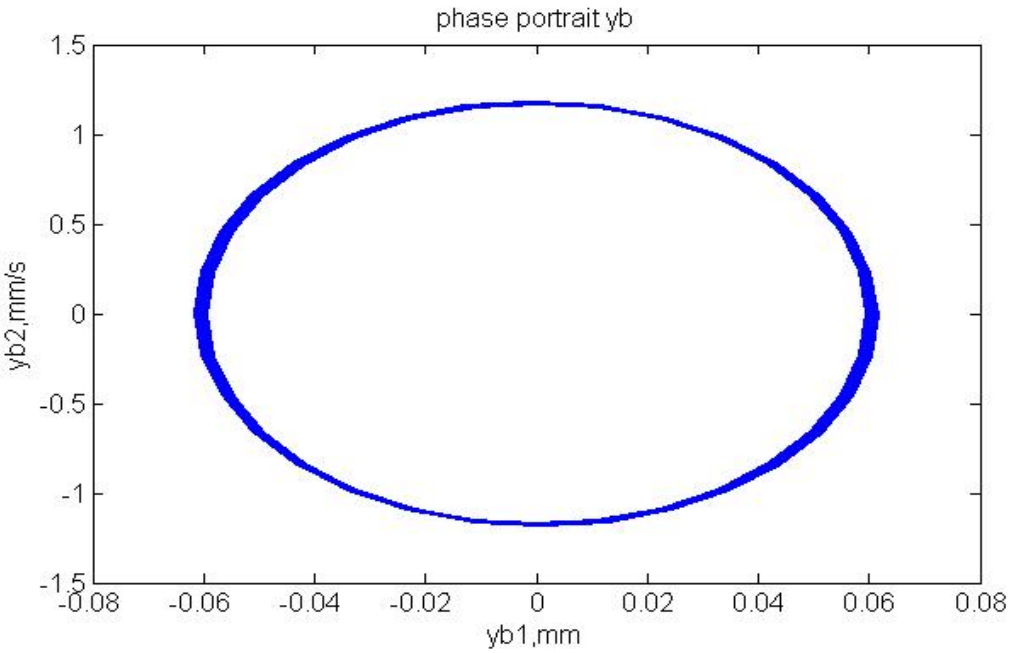

Fig. 5.59 Phase portrait of rotor motion at bearing B in Y-direction with $\alpha = 0.414$, gyroscopic effect and impulse excitation at 187,500rpm (after 1 seconds)

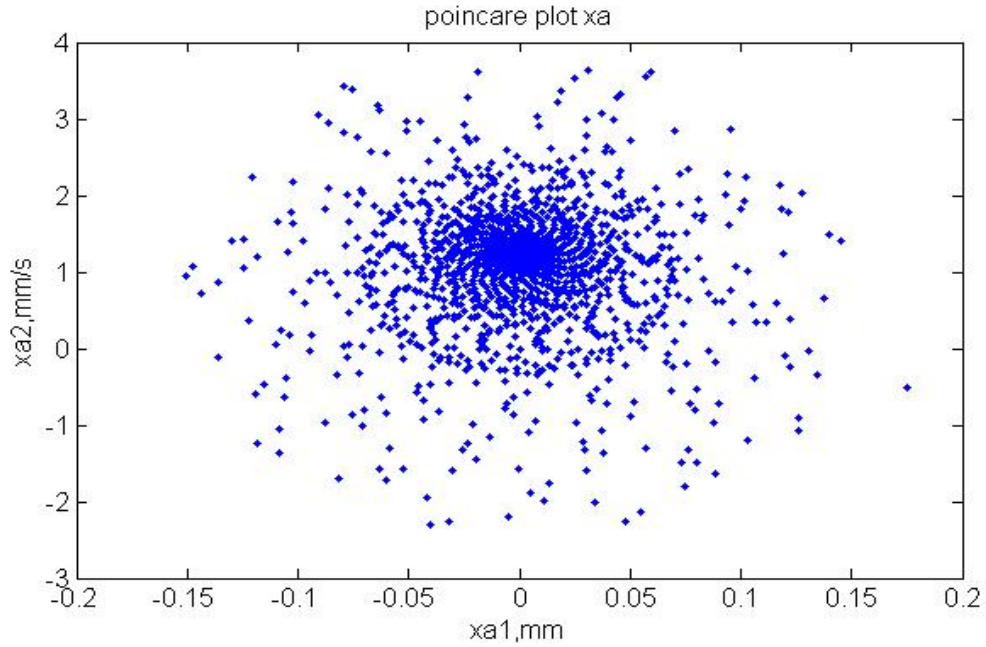

Fig. 5.60 Poincare section of rotor motion at bearing B in X-direction with $\alpha = 0.414$, gyroscopic effect and impulse excitation at 187,500rpm

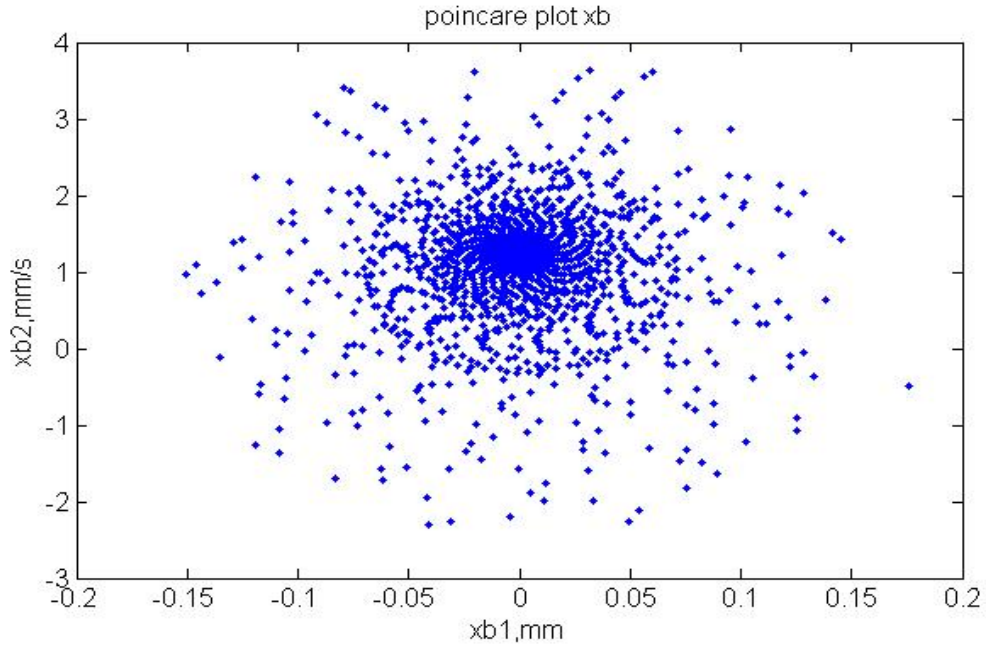

Fig. 5.61 Poincare section of rotor motion at bearing A in X-direction with $\alpha = 0.414$, gyroscopic effect and impulse excitation at 187,500rpm

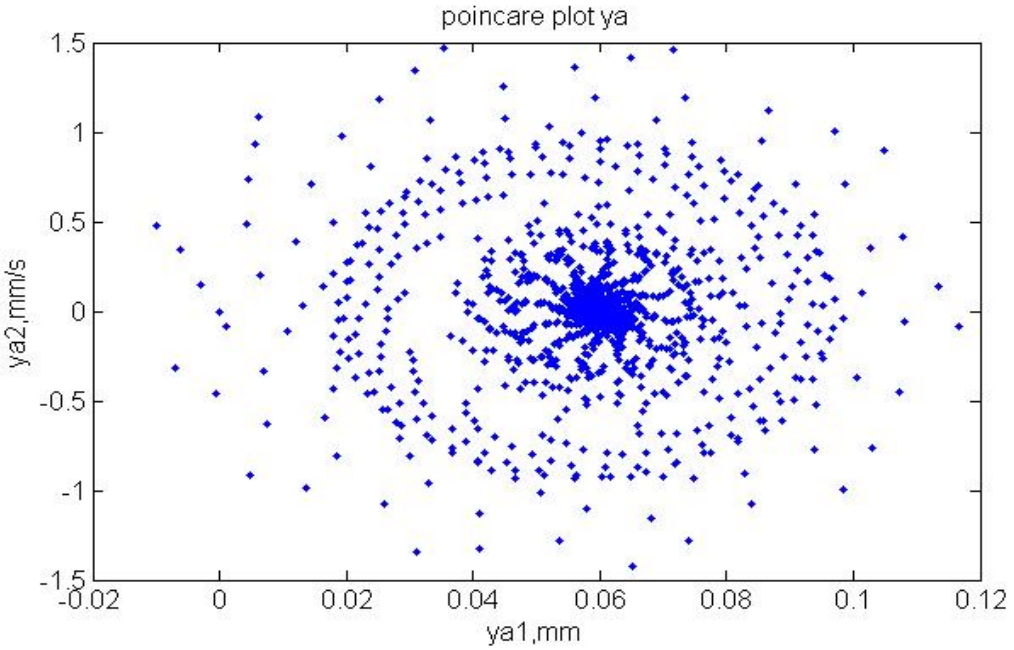

Fig. 5.62 Poincare section of rotor motion at bearing A in Y-direction with $\alpha = 0.414$, gyroscopic effect and impulse excitation at 187,500rpm

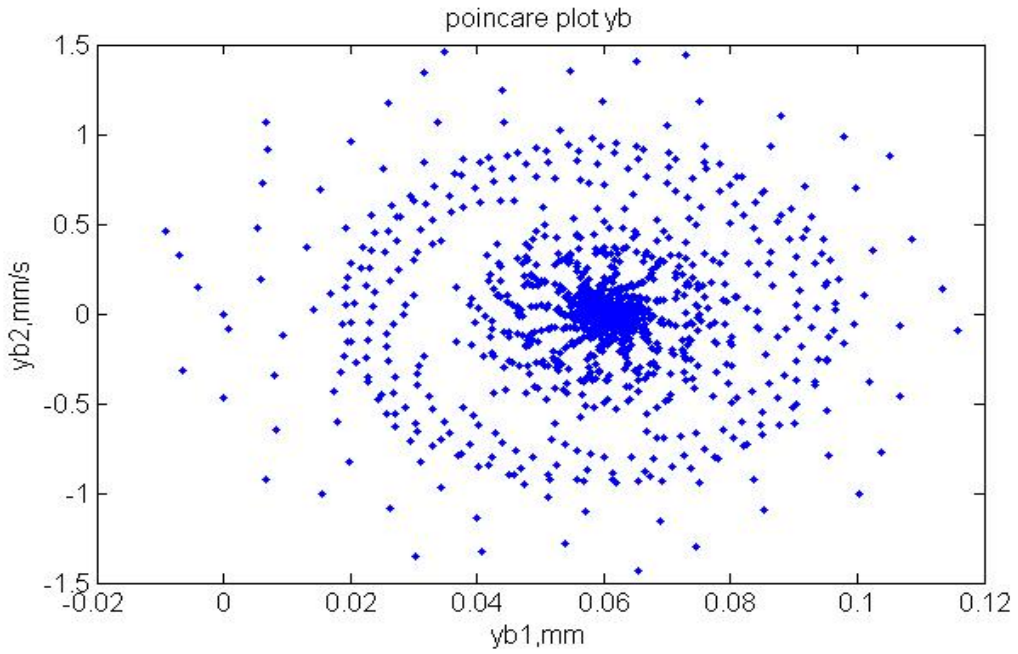

Fig. 5.63 Poincare section of rotor motion at bearing B in Y-direction with $\alpha = 0.414$, gyroscopic effect and impulse excitation at 187,500rpm

The prominent spectral feature of the imposed impact can be readily perceived in the corresponding instantaneous frequency plots in Figs. 5.64-5.67. A comparison made with the instantaneous frequencies given in Figs. 5.44-5.47, one sees that the action of the impulse results in broadband, non-stationary spectral responses whose presence significantly aggravate the dynamic stability of the system and temporarily delays the functioning of the controller. With the nonlinear time-frequency controller remaining on-line, the vibration amplitude is ultimately suppressed and the spectral responses in terms of bandwidth and the non-stationary of the high frequency components sufficiently limited and restrained.

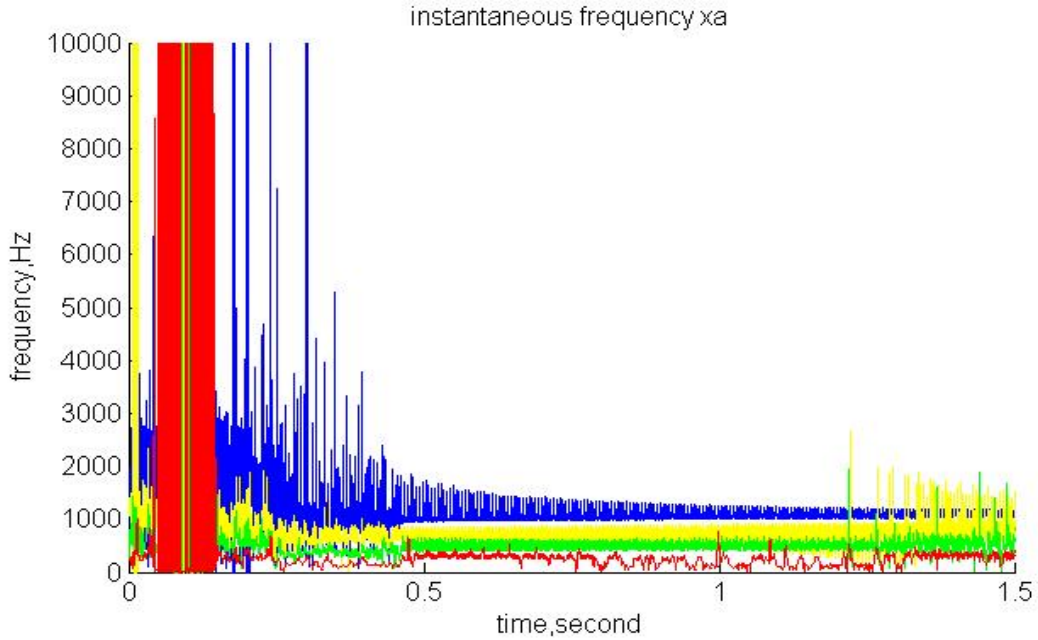

Fig. 5.64 Instantaneous frequency of rotor motion at bearing A in X-direction with $\alpha = 0.414$, gyroscopic effect, and impulse excitation at 187,500rpm

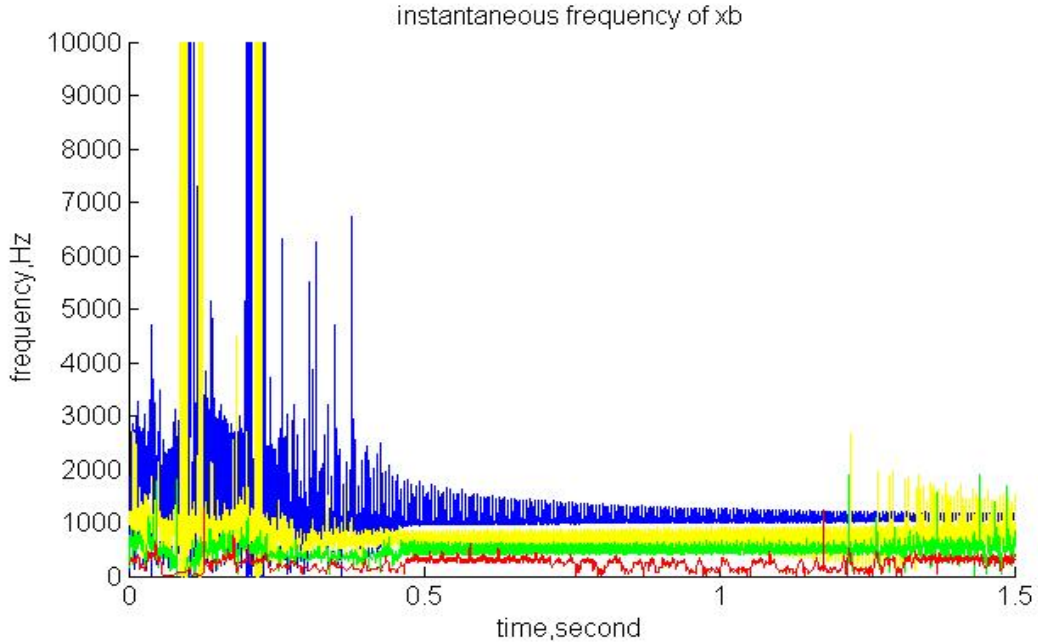

Fig. 5.65 Instantaneous frequency of rotor motion at bearing B in X-direction with $\alpha = 0.414$, gyroscopic effect, and impulse excitation at 187,500rpm

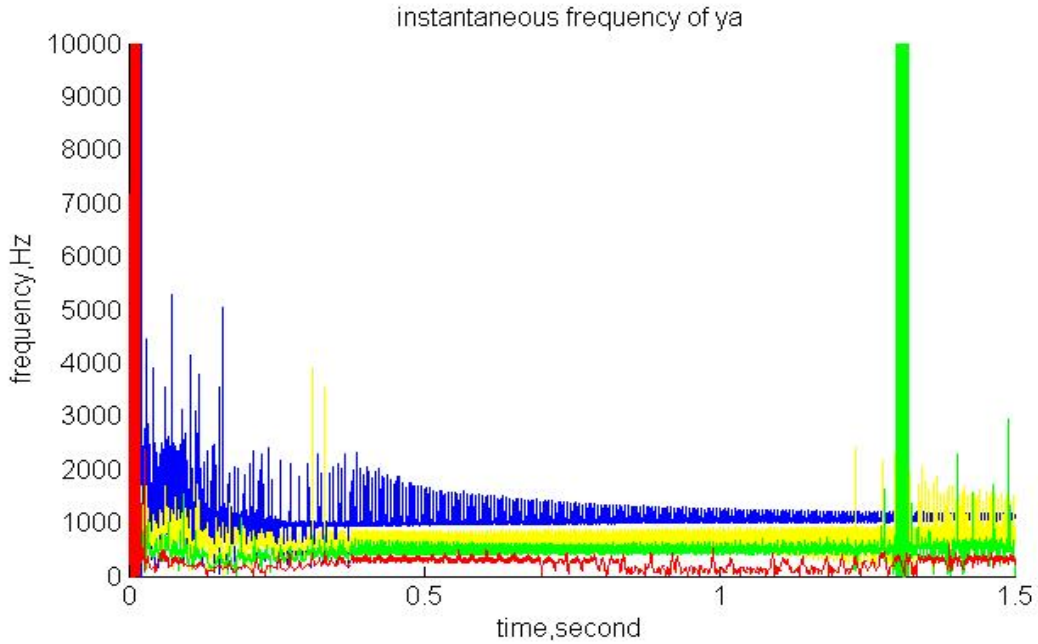

Fig. 5.66 Instantaneous frequency of rotor motion at bearing A in Y-direction with $\alpha = 0.414$, gyroscopic effect, and impulse excitation at 187,500rpm

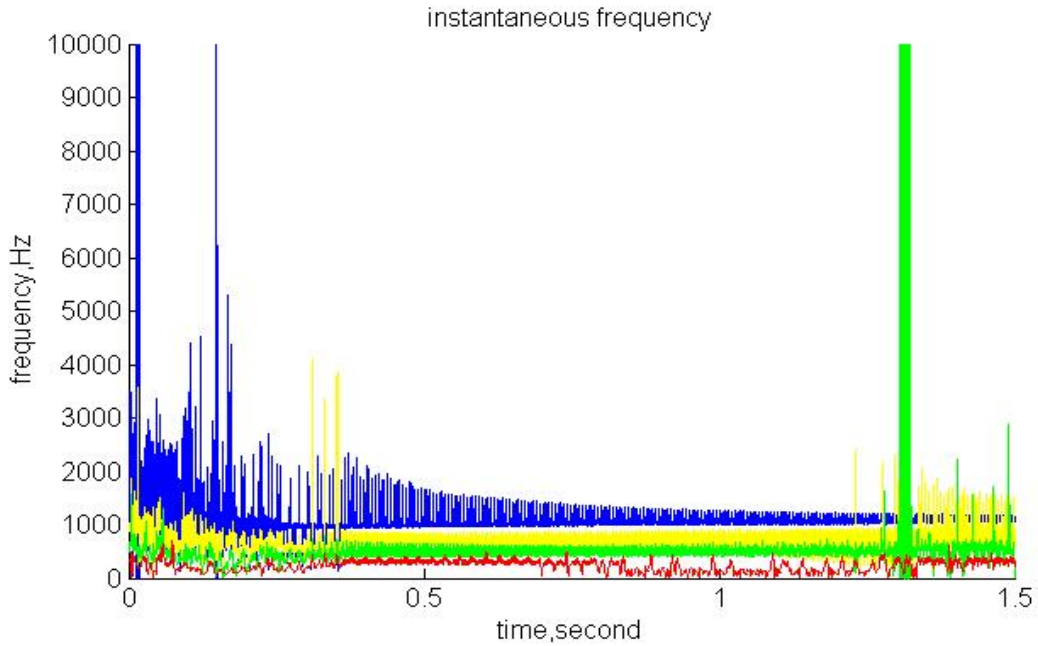

Fig. 5.67 Instantaneous frequency of rotor motion at bearing B in Y-direction with $\alpha = 0.414$, gyroscopic effect, and impulse excitation at 187,500rpm

CHAPTER VI

SUMMARY AND FUTURE WORK

6.1 Summary

The critical review performed in Chapter I indicated that the description of the underlying electro-magnetic-mechanical dynamics governing the motion of AMBs is incomplete. In Chapter II the equations of motion of a typical configuration of an AMB-supported rotor was derived in the Cartesian coordinate system. The translational and gyroscopic motions of the rotor were properly modeled without ignoring the angular moment of inertia that is made prominent by the finite length of the rotor. No linearization was employed in developing the equations of motion, so as to retain the true characteristics of the underlying rotor-dynamics. Since the electro-magnetic forces along the X and Y directions are physically coupled, a geometry coupling parameter was introduced to account for this coupling effect. The rotor considered for the study is flexible. Hence a finite eccentricity due to the weight of the rotor was also built into the equations of motion to allow for the imbalances of the rotor to be properly modeled.

In Section 3.1, the physical principle governing the generation of the electromagnetic actuation force was derived, followed by the derivation of the driving current for the AMB-rotor system in which the correlation of the electric current with the displacement of the rotor was established. The electro-mechanical system model was then presented as the state-variable representation that described the AMB-rotor model dynamics. The geometry coupling and gyroscopic effects were also considered in this state-variables representation.

In the first half of Chapter VI, the wavelet-based nonlinear time-frequency control theory was reviewed. This novel control theory employs the following two major notions to realize on-line identification and feed-forward control in the simultaneous time-frequency domain: the discrete wavelet transform (DWT) and least-mean-square adaptive (LMS) filters. The architecture of the controller design along with the control scheme was developed therein based on the state-variables representation of the AMB-rotor model system.

Numerical investigation into the effectiveness as well as performance of the nonlinear controller design was presented in Chapter V. 4 different model cases were considered in the chapter. They were: (1) model without considering gyroscopic effect, (2) model with variation of the geometry coupling parameter, (3) model with both the gyroscopic and geometry coupling effects included, and (4) model with a brief impulse excitation. In exploring the Model Case (3) the maximum speed of the model system was determined. The speed was found to be 187,500rpm subject to a tight spatial constraint (tolerance) in the order of 0.1375mm. Several conclusions were made from these model cases. The first was that it was not proper to ignore gyroscopic effect and geometry coupling, whether individually or altogether, as in so doing the system response was inadvertently misrepresented at the fundamental level. The second was that, with gyroscopic effect and geometry coupling both considered, the AMB-rotor model system was properly controlled at the maximum speed of the rotor. By employing phase portraits, Poincare sections, and instantaneous frequency, the various (controlled) responses of the system were shown to be limit-cycles that were bandwidth limited and of definitive fractal

patterns, thus signifying a stable state of motion that was quasi-periodic and deterministic. That the nonlinear controller was effective, stable, and robust was the last conclusion made which was drawn on the fact that the adverse effects induced by a broad bandwidth impulse excitation imposed on the rotor at the maximum speed was effectively negated. The controller was shown to restore the extreme state of dynamic instability back to the quasi-periodic state of stability characterized by limit-cycle.

6.2 Future Work

The research has generated an in-depth knowledge base viable for the creation of a broad set of AMB-rotor systems. Most importantly it provides the basis needed for the physical realization of a nonlinear controller configuration applicable to the robust control of AMB-rotor systems at extreme operation speed. While the endeavor documented in the thesis is both comprehensive and complete, however, more investigations into the followings are recommended. The first would be to physically validate the controller design and establish that the particular AMB-rotor configuration can indeed be controlled to demonstrate unconditional state of stability at high speeds if not precisely 187,500rpm. The second recommendation would be to consider the axial motion of the rotor in the model system. This can be done by incorporating magnetic thrust bearings (MTBs) to mitigate the translational motion of the rotor along the axial direction. Testing of the revised configuration including the controller design should then be performed to validate as appropriate.

REFERENCES

[1] Sam, Y.M. and Osman, J. H. S., "*Modeling and Control of the Active Suspension System Using Proportional Integral Sliding Mode Control Approach*," Asian Journal of Control, Vol. 7, No. 2, pp. 91-98, 2005.

[2] Lee, J. H., Allaire, P. E., Tao, G., Decker, J. A., and Zhang, X., "*Experimental Study of Sliding Mode Control for a Benchmark Magnetic Bearing System and Artificial Heart Pump Suspension*," IEEE Transactions on Control Systems Technology, Vol. 11, No. 1, pp. 128-138, 2003 .

[3] Losch, F., Gahler, C., and Herzog, R., "*Low Order u-Synthesis Controller Design for a Large Boiler Feed Pump Equipped with Active Magnetic Bearing*," Proceedings of the IEEE Conference on Control Applications, Vol. 1, pp. 564-569, 1999.

[4] Komori, M., Kumamoto, M., and Kobayashi, H., "*A Hybrid-Type Superconducting Magnetic Bearing System with Nonlinear Control*," IEEE Transactions on Applied Superconductivity, Vol. 8, No. 2, pp. 79-83, 1998.

[5] Mukhopadhyay, S. C., Ohji, T., Iwahara, M., and Yamada, S., "*Modeling Control of a New Horizontal-Shaft Hybrid-Type Magnetic Bearing*," IEEE Transactions on Industrial Electronics., Vol. 47, No. 1, pp. 100-108, 2000.

[6] Knospe, C. R., *"Active Magnetic Bearings for Machining Applications,"* Control Engineering Practices, Vol. 15, No. 3, pp. 307-313, 2007.

[7] Maslen, E. H., Bearnson, G. B., Allaire, P. E., Flack, R. D., Baloh, M., Hilton, E., Noh, M. D., Olsen, D.B., Khanwilkar, P.S. and Long J. D. "*Feedback Control*

Applications in Artificial Hearts," IEEE Control Systems, Vol. 18, No. 6, pp. 26-34, 1998.

[8] Chen, M., Knospe, C. R., "*A New Approach to the Estimation of Cutting Dynamics Using Active Magnetic Bearings*," Journal of Manufacturing Science and Engineering Transactions of ASME, Vol. 127, No. 4, pp. 773-780, 2005.

[9] Inayat-Hussain, J. I., "*Chaos via Torus Breakdown in the Vibration Response of a Rigid Rotor Supported by Active Magnetic Bearings,"* Chaos, Solitons and Fractals, Vol. 31, No. 4, pp. 912-927, 2007.

[10] Inayat-Hussain, J. I., "*Geometry Coupling Effects on Bifurcations of a Flexible Rotor Response in the Active Magnetic Bearing*," Chaos, Solitons and Fractals Vol. 41, No. 5, pp. 2664-2671, 2009.

[11] Cho, D., Kato, Y., and Spilman, D., "*Sliding Mode and Classical Controllers in Magnetic Levitation Systems*," IEEE Control System Magazine, Vol. 14, No. 2, pp. 42-48, 1994.

[12] Torries, M., Sira-Ramirez, H., and Escobar, G., "*Sliding Mode Nonlinear Control of Magnetic Bearings*," Proceedings of the IEEE International Conference on Control Applications, pp. 743-748, 1999.

[13] Charara, A., De Miras, J., and Caron, B., "*Nonlinear Control of a Magnetic Levitation System without Premagnetization,*" IEEE Transactions on Control Systems Technology, Vol. 4, No. 5, pp. 513-523, 1996.

[14] Kuseryi, I. S., *"Robust Control and Unbalance Compensation of Rotor/Active Magnetic Bearing System,"* Journal of Vibration and Control, Vol. 18, No. 6, pp. 817-832, 2012.

[15] Sabirin, C. R., Binder, A., Popa, D. D., and Craciunescu, A., *"Modeling and Digital Control of an Active Magnetic Bearing,"* Revue Roumaine des Sciences Techniques Serie Electrotechnique et Energetique, Vol. 52, No. 2, pp. 157-181, 2007.

[16] Smith, R. D. and Weldon, W. F., "*Nonlinear Control of a Rigid Rotor Magnetic Bearing System: Modeling and Simulation with Full State Feedback*," IEEE Transactions on Magnetics, Vol. 31, No. 2, pp. 973-980, 1995.

[17] Mittal, S. and Menq, C. H., "*Precision Motion Control of a Magnetic Suspension Actuator Using a Robust Nonlinear Compensation Scheme*," IEEE/ASME Transactions on Mechatronics, Vol. 2, No. 4, pp. 268-280, 1997.

[18] Liu, M.-K. and Suh, C.S.**,** "*Simultaneous Time-Frequency Control of Friction-Induced Instability*," Journal of Applied Nonlinear Dynamics, Vol. 3, No. 3, pp. 227-243, 2014.

[19] Liu, M.-K. and Suh, C.S., "*On Controlling Milling Instability and Chatter at High Speed*," Journal of Applied Nonlinear Dynamics, Vol. 1, No. 1, pp. 59-72, 2012.

[20] Virgin, L. N., Walsh, T. F. and Knight, J. D., *"Nonlinear Behavior of a Magnetic Bearing System,"* Journal of Engineering for Gas Turbines and Power Transactions of the ASME, Vol. 117, No. 3, pp. 582-588, 1995.

[21] Virgin, L. N., Walsh, T. F., Knight, J. D., "*Dynamic Analysis of a Magnetic Bearing System with Flux Control*," NASA Langley Research Center, Second International Symposium on Magnetic Suspension Technology, Part 1; pp. 353-366, 1994.

[22] Hung, J. Y., Albritton, N. G. and Xia, F., *"Nonlinear Control of a Magnetic Bearing System,"* Mechatronics, Vol. 13, No. 6, pp. 621-637, 2003.

[23] Hung, J. Y., *"Nonlinear Control of a Magnetic Levitation System,"* International Conference on Industrial Electronics, Control and Instrumentation, pp. 268-273, 1991.

[24] Suh, C. S. and Liu, M.-K., "*Control of Cutting Vibration and Machining Instability*," John Wiley, Hoboken, NJ.

[25] Pai, P. F. and Palazotto, A. N., "*Detection and Identification of Nonlinearities By Amplitude and Frequency,"* Mechanical System and Signal Processing, Vol. 22, No. 5, pp. 1107-1132, 2008.